IN-34
45347
(1+6)

p. 108

NASA Contractor Report 195038

Shock Tunnel Studies of Scramjet Phenomena 1993

Supplement 10

R. J. Stalker, R. J. Bakos, R. G. Morgan, L. Porter, D. Mee, A. Paull, S. Tuttle,
J. M. Simmons, M. Wendt, K. Skinner, Y. He, A. Neely, and W. Daniel
University of Queensland, St. Lucia, Queensland, Australia

(NASA-CR-195038) SHOCK TUNNEL
STUDIES OF SCRAMJET PHENOMENA 1993
(Queensland Univ.) 108 p

N95-25394
--THRU--
N95-25400
Unclas

G3/34 0045347

Grant NAGW-674

January 1995

National Aeronautics and
Space Administration
Langley Research Center
Hampton, Virginia 23681-0001

SHOCK TUNNEL STUDIES OF SCRAMJET PHENOMENA 1993
NASA GRANT NAGW-674 - SUPPLEMENT 10

In accord with the format of previous reports, this consists of a series of reports on specific projects. There is a brief introduction commenting on each report, and the project reports follow in the order of the headings in the introduction.

"Program A" corresponds to work funded jointly by NAGW-674 and Australian sources, and "Program B" to that funded by Australian sources alone.

PROGRAM A

(i) COMPARATIVE STUDIES OF T4 AND HYPULSE

Chemical Recombination in an Expansion Tube (R. Bakos and R.G. Morgan)

An analytical and numerical study has been carried out to determine the probable "frozen" composition of air test gas in an expansion tube. A model for diaphragm rupture was assumed and, using this model, it was found that the test gas composition could be obtained from an entropy correlation, similar to that employed by Harris for steady nozzle flows.

(ii) DIRECT MEASUREMENT OF THRUST/DRAG

(a) Drag Measurements on Blunted Cones and a Scramjet Vehicle in Hypervelocity Flow (L. Porter, D. Mee and A. Paull)

This records our first measurement of drag on a scramjet model (as well as drag measurements on blunt cones). Drag coefficients of the model were found to be quite high, and were subsequently reduced by reducing the afterbody cone angle, and the angle of the afterbody of the splitters between the combustion chambers.

(b) Thrust Measurements of a Complete Axisymmetric Scramjet in an Impulse Facility (A. Paull, R.J. Stalker and D.J. Mee)

This records the early measurements of thrust when fuel was injected on the scramjet model above. The model was modified by reducing the thrust surface angles as noted.

(c) Scramjet Thrust Measurement in a Shock Tunnel (A. Paull, R.J. Stalker and D.J. Mee)

The effect of stagnation enthalpy on scramjet thrust is measured in this paper. It is found that the positive thrust measured at 3.0 MJ/kg falls rapidly as stagnation enthalpy is increased, and above 3.5 MJ/kg, a negative thrust is recorded. Subsequent investigation showed that this was primarily due to the increase in precombustion temperature.

(d) Thrust Measurement in a 2-D Scramjet Nozzle (S. Tuttle, D.J. Mee and J.M. Simmons)

Considerable difficulty has been experienced in measuring thrust with this non-axisymmetric configuration, but the present measurements show evidence of a well deserved success. They show that skin friction losses do not make a large difference to the thrust of the nozzle.

(iii) COMBUSTION SCALING

Scaling in a Scramjet Combustor (M.V. Pulsonetti and R.J. Stalker)

This is a brief note indicating that scaling in scramjet combustors may follow that of ramjet combustors, with a scaling parameter that depends on the product (pressure x a characteristic dimension).

PROGRAM B

(i) MIXING AND COMBUSTION

(a) Hypersonic Ignition and Thrust Production in a Scramjet (A. Paull)

Measurements on a long combustion duct with a nozzle attached have been made. Specific impulse values in excess of 1500 sec were obtained with hydrogen fuel, but this decayed rapidly as stagnation enthalpy was increased.

(b) Supersonic Combustion in a Constant Area Duct (M. Wendt)

This began as a PhD study of the effect of temperature of H_2 fuel when injected into a supersonic duct. However, in understanding the results of experiments, a substantial amount of work on other effects was done. The work has been presented as a thesis, and the conclusions only are reported here.

(c) Scramjet Combustion Surveys (K. Skinner)

A PhD thesis on the mass spectrometer is currently being examined, and a chapter from that thesis relating to mass spectrometric measurements of species concentrations in a mixing and combustion wake is presented. The mass spectrometer results indicate that the width of the species concentration profiles is approximately the same as the pitot pressure profiles, indicating that species and momentum diffusion are similar.

(ii) SKIN FRICTION AND HEAT TRANSFER MEASUREMENTS

(a) Transition of Compressible High Enthalpy Boundary Layer Flow over a Flat Plate (Y. He and R.G. Morgan)

Measurements of the heat transfer to a flat plate in T4 showed transition taking place at Reynolds' number between 2.8 x 10^6 and 0.6 x 10^6 for stagnation enthalpies arranging from 3 to 7 MJ/kg.

Skin friction measurements in a turbulent boundary layer are being attempted.

(iii) EXPANSION TUBES

The Superorbital Expansion Tube Concept, Experiment and Analysis (A. Neely and R.G. Morgan)

This paper reports experiments with a small expansion tube in which a usable test flow was produced at a test section velocity of 13 km/sec.

(iv) FORCE BALANCE

Balances for the Measurement of Multiple Components of Force in Flows of a Millisecond Duration (D.J. Mee, W.J.T. Daniel, S.L. Tuttle and J.M. Simmons)

The principle of the force balance, which has been used to measure thrust and drag in shock tunnels, is extended to measure lift and pitching moment as well.

AIAA JOURNAL
Vol. 32, No. 6, June 1994

Technical Notes

TECHNICAL NOTES are short manuscripts describing new developments or important results of a preliminary nature. These Notes cannot exceed 6 manuscript pages and 3 figures; a page of text may be substituted for a figure and vice versa. After informal review by the editors, they may be published within a few months of the date of receipt. Style requirements are the same as for regular contributions (see inside back cover).

Chemical Recombination in an Expansion Tube

Robert J. Bakos* and Richard G. Morgan†
University of Queensland,
Brisbane, Queensland 4072, Australia

Introduction

HYPERSONIC propulsion and aerothermal testing requirements continue to drive the development of ground facilities capable of duplicating energy, Reynolds number, and stream chemistry at near-orbital velocities. Expansion tube pulse facilities offer this capability if the theoretical operating cycle proposed by Trimpi[1] is accepted as representing the actual flow history. As shown in the distance-time (x-t) diagram (Fig. 1a), this requires that the secondary diaphragm rupture instantaneously on impact by the primary shock, and that its mass contributes no inertia to the test gas for subsequent acceleration. However, experiments by Shinn and Miller[2] with helium test gas have shown that for even the thinnest practical diaphragm (3.18 μm polyester film in a 152-mm-diam tube) the primary shock reflection off the diaphragm maintains sufficient strength to travel more than 110 mm upstream into the oncoming test gas. Because the test gas in an expansion tube originates from the vicinity of the diaphragm, it is processed by the reflected shock. For air test gas, the entropy generated may be sufficient to cause significant oxygen dissociation that can only be eliminated by recombination in the subsequent unsteady expansion. In this sense, the problem is similar to the nozzle freezing problem occurring in high-enthalpy reflected shock tunnels.

The details of the secondary diaphragm rupture will affect both the strength of the reflected shock generated and the rate of expansion experienced by the test gas as it accelerates under the influence of the unsteady expansion. This Note adopts a diaphragm inertia rupture model[3] assuming that the diaphragm shears cleanly around its periphery, remains intact and nearly planer, and provides no resistance other than its inertia to acceleration by the pressure field. The diaphragm acceleration relieves the pressure behind the reflected shock so that it weakens with time (Fig. 1b), lowering the test gas entropy and initial dissociation levels. Also, and perhaps more importantly, the diaphragm inertia limits the initial expansion rate, allowing effective recombination to be achieved.

For this situation an approximate analytical solution for the Lagrangian pressure-time history is presented for an ideal gas. A one-dimensional numerical solution with equilibrium chemistry for the diaphragm-inertia model was also done and shows good agreement with both the approximate analytical solution and a pressure measurement for air test gas from the NASA Langley HYPULSE expansion tube.[4] The extent of recombination is then calculated using a finite rate chemistry package for the analytically or numerically determined pressure-time history.

Calculations including the diaphragm inertia show significantly lower dissociation levels than those reported recently by Wilson[5] where the diaphragm was taken to hold fast for a specified holding time and then allowed to open instantaneously without contributing inertia to the subsequent acceleration (Fig. 1c). In Ref. 5, this model was used in a full one-dimensional, unsteady-flow calculation with finite rate chemistry. An approximate calculation of recombination for this rupture model is included here for comparison with the inertia model.

Finally, a two-parameter correlation summarizes the results of the nonequilibrium calculations for air in terms of the

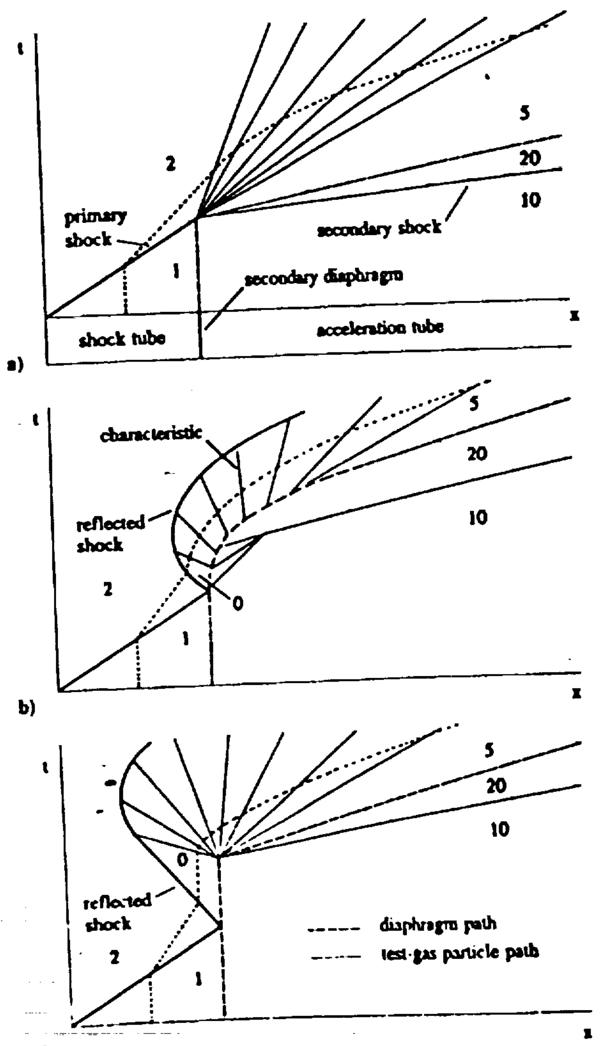

Fig. 1 x-t diagrams for secondary diaphragm rupture models: a) ideal diaphragm, b) inertial diaphragm and c) holding time diaphragm.

Received June 5, 1993; revision received Dec. 29, 1993; accepted for publication Jan. 3, 1994.

*Graduate Research Student, Department of Mechanical Engineering; currently Principal Scientist, General Applied Science Laboratories, 77 Raynor Avenue, Ronkonkoma, NY 11779. Member AIAA.

†Senior Lecturer, Department of Mechanical Engineering. Member AIAA.

postreflected shock thermodynamic properties and an inertial ime scale for the diaphragm. This allows rapid estimation of nonequilibrium air compositions for any choice of diaphragm and suborbital test conditions in an expansion tube.

Analysis

Under the assumption of a peripheral diaphragm rupture, the diaphragm motion will proceed subject to its inertia and the pressure applied to either side. Therefore, the diaphragm acts as a very light piston separating the test and acceleration gases. Because typical prerun diaphragm pressure ratios are of the order 100-1000:1, pressure in the compressing acceleration gas is negligible (for the initial portion of the diaphragm motion) relative to the test gas pressure p_d, behind the reflected shock. The equation of motion for the diaphragm is

$$\frac{du}{dt} = \frac{p_d}{\rho_d w_d} \tag{1}$$

where ρ_d is the diaphragm density and w_d the thickness.

Following Meyer,[6] the gas between the diaphragm and the reflected shock is assumed to have a uniform value of the Riemann invariant $J_+ = 2a/(\gamma - 1) + u$, where a is the sound speed and u the gas motion velocity, such that the J_- characteristics will be straight lines emanating from the diaphragm surface. That is, the expansion occurs through a simple wave. Uniformity of J_+ requires that either the reflected shock be weak such that entropy changes across it can be ignored, or that it does not decay so that again a uniform entropy region exists behind it. For conditions of interest the initial reflected shock Mach number relative to the test gas is within the range $M_{rs} = 2$-3, which, although not weak, does not significantly alter the value of J_+. J_+ is evaluated behind the fully reflected shock and assumed not to vary; thus the diaphragm motion is equivalent to that caused by an infinite-length reservoir at the postreflected shock pressure and sound speed. This leads to the following relation for the pressure on the upstream face of the diaphragm,

$$\frac{p_d}{p_0} = \left(\frac{J_+ - u_d}{J_+}\right)^{2\gamma/\gamma - 1} \tag{2}$$

where subscript 0 refers to conditions behind the fully reflected shock. Introducing a velocity scale $u_R = 2a_0/(\gamma - 1)$ and an inertial time scale $t_R = 2\rho_d w_d a_0/(\gamma + 1)p_0$ for the diaphragm motion, integration of Eq. (1) with Eq. (2) gives for the diaphragm velocity

$$\frac{u_d}{u_R} = 1 - \left(1 + \frac{t}{t_R}\right)^{-(\gamma - 1)/(\gamma + 1)} \tag{3}$$

and for the pressure history of a particle adjacent to the diaphragm face,

$$\frac{p_d}{p_0} = \left(1 + \frac{t}{t_R}\right)^{-2\gamma/(\gamma + 1)} \tag{4}$$

The initial expansion rate at $t = 0$ is $dp_d/dt = -\gamma p_0^2/\rho_d \tau_d a_0$, which is seen to be limited by the diaphragm mass.

For subsequent particles, their location and pressure-time history is evaluated analytically using the now known diaphragm trajectory (3) and the straight J_- characteristics.[7] The reflected shock trajectory is computed similarly by evaluating J_- at the diaphragm and communicating it back along the straight characteristics to specify the downstream velocity boundary condition for the shock.

For the holding time model just described, the holding time creates a fully stagnant region. The instantaneous diaphragm rupture that follows forms a centered unsteady expansion anchored to the diaphragm station (Fig. 1c). Shock decay only begins when the head of the expansion intersects the reflected shock. Taking the holding time sufficiently large so that no decay occurs for test gas particles that will comprise the useful test gas, the pressure history for a particle which enters the centered expansion at time t_0 after shock reflection is,[7]

$$\frac{p}{p_0} = \left(\frac{t}{t_0}\right)^{-2\gamma/(\gamma + 1)} \tag{5}$$

where p_0 is the pressure behind the reflected shock and $t \geq t_0$. Different particle histories correspond to different values of t_0. The initial expansion rate at $t = t_0$ is $dp/dt = -2\gamma p_0/(\gamma + 1)t_0$, so that the particle initially adjacent to the diaphragm at rupture, corresponding to $t_0 \rightarrow 0$, experiences an infinite expansion rate.

Inertial Diaphragm Model Results

The nominal Mach 17 operating condition[4] of the HYPULSE expansion tube is used for a test case. For this condition the shock tube is filled with air to 3.45 kPa, and the primary shock speed is 2670 m/s approaching the diaphragm. The acceleration tube is filled to 7.2 Pa, also with air, and the diaphragm is 12.7-μm polyester film. Equilibrium conditions behind the reflected shock at the diaphragm are $p_0 = 2.19$ MPa, $a_0 = 1380$ m/s, and $\gamma = 1.30$. The one-dimensional finite volume code of Jacobs[8] was run for this test case using approximate equilibrium chemistry. The solution was started at the time the primary shock reaches the diaphragm and continued for 0.5 ms. The diaphragm was assumed to act as a piston of fixed mass. Grid convergence was confirmed by doubling the resolution and noting no significant change in the solution.

Figure 2a shows a measured tube wall pressure trace[9] at a location 76 mm downstream of the secondary diaphragm with analytical and numerical simulations. The numerical solution accurately predicts the diaphragm location, as well as the initial pressure field. The reflected shock appears to be smeared in the experimental trace, possibly as a result of nonplaner diaphragm rupture. The analytical solution captures the general features of the flowfield, in particular the location and pressure on the diaphragm. In addition, Fig. 2b

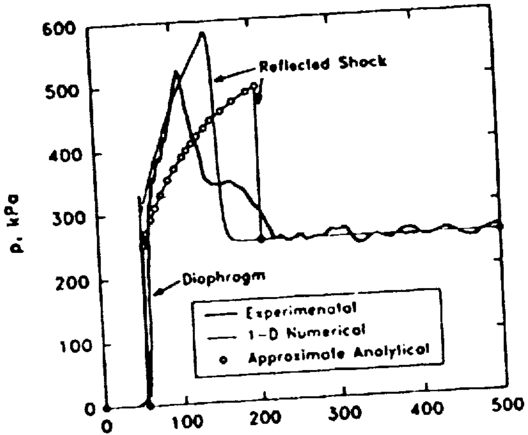

Fig. 2a Pressure history at 76 mm downstream of secondary diaphragm.

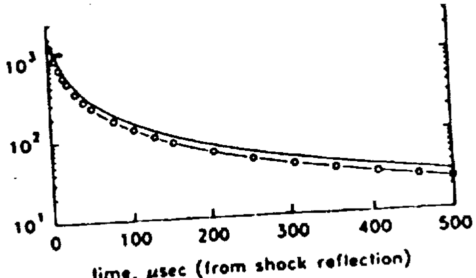

Fig. 2b Calculated pressure on diaphragm upstream surface.

shows that there is good agreement between the numerical and analytical estimates of pressure decay for the particle adjacent to the diaphragm. This also indicates that the effects of chemistry on the pressure distribution are small for the conditions considered and that the ideal gas approximation is adequate for this study.

Recombination Chemistry

Recombination in the expansion is calculated using a general chemical kinetics computer program[10] for a specified particle pressure-time history, with the gas immediately behind the reflected shock assumed to be in chemical equilibrium. There exist several choices for the chemical kinetic rate mechanisms for high-temperature air[11] that give variations of approximately ±20% in the computed atomic oxygen mass fraction. The mechanism in Ref. 12 has been widely used for computing shock tunnel nozzle flows and is adopted here.

Figure 3 shows computed atomic oxygen and nitric oxide mass fractions (the only significant air contaminants at these conditions) as a function of time after flow arrival in the test section located 14 m from the diaphragm at the exit of the acceleration tube. The time ordinate in all cases results from conserving mass between a given particle and the diaphragm when going from the postincident shock state, 2, through the reflected shock and expansion, to the facility exit, state 5 (Fig. 1).

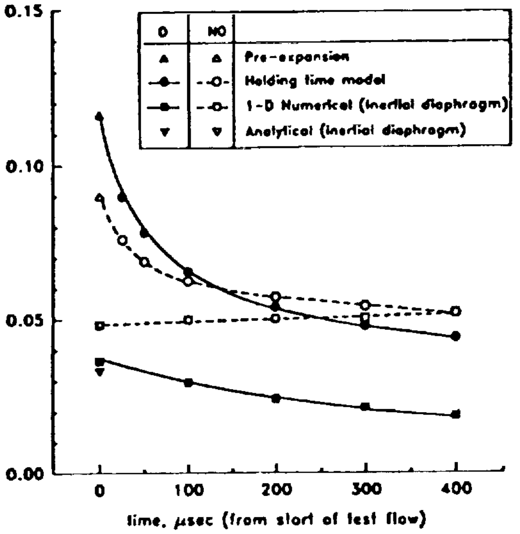

Fig. 3 Atomic oxygen (O) and nitric oxide (NO) mass fractions in the test flow at Mach 17 HYPULSE condition.

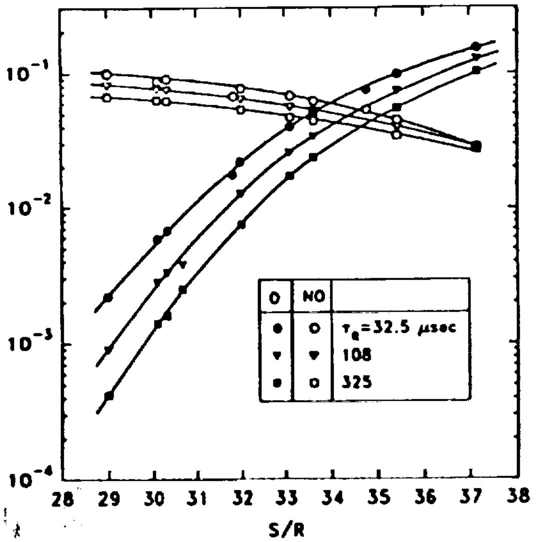

Fig. 4 Entropy-inertia correlation for predicting nonequilibrium air compositions in an expansion tube, $\tau_R = t_R p_0^{(\gamma+1)/2\gamma}$.

Considering the holding time model results, the first particles to exit the facility (those initially adjacent to the diaphragm) experience rapid expansion rates and freeze at a composition near the pre-expansion value. Subsequent particles see lesser expansion rates and recombine further, in agreement with the results of Ref. 5. For the numerical solution of the inertia model, five particle trajectories were analyzed. The presence of the diaphragm mass reduces the expansion rate for the first particles yielding greater recombination than the holding time model. Subsequent particles are processed by a weaker reflected shock altering the composition as shown. Using the pressure history from the analytical solution for the particle adjacent to the diaphragm, good agreement is found with the numerical solution there. Accuracy of the analytical solution diminishes for subsequent particles and they are not analyzed for recombination.

Entropy Correlation

For steady expansion nozzles the frozen enthalpy and composition of nonequilibrium air at the nozzle exit correlate well with the nozzle reservoir entropy.[13,14] Nonequilibrium compositions resulting from unsteady expansion can be similarly correlated using the postreflected shock entropy, provided that the initial portion of the expansion occurs in equilibrium and at constant entropy. For this situation the expansion will pass through the lower pressure starting conditions of other expansions having the same entropy. If these expansions subsequently have coincident pressure-time histories, they will yield the same final composition. From Eq. (4) it can be seen that coincident expansions have equal values of the modified time scale

$$\tau_R = t_R p_0^{(\gamma+1)/2\gamma} \tag{6}$$

All expansions with the same τ_R and initial entropy will yield the same chemical composition.

Figure 4 illustrates this correlation for atomic oxygen and nitric oxide mass fractions. It was constructed for a range of initial pressures of 1.5, 15.0, and 150 MPa and temperatures from 3500 to 6000 K. These ranges should span the majority of expansion tube operating conditions for simulating suborbital velocities. The correlation is accurate to within the uncertainty due to the high-temperature air kinetics already noted. It applies to the particle initially adjacent to the diaphragm, and thus from Fig. 3, represents an upper bound on atomic oxygen and a reasonable estimate of nitric oxide content. Departure from the correlation occurs below 3500 K where the equilibrium starting conditions fall below the freezing condition of expansions from higher pressure and the same entropy. The thermodynamic data available in the kinetics code[10] set the 6000 K maximum temperature limit.

Acknowledgments

This work was supported under a grant from the NASA Langley Research Center, NAGW-674, and by an Australian Overseas Postgraduate Research Scholarship in Australia. The authors also acknowledge R. J. Stalker for instigating the study and P. A. Jacobs for contributing the numerical simulation, both from the University of Queensland, and J. Tamagno from General Applied Science Laboratories for the experimental data.

References

[1] Trimpi, R. L., "A Preliminary Theoretical Study of the Expansion Tube, a New Device for Producing High-Enthalpy Short-Duration Hypersonic Gas Flows," NASA TR-133, 1962.

[2] Shinn, J. L., and Miller, C. G., "Experimental Perfect Gas Study of Expansion-Tube Flow Characteristics," NASA TP 1317, 1978.

[3] Morgan, R. G., and Stalker, R. J., "Double Diaphragm Driven

Free Piston Expansion Tube," *Proceedings 18th International Symposium on Shock Tubes and Waves* (Sendai, Japan, July 1991), Springer-Verlag, 1992.

[4] Tamagno, J., Bakos, R., Pulsonetti, M., and Erdos, J., "Hypervelocity Real Gas Capabilities of GASL's Expansion Tube (HYPULSE) Facility," AIAA Paper 90-1390, June 1990.

[5] Wilson, G. J., "Time-Dependent Quasi-One Dimensional Simulations of High Enthalpy Pulse Facilities," AIAA Paper 92-5096, Dec. 1992.

[6] Meyer, R. F., "The Impact of a Shock Wave on a Movable Wall," *Journal of Fluid Mechanics*, Vol. 3, No. 3, 1957, pp. 309-323.

[7] Courant R., and Friedrichs, K. O., *Supersonic Flow and Shock Waves*, Applied Mathematical Sciences, Vol. 21, Springer-Verlag, New York, 1976, pp. 97-106.

[8] Jacobs, P. A., "Quasi-One-Dimensional Modeling of Free-Piston Shock Tunnels," AIAA Paper 93-0352, Jan. 1993.

[9] Tamagno, J., private communication, General Applied Science Laboratories, Ronkonkoma, NY, July 1992.

[10] Bittker, D. A., and Scullin, V. J., "General Chemical Kinetics Computer Program for Static and Flow Reactions, with Application to Combustion and Shock Tube Kinetics," NASA TN-D-6586, Jan. 1972.

[11] Sagnier, P., and Marraffa, L., "Parametric Study of Thermal and Chemical Nonequilibrium Nozzle Flow," *AIAA Journal*, Vol. 29, No. 3, 1991, pp. 334-343.

[12] Hall, J. G., Eshenroeder, A. Q., and Marrone, P. V., "Blunt-Nose Inviscid Airflows with Coupled Nonequilibrium Processes," *Journal of the Aerospace Sciences*, Vol. 29, No. 9, 1962, pp. 1038-1051.

[13] Lordi, J. A., and Mates, R. E., "Nonequilibrium Effects on High-Enthalpy Expansions of Air," *AIAA Journal*, Vol. 3, No. 10, 1965, pp. 1972-1974.

[14] Harris, C., "Comment on 'Nonequilibrium Effects on High-Enthalpy Expansions of Air'," *AIAA Journal*, Vol. 4, No. 6, 1966, p. 1148.

DRAG MEASUREMENTS ON BLUNTED CONES AND A SCRAMJET VEHICLE IN HYPERVELOCITY FLOW

L. M. Porter[*], D. J. Mee[†] and A. Paull[#]
The University of Queensland, St. Lucia, Queensland 4072, Australia

Abstract

This paper reports some applications of the deconvolution force balance (Sanderson and Simmons, 1991) for measuring drag in hypervelocity impulse facilities where test times are of the order of 1 ms. Two basic model geometries are considered. The first is a 5° semi-vertex angle cone with varying degrees of nose bluntness. The influence of bluntness on drag on this slender conical body in a Mach 5.2 air stream at a stagnation enthalpy of 14 MJ/kg is presented. The second application is to the drag measurement on the more complex geometry of a scramjet powered vehicle. The drag on the vehicle has been measured at stagnation enthalpies in the range of 3 - 14 MJ/kg.

1 Introduction

A scramjet operating at Mach numbers above 4 is being proposed as the propulsion system for a disposable vehicle to launch small payloads into low earth orbit (Stalker, 1992). The forebody of the scramjet will be conical in geometry. Ideally, a sharp nose would reduce the aerodynamic drag on the vehicle. However, a pointed slender nose is difficult to cool and may restrict the payload capacity. These practical limitations have motivated research into the aerodynamic characteristics of a blunted cone in hypersonic (Mach number greater than 5) and hypervelocity (flight speed greater than 5 kms^{-1}) flow.

To simulate these flight conditions experiments were performed in the T4 free piston driver shock tunnel facility (Stalker and Morgan, 1988). The test times experienced in the T4 facility are of the order of 1 ms. While the drag force is a fundamental parameter in the design of any flight vehicle, its measurement in hypersonic impulse facilities is inhibited by the short test time. Conventional force balance or accelerometer balance techniques would restrict the maximum model size to 50 mm in a facility having a test time of 1 ms (Sanderson and Simmons, 1991). However, a technique for drag measurement in hypersonic impulse facilities, the deconvolution force balance, has been developed by Sanderson and Simmons (1991). This technique takes into account the distributed mass effects and depends on the interpretation of the transient stress waves propagating within the model and its supporting structure.

The present experimental programme is the first in which the technique has been used to obtain data on the drag of aerodynamic bodies of current interest. One primary aim was to obtain a preliminary measurement of the influence of nose bluntness on drag on a slender cone in hypervelocity flow. Another was to extend the technique to measuring the drag on the more complex geometry of a scramjet vehicle. Having achieved these objectives it is envisaged that a more comprehensive investigation into nose bluntness effects can be conducted. The result of applying this knowledge to the optimal design of a scramjet vehicle can then be measured directly using the deconvolution force balance to measure the drag in hypersonic and hypervelocity test flows.

2 Experiments

2.1 Facility

The experiments were performed in the T4 free piston driver shock tunnel facility (Stalker and Morgan, 1988). A contoured axisymmetric Mach 5 nozzle was used to expand the gas from the stagnation region to the appropriate test conditions. The nozzle exit plane was 265 mm in diameter and the nozzle throat diameter was 25 mm. The tunnel was operated in a tailored mode so that the static pressure and enthalpy would be constant throughout the flow test time.

2.2 Drag Measurement Technique

The model is attached to a "sting" in the form of a slender elastic bar (Figure 1). The sting is suspended

---

[*] Graduate Student, Department of Mechanical Engineering.

[†] QEII Research Fellow, Department of Mechanical Engineering.

[#] Research Fellow, Department of Mechanical Engineering.

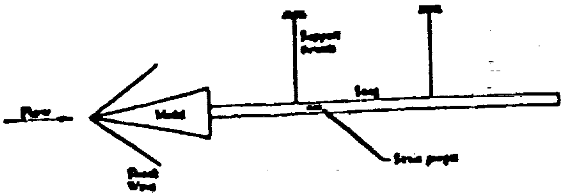

Figure 1. Drag balance configuration.

by vertical threads to allow free movement in the axial direction. Strain gauges located on the sting record the passage of stress waves resulting from the impulsively applied drag force as they are transmitted from the model into the sting.

Following Sanderson and Simmons (1991) the dynamic behaviour of the model/sting combination is modelled as a time-invariant, causal, linear system described by the convolution integral,

$$y(t) = \int_0^t g(t - \tau)\, u(\tau)\, d\tau \qquad (1)$$

where u(t) is the single input to the system, y(t) is the resulting output and g(t) is the unit impulse response function. Knowing the response of the system to a unit impulsive force it is possible to determine the response of the system to excitation by any arbitrary force via Equation 1. Alternatively, and what is done here, y(t) is obtained from the strain gauge output and a numerical deconvolution process is performed to obtain u(t), the time-history of drag applied to the model (Sanderson and Simmons, 1991)..

It has been demonstrated that the technique is insensitive to small changes in the impulse response function (Simmons et al (1992)). Thus the unit impulse response function may be approximated numerically using dynamic finite element modelling.

2.3 Variable Nose Bluntness Slender Cone Model

Experiments were performed on a 5° semi-vertex angle aluminium cone of 100 mm base diameter. A total of 11 variable nose tips was used ranging in nose radius from 0.2 mm to 18.0 mm in steps of 1.8 mm. These correspond to bluntness ratios of 0.004 to 0.36 where the bluntness ratio is the ratio of the nose radius to the cone base radius. The cone is 571.5 mm long with the sharpest tip attached. The base of the cone was made hollow in order to reduce the mechanical time constant of the system (Porter et al, 1992). This reduced the mass of the model by almost 50 %.

The 2.5 m long sting was constructed from brass tubing of 34.9 mm outside diameter and 1.6 mm wall thickness, giving a high bending stiffness. The sting length was chosen to delay the interference of the stress wave reflected from the free end of the sting with the flow test time. As the speed of propagation of stress waves in brass is 3.6 kms^{-1}, a sting length of 2.5 m allowed 1.3 ms before the reflected waves arrived at the strain gauges. (This estimate of test time takes into account the positioning of the strain gauges 300 mm from the model/sting interface (Figure 1))

Figure 2 shows a diagram of the model/sting arrangement with the finite element mesh used to calculate the unit impulse response function superimposed. As the drag measurement technique used here is insensitive to small changes in the impulse response (Simmons et al, 1992) and as the unit impulse response function is in turn relatively insensitive to the loading distribution on the model, the impulse response determined for a distributed load on the sharp cone model has been used in the numerical deconvolution to obtain the drag for all the blunted cone models tested.

2.4 Scramjet Vehicle Model

The model of the scramjet vehicle was made of aluminium and consisted of a centrebody surrounded by 6 evenly distributed combustion chambers (Figure 3). The centrebody was composed of a 9° semi-vertex angle sharp conical forebody of length 99 mm; a 9° intake surface extending for a further 60 mm; a combustion duct length of 60 mm; and a 15° thrust surface of length 55 mm. The scramjet centrebody thus had a total length of 274 mm. The combustion duct was also made of aluminium and had a total length of 145 mm. The stainless steel cowl surface angle at the thrust nozzle exit was 7°.

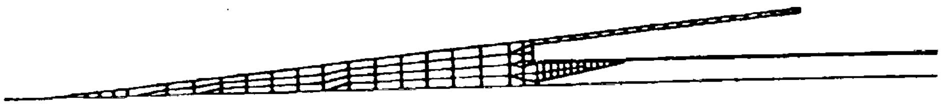

Figure 2. Finite element model of sharp cone model and sting.

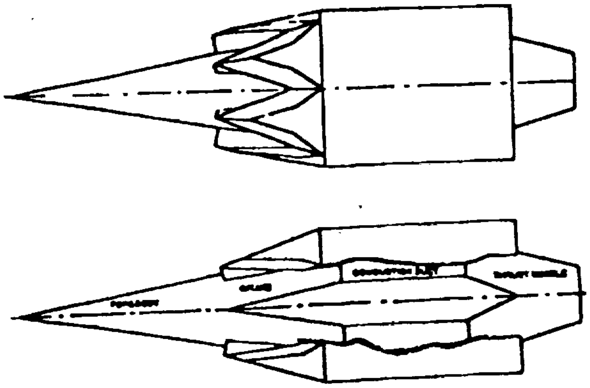

Figure 3. Scramjet powered vehicle.

The scramjet model had 6 combustion ducts evenly distributed about the centrebody. The diameter of the centrebody for the length of the combustion chambers was 51 mm. The internal diameter of the combustion duct cowl was 69 mm and the external diameter was 71 mm. Each of the combustion chambers was approximately 12 mm in radial width. No provision was made for injecting fuel into the scramjet ducts on this model.

For these tests the scramjet model was attached to the nose of the cone in place of one of the blunt tips. The cone was then shielded from the flow to prevent it from experiencing any aerodynamic forces.

The unit impulse response function was determined numerically using a dynamic finite element program for the case of a point load applied axially at the tip of the model. The finite element mesh for the scramjet model is shown in Figure 4. The supports attaching the centrebody to the cowl were designed to approximate the mass of the walls of the 6 combustion chambers. This was done so that the scramjet could be modelled with an axisymmetric finite element mesh to simplify the numerical analysis.

2.5 Instrumentation

Kulite UHP-5000-060 semi-conductor strain gauges were used to measure the system output y(t). These gauges have a gauge factor of 155 but they are highly temperature sensitive. This made it necessary to use a modified Wheatstone bridge circuit to compensate the gauge output signals against undesirable temperature effects. Four strain gauges were used. Two gauges were attached to a separate piece of the sting material and placed near the sting so that they saw the same thermal environment but no mechanical strain. The two strain measuring gauges were arranged so that the circuit was sensitive only to axial loads.

Measurements of the pressure in the base area of the cone were obtained. Additional instrumentation consisted of measurement of the shock speeds in the shock tube and stagnation pressures. These are used to determine the conditions of the test gas.

3 Results and Discussion

3.1 Test Flow Conditions

The conditions in the test section were numerically determined using ESTC (McIntosh, 1968) and NENZF (Lordi et al, 1966). The shock speed in the shock tube and the stagnation pressure were measured and used as inputs to ESTC to determine the temperature of the test gas in the stagnation region after shock reflection. The test gas undergoes a steady expansion from the stagnation region to the test flow properties at the exit plane of the nozzle. NENZF is a one-dimensional non-equilibrium code which is then used to predict the properties of the test gas at the nozzle exit plane given the stagnation pressure and temperature.

Measurements made of the test section Pitot pressure and static pressure were found to agree well with those predicted by NENZF. The test flow properties were found to be repeatable to within 10%. The four conditions at which tests have been performed are listed in Table 1. All experiments were conducted in a test gas of air.

3.2 Blunted Cone Drag Measurements

Experiments on the variable nose bluntness slender cone model were performed at the 14.4 MJ/kg test condition (Table 1). The signal output from the strain gauge bridge was deconvoluted numerically as described in Section 2.2 to obtain the time history of

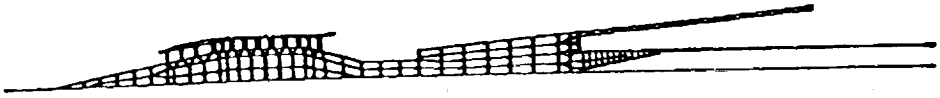

Figure 4. Finite element model of scramjet vehicle and sting.

Condition	Stagnation Enthalpy MJ/kg	Mach No.	Static Pressure kPa	Pitot Pressure kPa	Static Temperature K	Flow Velocity km/s	Density kg/m3
A	14.4	5.2	16	555	1860	4.5	0.028
B	10.8	5.4	18	580	1500	4.1	0.035
C	3.3	6.4	10	570	355	2.6	0.094
D	2.9	6.8	3.8	200	310	2.3	0.038

Table 1. Flow conditions in a test gas of air.

the drag on the model. This drag measurement technique is inherently noisy as the deconvolution process tends to amplify any noise present in the original output signal, y(t). It was thus necessary to pass all the drag measurements resulting from the numerical deconvolution process through a 2 kHz, 6 pole Butterworth low-pass digital filter.

Figure 5 shows the measured drag in its filtered form for a nose radius of 10.8 mm in comparison with its corresponding strain gauge output signal before deconvolution. The steady flow test time may be identified by the regions of steady drag, occuring around 4.8 ms in Figure 5.

The results from this preliminary study into the effects nose bluntness has on cone drag are summarised in Figure 6. At the smaller nose bluntnesses the effect on the total drag is relatively minor. The drag shows an increase from the sharp nose value of about 20 % at a nose radius of 7.2 mm (bluntness ratio of 0.144). However, beyond this radius the drag increases more rapidly so that at a nose radius of 18.0 mm (bluntness ratio of 0.36) the value of drag is about 145% greater than the drag on the sharp cone.

A theoretical prediction of the total drag on a sharp cone has been made and is also shown in Figure 6. The pressure drag was predicted using Taylor-Maccoll theory (Taylor and Maccoll, 1932) and found to be 159 N for the case being studied here. An estimate for the skin friction drag on the cone was made based on laminar boundary layer theory (White, 1974) and found to be 36 N. This gives a total drag of 195 N for a sharp, 5° semi-vertex angle and 571.5 mm long cone travelling in air at the 14 MJ/kg condition (Table 1). The value of drag measured for the sharp cone was 200 N, thus reinforcing the accuracy of the drag measurement technique used.

3.3 Drag Force on Scramjet Vehicle

This model provides a good test of the utility of the deconvolution force balance given the complexity and size of the model. All previous studies using the deconvolution balance have been on simpler conical geometries (Sanderson and Simmons, 1991; Porter et al, 1992). The present model deviates from axisymmetry in the arrangement of the scramjet engine modules around the central body of the vehicle. All net aerodynamic forces should be axial for these zero incidence tests. These tests were performed to measure the aerodynamic drag associated with the scramjet vehicle design, thus there was no injection of fuel into the scramjet ducts.

The first step in testing the applicability of the deconvolution force balance to drag measurement on

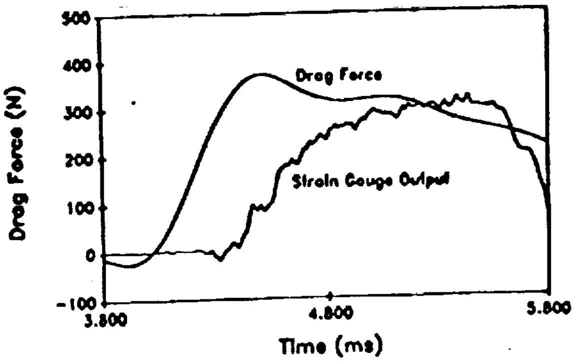

Figure 5. Comparison between signal from strain gauge bridge before (raw signal) and after (drag force) deconvolution for a nose radius of 10.8 mm.

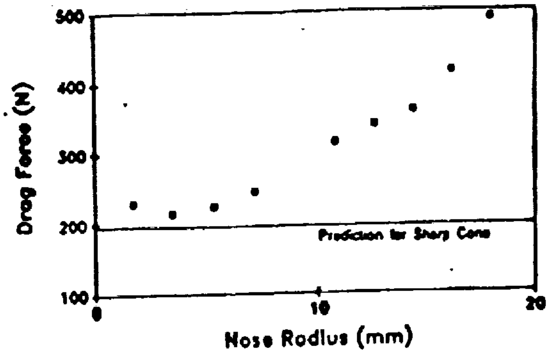

Figure 6. Drag force versus nose radius.

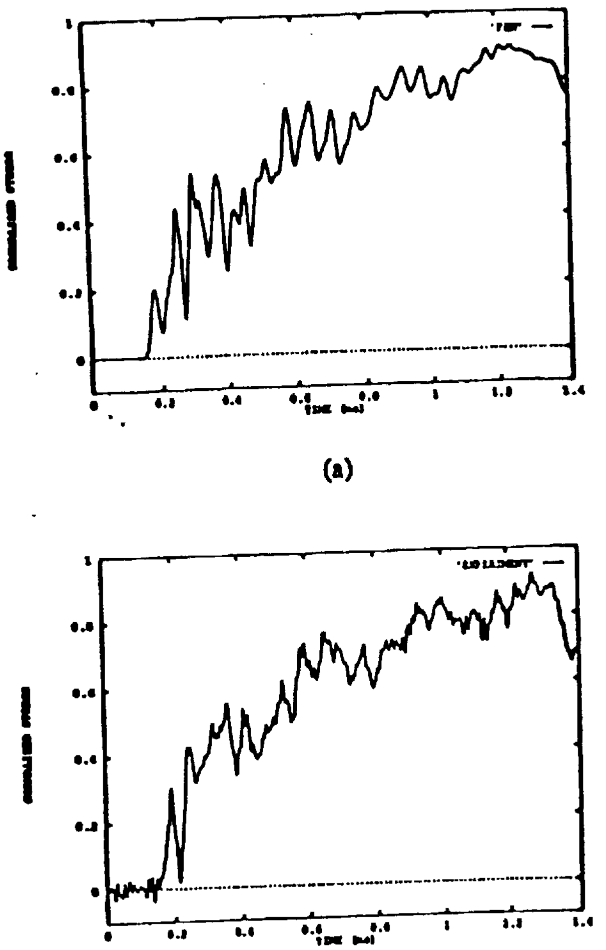

(a)

(b)

Figure 7. Comparison between (a) numerically predicted and (b) experimentally measured step response for a point load applied to the tip of the scramjet vehicle.

the complicated scramjet model involved comparison of a finite element computation of the step response of the model with an experimental result. The finite element computation was performed for an impulsively applied point load at the tip of the model. The experimental step response was obtained by cutting a wire attaching a mass to the tip of the model as in Sanderson and Simmons (1991). This simulates a point load applied impulsively to the tip of the model. Six experimental results were averaged in order to reduce the level of random noise on the signals. The results for the computation and experiment are shown in Figure 7. In these plots the stresses are normalized with the stress that is obtained for a static application of the load to the tip.

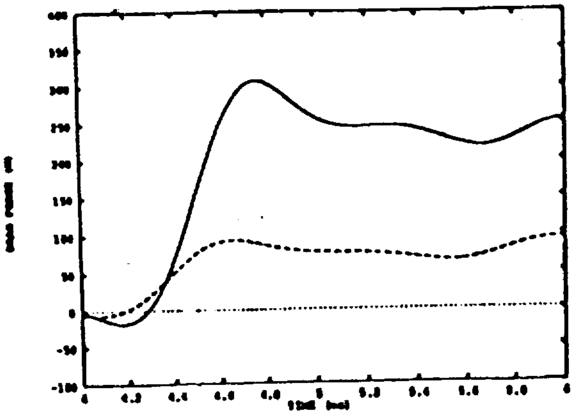

Figure 8. Comparison between the drag time histories on the scramjet model in a flow of nominally 3 MJ/kg and two static pressures. The solid line represents the drag at a static pressure of 10 kPa and the dashed line represents the drag at a static pressure of 3.5 kPa.

The results show that the finite element computation predicts the experiments quite well. The overall rise in the level of stress in the sting is well captured although there are some differences in the finer detail. Based on this result the computed step response has been used to determine the impulse response for use in deconvolution of the measured results.

Figure 8 shows time-histories of the deconvoluted drag on the scramjet vehicle at the low enthalpy conditions of nominally 3 MJ/kg of Table 1. Results are shown for the two different pressure levels at this enthalpy. The results show the characteristic peak in drag at the start of the test flow which is attributed to the starting up process of the nozzle, followed by a period of relatively steady overall force. This is also evident in the cone drag data. The period of steady drag force corresponds to the steady flow test time. Thus, it would appear that the deconvolution balance is suitable for testing complex models such as the present scramjet vehicle.

Condition	Drag (N)	Drag Coefficient
A	370	0.33
B	360	0.31
C	250	0.21
D	80	0.20

Table 2. Drag coefficients of scramjet vehicle at the 4 conditions of Table 1.

The drag coefficients (based on the external cowl radius) corresponding to the four test conditions of Table 1 ranged from 0.20 to 0.33 (Table 2). These relatively high values are attributed to a lack of pressure recovery downstream of the combustion ducts.

4 Conclusion

The drag measurements made on the 5° semi-vertex angle, variable nose bluntness cone model reveal a steadily increasing effect of nose bluntness on drag on the cone. The effect at the smaller nose bluntnesses is relatively small, with a 20% increase in drag at a nose radius of 7.2 mm. This is encouraging for the design of a hypersonic space plane or a centrebody for an axisymmetric scramjet where a slightly blunted nose is required to reduce stagnation point heating. Beyond this nose radius the drag increases more rapidly with nose bluntness.

The results for the scramjet powered vehicle indicate that the deconvolution force balance can be applied successfully to measure the drag on models of quite complex geometry. It is envisaged that a more comprehensive investigation into possible real gas effects on the nose bluntness effects on cone drag will then be applied to the optimal design of the forebody of a scramjet vehicle. The testing of various designs can then be carried out using the deconvolution force balance.

5. Acknowledgements

The authors are grateful for the support received from the Australian Research Council under grant AE9032029 and the Queen Elizabeth II Fellowship Scheme (for Dr. D. Mee).

6 References

LORDI, J A, MATES, R E and MOSELLE, J R (1966) Computer program for numerical solution of nonequilibrium expansion of reacting gas mixtures. NASA CR-472.

McINTOSH, M K (1968) Computer program for the numerical calculation of frozen and equilibrium conditions in shock tunnels. Dept. of Phys. ANU, Canberra.

PORTER, L.M., MEE, D. J. and SIMMONS, J. M. (1992) Measuring the effect on drag produced by nose bluntness on a cone in hypervelocity flow. Eleventh Australasian Fluid Mechanics Conference, Hobart, Australia, 14 - 18 December, pp 287 - 290.

SANDERSON, S R and SIMMONS, J M (1991) Drag balance for hypervelocity impulse facilities. AIAA J., 29, 2185-2191.

SIMMONS, J M, DANIEL, W J, MEE, D J and TUTTLE, S L (1992) Force measurement in hypervelocity impulse facilities. Proceedings of Workshop on New Trends in Instrumentation for Hypersonic Research, ONERA Le Fauga - Mauzac, France, 27 April to 1 May.

STALKER, R. J. (1992) Scaling Laws and the Launch Vehicle Market. Seventh National Space Engineering Symposium, Canberra, Australia, September 21 - 26.

STALKER, R J and MORGAN, R G (1988) The University of Queensland Free Piston Shock Tunnel T4 - Initial Operation and Preliminary Calibration. NASA CR-181721, Sept. 1988.

TAYLOR, G I and MACCOLL, J W (1932) The air pressure on a cone moving at high speed - I Proc. Royal Soc. (London) Ser. A 139, 278-297.

WHITE, F M (1974) Viscous Fluid Flow. McGraw-Hill, Inc., New York., Inc., New York.

N95- 25395 S1-07

1995118975 45348

p. 4

THRUST MEASUREMENTS OF A COMPLETE AXISYMMETRIC SCRAMJET IN AN IMPULSE FACILITY

A. Paull, R. J. Stalker and D. Mee
Mechanical Engineering Department
University of Queensland
Australia

ABSTRACT

This paper describes tests which where conducted in the hypersonic impulse facility T4 on a fully integrated axisymmetric scramjet configuration. In these tests the net force on the scramjet vehicle was measured using a deconvolution force balance. This measurement technique and its application to a complex model such as the scramjet are discussed. Results are presented for the scramjet's aerodynamic drag and the net force on the scramjet when fuel is injected into the combustion chambers. It is shown that a scramjet using a hydrogen-silane fuel produces greater thrust than its aerodynamic drag at flight speeds equivalent to 2600 m/s.

INTRODUCTION

Extensive investigations, both numerical and experimental, have been conducted to determine if scramjets produce sufficient thrust to be economically viable for hypersonic flight. Although these investigations are important, the most definitive way to determine the viability of a scramjet is to perform flight tests with a fully integrated configuration. That is to say, flight tests of a scramjet with intakes, combustion chambers, thrust surfaces and exterior surfaces.
Flight tests can be made in two ways. A scramjet could be propelled through the atmosphere with a suitable carrier or alternatively, and what was used for the tests described here, flight tests can be performed in a hypersonic test facility.
The free piston driven shock tunnel T4 was used to test the axisymmetric scramjet seen in figure 1. The drag or net thrust produced by the scramjet was obtained using a deconvolution force balance (Sanderson and Simmons (1991)). The time-history of the force acting on the scramjet is obtained by numerically deconvolving measurements made of the axial strain in a sting attached to the scramjet.
This type of balance was originally designed so that a force could be deconvolved over a period of approximately 1 ms. However, this is insufficient for testing scramjets. An increase in deconvolution time is required because valves are opened and fuel is injected prior to the start of the test flow. To obtain an accurate time history of the force on the scramjet these events must also be deconvolved. The development of this balance and technique to the point where time-history measurements can be made over a period in excess of 10 ms on a complicated model has been crucial to the measurement of the net thrust produced by a scramjet.
The ability to measure the overall performance of a fully integrated scramjet is one which should enhance the design efforts towards the development of this type of engine. The results presented here are the first record of the thrust produced by a fully integrated scramjet which has been tested in an impulse facility.

MODEL DESCRIPTION

A schematic of the scramjet, fuel tank and sting is shown in figure 1. The scramjet is connected to the fuel tank which in tern is connected to the sting. The scramjet is cylindrical in shape with a conical forebody and thrust surface. It has an aluminum centrebody and a stainless steel cowl. The fuel tank is cylindrical in shape and is made from stainless steel. The sting is a brass cylindrical pipe. Semiconductor strain gauges are attached to the sting approximately 200 mm downstream of the fuel tank.
The sting and model are suspended by fine threads so that the combination is free to move in the direction of the axis of the tunnel. The fuel tank and sting are shielded from the test flow. This shielding is required to ensure that the forces which are measured are only the aerodynamic forces acting on the model.
The overall length of the scramjet is 274 mm and its external diameter is 71 mm. The conical forebody has a 9 degree half angle and the thrust surface has a 11 degree half angle.
Six identical combustion chambers are distributed

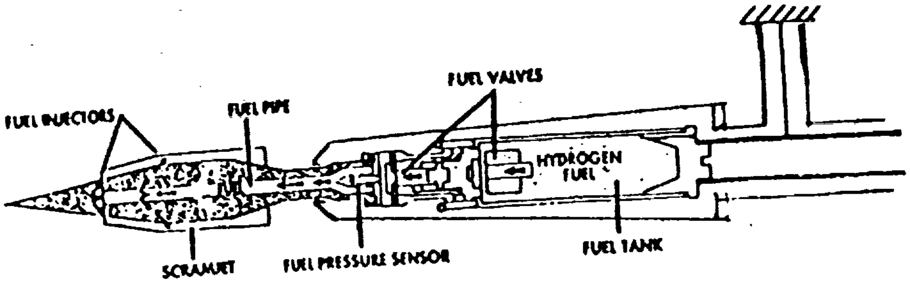

Figure 1. Schematic of the scramjet and its fuel tank.

around the cylindrical centrebody. The combustion chambers are 58.5 mm long and of constant cross-section. The centrebody is cylindrical with a diameter of 51 mm.

A connecting pipe between the model and the fuel tank is 75 mm long. The fuel tank shielding which seals on this pipe starts 55 mm downstream of the end of the thrust surface. Aerodynamic drag on this 55 mm section constitutes part of the drag on the scramjet.

Fuel could be injected upstream of the combustion chamber intakes from injectors located on the conical forebody or from injectors within the intakes positioned at the entrance to the combustion chambers. In the tests described here, fuel was injected only from the injectors located at the entrance to the combustion chambers. The upstream injectors were plugged.

In each combustion chamber there is one injector. Each injector is a 2mm orifice angled at 30 degrees to the centreline of the scramjet and located centrally at the entrance to the combustion chamber. Fuel is supplied to the injectors from the fuel tank by means of a pipe through the centrebody of the scramjet.

The fuel pressure is monitored in the fuel pipe as shown in figure 1. This pressure and calibration factors for the injectors are used to determine the mass flow rate of the fuel. It is assumed that the flow through the injectors is choked. The mass flow rate of the fuel is varied by changing filling pressure of the fuel tank.

Fuel flow is controlled by a fast acting valve located between the scramjet and the fuel tank. The valve fully opens in approximately 6 ms (depending on filling pressure) and closes in approximately 100 ms.

THE FORCE MEASUREMENT TECHNIQUE

The force balance used to measure the scramjet's thrust is described in detail by Sanderson and Simmons (1991) and involves determining the time-history of the force acting on the test model by monitoring the axial strain on a long sting attached to the base of the model. When the flow starts around the model the resulting aerodynamic forces cause stress waves to propagate and reflect within the model and fuel tank. These waves are transmitted into the sting and are monitored by the strain gauges. Such a system can be modelled as a linear system characterized by an input $u(t)$ - the axial force on the model, an output $y(t)$ - the strain measured in the sting and an impulse response $g(t)$ relating the two. This can be written using a convolution integral,

$$y(t) = \int_0^t g(t-\tau)\, u(\tau)\, d\tau. \qquad (1)$$

When the impulse response and the output are known, deconvolution techniques can be used to solve the inverse problem to find the time-history of the axial force on the model.

The impulse response which characterizes the system can be found either experimentally or by using dynamic finite element analysis. For the present tests an experimentally determined impulse response has been used. This was found by suspending the model and sting by a fine wire attached to the tip of the conical forebody of the scramjet. The wire was then cut close to the tip of the forebody to produce a sudden removal of a tensile load. This is equivalent to a step-like drag load applied at the tip of the model. The resulting strain gauge output (figure 2) measured in the sting gives the step response for the system. The impulse response is then found by differentiating the step response with respect to time.

The opening of the fuel valve a few milliseconds before the arrival of the test flow added some complications to the force balance measurement technique not previously encountered. Previously (Sanderson and Simmons (1991)) strain gauge signals

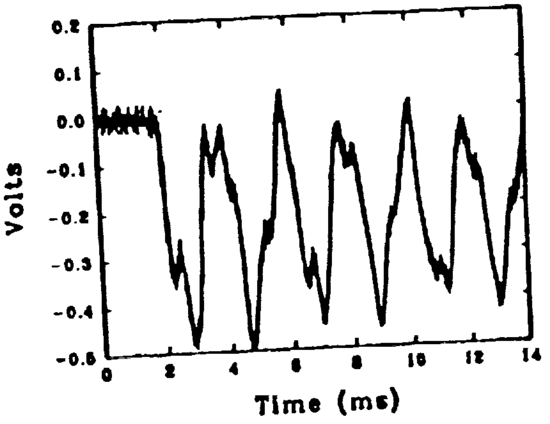

Figure 2. Strain gauge output as a function of time for a unit step load applied to the scramjet nose.

had only been processed to the point in time at which waves that reflected from the downstream end of the sting returned to the measurement location. However, it was found in the work of Porter et.al. (1993) that signals could be processed beyond this time provided that an impulse response was used which included characterization of these reflected waves. Since the opening of the fuel valves causes an output on the strain gauge signal it became imperative in the present tests that signals could be deconvolved through a number of stress wave reflections.

FUEL DESCRIPTION

Initially, hydrogen was used as the fuel, however, it was observed that very little thrust was obtained. It is believed that the combustion chambers are too short for the fuel to fully combust at the conditions targeted. To reduce the combustion length, silane (SiH_4) was added to the hydrogen. 13% of the fuel's volume was silane. Fuel was injected at an equivalence ratio of 0.8.

A typical record of the fuel pressure is given in figure 3. It can be seen that the fuel pressure is constant during the test time. The fuel pressure remains constant for approximately 3 ms, after which it falls rapidly as the fuel is drained from the fuel tank. It is critical that the fuel valve is opened so that this 3 ms period is coincident with the test flow. Ideally, the fuel pressure should reach its maximum approximately 0.5 ms before the test flow arrives. If fuel is injected early then the mass flow rate of the fuel will not be steady and furthermore, the time-history of the strain induced into the sting from the injection of fuel may not be fully recorded or will be excessively long. Consequently, the force on the scramjet could not be properly deconvolved.

RESULTS

Figures 3, 4, 5 and 6 display the measurements made during the tests. Time t=0 on all figures represents the same time during the tests. The flow arrives at the test section at t = 0.5 ms.

FLOW PROPERTIES

In the operation of a reflected shock tunnel the test gas is first shock heated and is then expanded through a contoured nozzle. The temperature of the test gas after it is heated but before it is expanded is determined using ESTC (McIntosh (1968)) to be 2700 K. Properties of the test gas in the test section are then determined using NENZF (Lordi et.al.(1966)). In the experiments described here it is assume that the test gas is in chemical equilibrium as it expands down the nozzle. It has been determined that, in the test section, the test gas has a velocity of 2400 m/s, a density of 0.09 kg/m^3, and a temperature of 350 K. The total enthalpy of the flow is 3.3 MJ/kg and therefore is equivalent to a flight speed of 2600 m/s.

Figure 4 displays measurements made of the static and Pitot pressures. It can be seen that the test flow establishes itself approximately 0.5 ms after the arrival of the first shock. Subsequently, the flow is quasi-steady for approximately 1.5 ms.

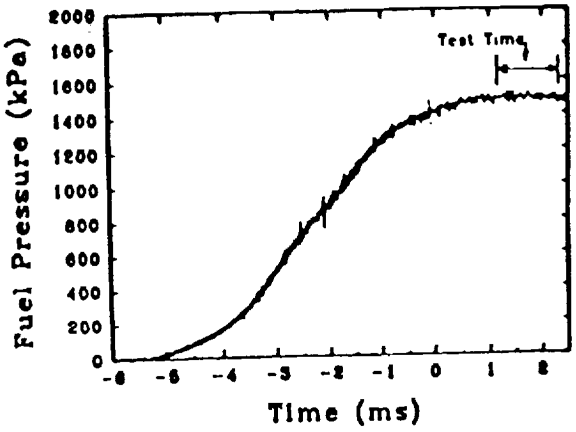

Figure 3. Fuel pressure as a function of time.

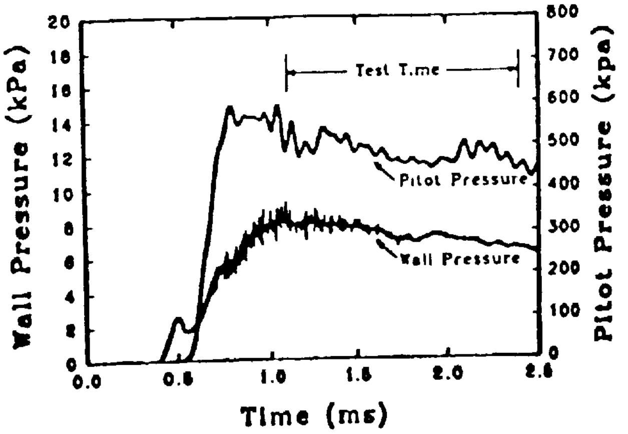

Figure 4. Wall and Pilot pressure as a function of time.

FORCE MEASUREMENTS

Figure 5 displays the output from the strain gauge mounted on the sting. The thrust produced by the injection of the fuel is observed as a relatively slow oscillation prior to the arrival of the test gas. When the test flow arrives it can be observed that the output is more complex.

The output in Figure 5 is deconvolved using the unit impulse response function to obtain the time-history of the net force on the scramjet. The result of this deconvolution is displayed in Figure 6.

Figure 6 displays three such deconvolved time-histories. These are the net forces on the scramjet when

(i) fuel is injected into a test gas of air,

(ii) fuel is injected into a test gas of nitrogen and

(iii) fuel is not injected and the test gas is air.

In the latter case it can be seen that the scramjet experiences a drag-history which basically reflects the slight decay observed in the Pitot pressure (figure 4). It can be seen that the drag is approximately 140±25 N.

When nitrogen is used as a test gas and fuel is injected the drag on the scramjet is approximately 90±20 N. Hence, the drag is approximately 50 N less than the fuel off test in air. There is a slight difference in flow conditions between the air and nitrogen test gases, however, the drag is reduced primarily due to the presence of the fuel. When fuel is injected, it can be seen, prior to the arrival of the test flow, that the fuel induces a thrust of approximately 30 N. It is speculated that the the remaining 20 N reduction in drag results from the different test gases and fuel air interactions which possibly change the skin friction coefficients within the combustion chambers.

Figure 5 also displays the drag and thrust on the scramjet when fuel is injected into air. It can be seen, as above, that prior to the test flow the fuel induces a net thrust of approximately 30 N. As the flow establishes itself across the model the drag increases, following closely the result obtained with the nitrogen test gas. However, once the flow is established ignition of the fuel occurs and the drag is substantially reduced. 200 μs after flow establishment the thrust created by the combustion of the fuel is sufficient to balance the drag. 1 ms after flow establishment and during the test time the net thrust is approximately 50 N. During the test time the net thrust peeks at approximately 95 N and is always greater than 40 N.

CONCLUSIONS

The impulsive force balance and the deconvolution techniques described in this paper are sufficiently advanced to measure the net force on a complicated model.

The use of an experimentally determined unit impulse response function has made it possible to determine with good frequency response the net force time-history on a model such as the scramjet, where the time-history of the forces applied to the model are of the order of 10 ms.

The scramjet used in these tests, although producing more thrust than drag, will need to be more efficient to become viable. The technique described above has made it possible to test new designs in hypersonic impulse facilities. Thus, definitive values for overall performance of scramjet designs can now be obtained relatively simply and cheaply at hypersonic conditions.

ACKNOWLEDGEMENTS

This work was complete under grants supplied by the Australian Research Council and NASA Langley Research Center.

BIBLIOGRAPHY

Lordi, J.A., Mates, R.E. and Moselle, J.R. 1966, Computer program for numerical solution of nonequilibrium expansion of reacting gas mixtures. NASA CR-472.

McIntosh, M.K. 1968, Computer program for the numerical calculation of frozen and equilibrium conditions in shock tunnels. Dept. of Physics, A.N.U. Australia.

Porter, L., Paull, A. and Mee, D. 1993, Measuring the effect of nose bluntness on drag on a cone in a hypervelocity shock tunnel facility. HF1, 19th ISSW 1993.

Sanderson, S.R. and Simmons, J.M. 1991, Drag balance for hypervelocity impulse facilities. AIAA J., 2185-2191.

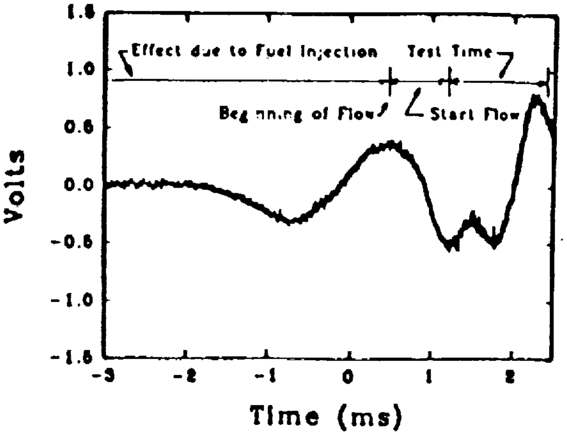

Figure 5. Strain gauge output as a function of time. Fuel injected into air

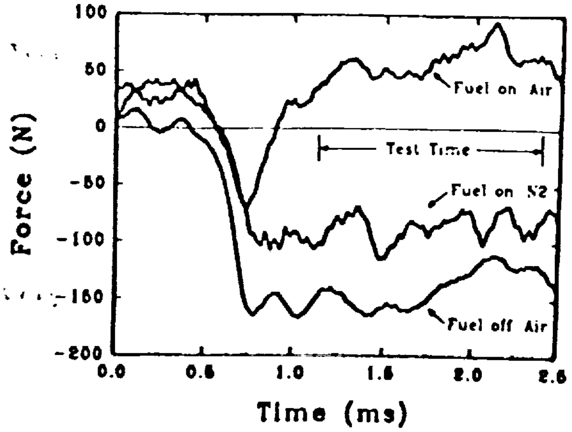

Figure 6. Net force on the scramjet as a function of time when fuel is injected into air and nitrogen test gases and when fuel is not injected and the test gas is air.

S2-07
5349
P- 9

SCRAMJET THRUST MEASUREMENT IN A SHOCK TUNNEL

N95- 25396

[1]A. Paull, [2]R.J. Stalker & [3]D.J. Mee

Department of Mechanical Engineering, The University of Queensland, Brisbane, 4072
Australia

1995 118976

INTRODUCTION

This note reports tests in a shock tunnel in which a fully integrated scramjet configuration produced net thrust. The experiments not only showed that impulse facilities can be used for assessing thrust performance, but also were a demonstration of the application of a new technique (1) to the measurement of thrust on scramjet configurations in shock tunnels. These two developments are of significance because scramjets are expected to operate at speeds well in excess of 2 km/sec, and shock tunnels offer a means of generating high Mach number flows at such speeds.

THE MODEL AND TEST FACILITY

A sketch of the scramjet model and fuel tank is shown in Figure 1. The scramjet centrebody, shown in streamwise section in the figure, consisted of a conical forebody with 9° half angle, a cylindrical section of 51 mm diameter, and an afterbody of 10° half angle. It was partly surrounded by a axisymmetric cowl, which had an internal diameter of 67 mm over the parallel section of the centrebody, and was of 71 mm outside diameter. Filler pieces, which are not shown, divided this parallel section into six constant area combustion chambers, each of which subtended an angle of 26° at the centreline. Fuel was injected through six orifices, each 2 mm in diameter and angled at 30° to the centreline. They were located at the upstream end of the combustion

---

[1] Research Fellow

[2] Professor of Space Engineering, Member AIAA

[3] Lecturer

chambers. The filler pieces between the combustion chambers extended upstream in the form of intake compression ramps which processed the flow in the forebody shock layer through two shocks, each of 8° deflection. The leading edges of the cowl were shaped to prevent these shocks spilling from the intake, thus forming a convergent duct leading to the combustion chambers. The radial dimension of this duct was 10 mm.

The fuel supply system is also shown in the figure. The fuel tank was filled before a test, and the supply valve remained closed until the test was initiated. The recoil of the shock tunnel closed a switch to operate the solenoid valve, which opened the supply valve. As the fuel flowed to the model and fuel injection orifices, its pressure was monitored by a PCB piezoelectric pressure transducer. The system was designed so that sonic flow occurred at the orifices. As shown, the fuel tank and valve assembly was shielded from the flow by an aerodynamic shroud. In normal operation, the upstream end of this shroud was located 50 mm downstream of the termination of the scramjet afterbody, and to check that this was sufficient for the shroud to have no influence on the forces on the scramjet, a test was run with an insert to increase this distance to 125 mm. No change in the measured force was observed.

The experiments were done in the free piston shock tunnel T4 at the University of Queensland which had a shock tube 10 m long and 76 mm in diameter. A mixture of Argon with Helium was used as the driver gas, and the ratio of the two was varied as the stagnation enthalpy was varied to ensure that a sufficient period of approximately constant nozzle stagnation pressure was maintained throughout the tests. The contoured hypersonic nozzle used for the tests had a throat diameter of 25 mm and a test section diameter of 250 mm, and was operated with a reservoir pressure of 37.5 ± 2.5 MPa.

THE STRESS WAVE FORCE BALANCE

A stress wave force balance, as originally outlined in ref 1 by Sanderson and Simmons, was used to measure the axial force on the model. They employed the method to measure the drag on a short cone, but it has since been developed for longer cones (2), and for long cones with the load distribution imparted by a blunt nose (3). Essentially, it involves measurement by a strain gauge of the time variation of stress induced in a stress wave bar by the forces on the model, and deconvolution of the resultant record to obtain the net force on the model. As shown in Figure 1, the stress wave bar was attached to the downstream end of the fuel tank, and the strain gauge was mounted some 250 mm from the junction. The stress bar was free at the downstream end and was suspended by wires, which did not influence the propagation of stress waves.

The relation between the force input u(t) and the strain gauge output y(t) can be written by using the impulse response g(t) relating the two, as

$$y(t) = \int_0^t g(t - \tau)\, u(\tau)\, d\tau \quad .$$

Dynamic finite element computer simulations showed that the sum of the forces distributed along the length of the model could be accurately represented by a single force applied at the nose, so the required g(t) was obtained experimentally by vertically suspending the model and stress wave bar by a fine wire from the tip of the forebody, and suddenly severing the wire. The resulting strain gauge response was then differentiated with respect to time to find g(t). It was necessary to establish g(t) for a period of several milliseconds, in order to accomodate the generation of thrust by fuel injection before the initiation of the test flow. As the stress wave bar was only 2 m long, and was made of brass, this implied that the impulse response included stress wave reflections in the bar.

A computer program was prepared to deconvolute the above integral with this g(t) and applied to yield the axial force for each test.

EXPERIMENTS AND RESULTS

The experiments were conducted with a fuel consisting of 13% silane (SiH_4) and 87% hydrogen by volume, yielding typical results as displayed in Figure 2 [(4)]. Figure 2(a) displays the pitot pressure and static pressure of the free stream measured during a test, showing that the flow reaches an approximately quasi-steady state about 0.5 milliseconds after first arrival at the test section, and that state subsequently persists for approximately 1 millisecond. Records of the axial force experienced by the scramjet are displayed in Figure 2(b). It can be seen that with no fuel injection, the scramjet experiences a drag force of 140 ± 25 N. When nitrogen is used as the test gas, and fuel is added, the drag on the scramjet is reduced substantially. The test conditions with nitrogen differ only slightly from those with air, so most of the difference is attributed to the thrust due to fuel injection alone. When the fuel is injected into air, it can be seen that, prior to arrival of the test flow, the fuel produces a thrust of approximately 40 N, and as the flow about the model establishes itself the drag increases, closely following the nitrogen result. However, once air flow through the combustion chambers allows ignition of the fuel, the thrust due to combustion increases until, during the test time, it is sufficient to produce a net thrust on the scramjet of more than 50 N.

The variation of the thrust with tunnel stagnation enthalpy, or with the computed test section velocity (5), is shown in Figure 3. It can be seen that although the net thrust is positive around stagnation enthalpies of 3 MJ/kg, it falls off rapidly with increasing stagnation enthalpy. It is thought that this is largely due to the dissociation of combustion products in the combustion chamber. An attempt was made to increase the maximum thrust measured by either increasing the amount of fuel injected, or by lowering the tunnel stagnation enthalpy. In both cases unsteadiness in the flow resulted, suggesting the onset of thermal choking.

In order to confirm that the flow in the combustors was supersonic when combustion was taking place, pitot and static pressures were measured at the downstream end of one of the ducts just upstream of the expansion caused by the upstream corner of the afterbody. At a stagnation enthalpy of 3.3 MJ/kg the ratio of the two was 4.1, yielding a Mach number of 1.75 ± 0.1.

The performance of the scramjet configuration tested was not impressive, as the maximum observed net thrust of 60 N corresponded to a fuel specific impulse of only 200 seconds. However, no serious attempt was made to optimise the configuration for net thrust, as is witnessed by a fuel-off drag co-efficient of 0.13 at a stagnation enthalpy of 3 MJ/kg. Substantial improvements may be expected from proper attention to aerodynamic design.

ACKNOWLEDGMENTS

The authors would like to express their appreciation of the support provided by the Australian Research Council, and through NASA grant NAGW-674.

REFERENCES

1. Sanderson, S.R. and Simmons, J.M. "Drag Balance for Hypervelocity Impulse Facilities" AIAA Journal, Vol 29, December 1991, pp 2185-2191.
2. Simmons, J.M., Daniel, W.D., Mee, D.J., and Tuttle, S.L. "Force Measurement in Hypervelocity Impulse Facilities" New Trends in Instrumentation for Hypersonic Research (ed. A. Boutier), 1993, Kluwer Academic Publishers, Amsterdam pp 285-294.
3. Porter, L.M., Mee, D.J., and Simmons, J.M. "Measuring the Effect on Drag Produced by Nose Bluntness on a Cone in Hypervelocity Flow" Proc. 11th Australasian Fluid Mechanics Conference (ed. M. Davis & G. Walker), University of Tasmania, Hobart, Australia, 14-18 December, 1992, pp 287-290.
4. Paull, A., Stalker, R.J. and Mee, D.J. "Thrust Measurements of a Complete Axisymmetric Scramjet in an Impulse Facility". AIAA paper no. 93-5168. AIAA/DGLR Fifth International Aerospace Planes and Hypersonics Technologies Conference, Munich, Germany, 30 Nov-3Dec , 1993.
5. Lordi, J.A., Mates, R.E. and Moselle, J.R., "Computer Program for Numerical Solution of Non-equilibrium Expansion of Reacting Gas Mixtures" NASA CR-472, 1966.

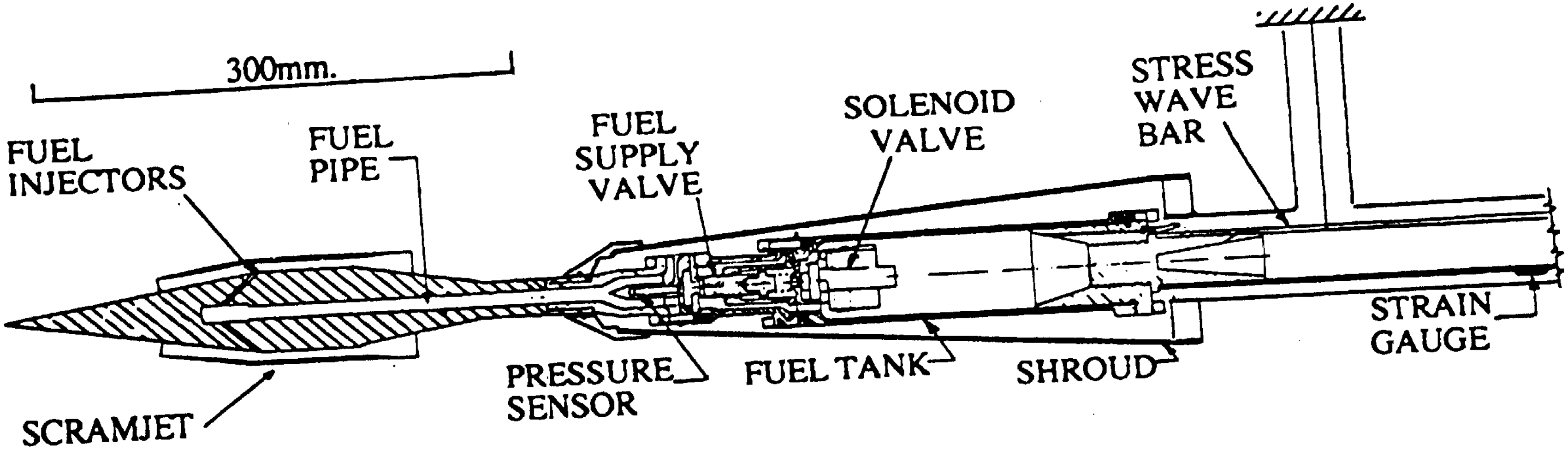

FIGURE 1. SCRAMJET MODEL AND FUEL TANK ASSEMBLY

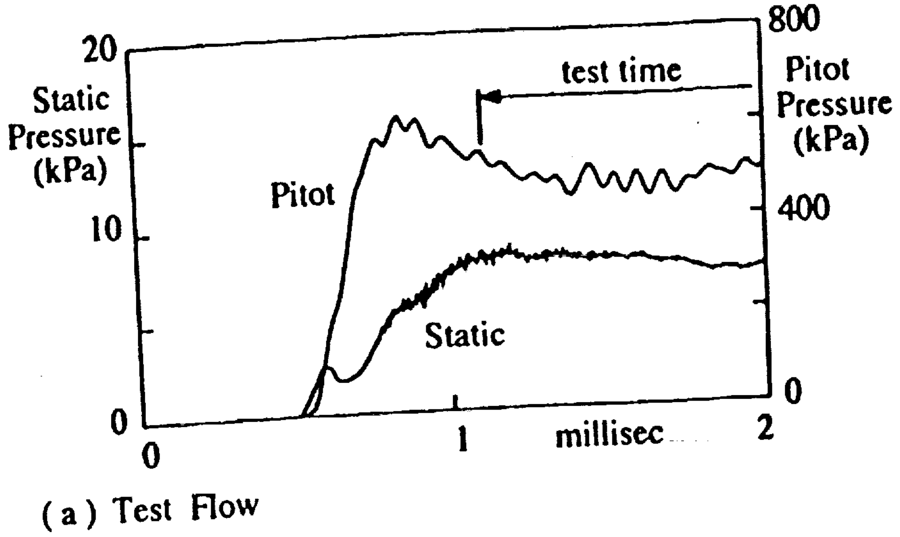

(a) Test Flow

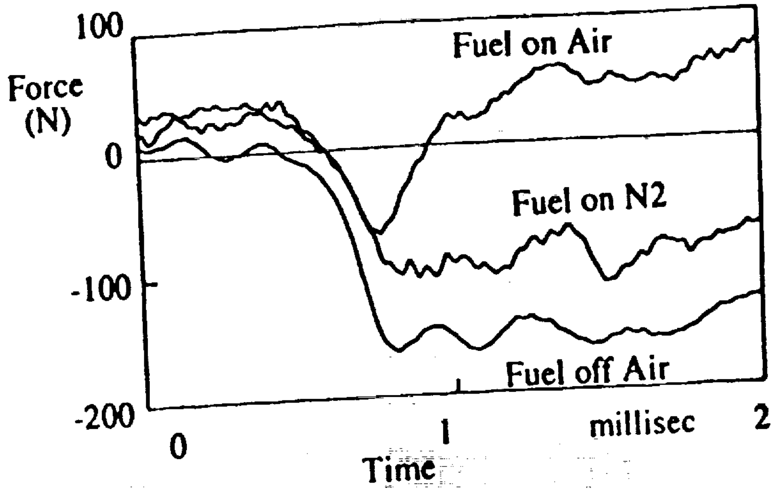

(b) Axial Force on Model

FIGURE 2. TEST RECORDS SHOWING GENERATION OF NET THRUST (STAGNATION ENTHALPY = 3.2 MJ/KG, FUEL/AIR EQUIVALENCE RATIO = 0.90)

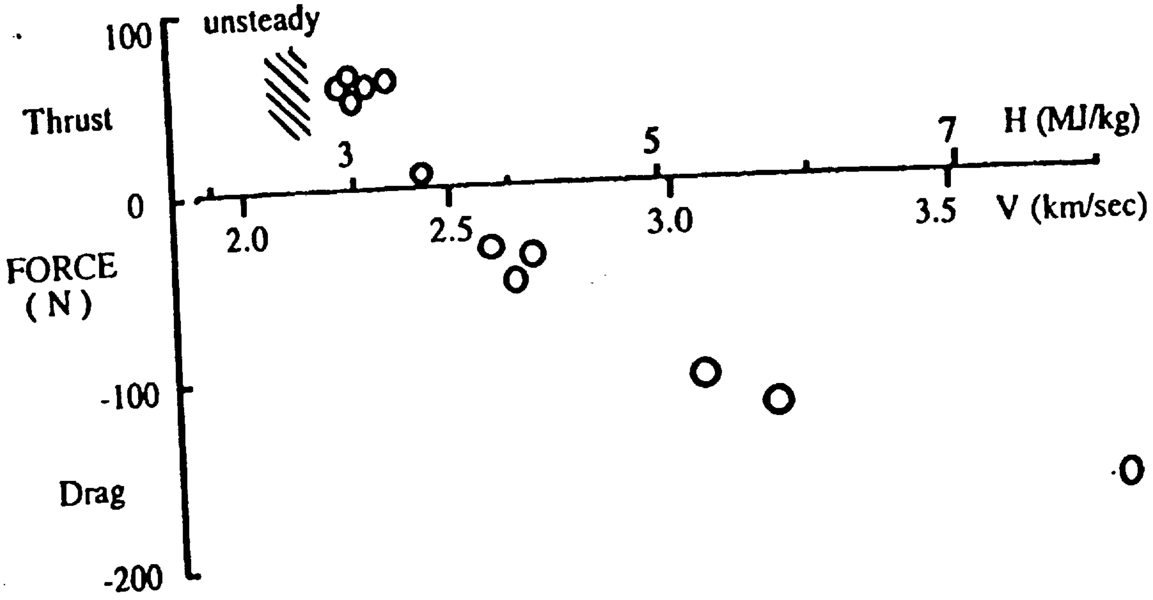

FIGURE 3. MEASURED AXIAL FORCE ON SCRAMJET MODEL WITH FUEL INJECTION.

(H = STAGNATION ENTHALPY, V = TEST SECTION VELOCITY, FUEL 87% H_2 13% SI H_4, EQUIVALENCE RATIO = 0.83 ± 0.07. MACH NUMBER = 6.6 TO 5.6)

N95- 25397

S3-07

45350

Thrust measurement in a 2-D scramjet nozzle - Sean Tuttle

1995 118977

P- 8

Supervisors: J.M Simmons, D.J. Mee

The two-dimensional thrust nozzle presents a challenging problem. The loading is not axisymmetric as in the case of a cone and the internal flow presents some design difficulties. A two-sting system has been chosen to accommodate the internal flow and achieve some symmetry. This can be seen in Figure 1. The nozzle is 300 mm long and together the nozzle and stings weigh 6.55 kg. The angle of the ramp walls is 11° and the area ratio is 4.76.

The situation is complicated by the fact that with the small ramp angle and the internal pressure on the nozzle walls, loading is predominantly transverse. Yet it is the axial thrust which is to be measured (i.e. the tensile waves propagating in the stings). Although bending stress waves travel at most at only 60% of the speed of the axial stress waves, the system needs to be stiffened against bending. The second sting was originally only used to preserve symmetry. However, the pressures on each thrust surface may be quite different at some conditions, so at this stage the signals from both stings are being averaged as a first order approximation of the net thrust. The expected axial thrust from this nozzle is not large so thin stings are required. In addition to this, the contact area between nozzle and sting needs to be maximised. The result was that it was decided to twist the stings through 90°, without distorting their cross-sectional shape, just aft of the nozzle.

Finite element analysis showed that this would not significantly alter the propagation of the axial stress wave in the sting, while the rigidity of the system is greatly increased.

Figure 2 shows the numerically predicted response of the nozzle to a step point load and the experimentally measured step response to a point load. The results indicate that the speed of response of the balance is adequate.

The 300 mm long nozzle is freely suspended behind a fixed scramjet combustor. A 3 mm lip at the exit of the combustor will ensure there is no flow leakage, while simultaneously allowing free movement of the nozzle and stings. Around the perimeter of the lip there is approximately 0.5 mm of clearance with the nozzle. This is shown in Figure 3. The alignment of the nozzle behind the combustor has been one of the challenges of this experiment. Sufficient free movement is required to measure signals of a useful duration (production of positive thrust will accelerate the nozzle towards the combustor) while flow leakage onto the front face of the nozzle is undesirable.

The stings are mounted into the top surface of the nozzle ramp walls in order to keep them out of the nozzle exit plane (see Figure 3).

There are static pressure tappings in the ramp walls of the nozzle and a pitot rake provides a survey of the flow at the exit of the nozzle. Combustor static pressures are also measured, and shots are repeated with the nozzle removed in order to measure the pitot pressure across the combustor exit. The scramjet is 600 mm long and fuel is injected from a central planar strut.

The thrust measured via the strain gauges will be the net axial load on the nozzle. This should be less than the thrust calculated from static pressure measurements by an amount equal to the skin friction. Figure 4 shows how the static pressures in the nozzle are different on either side for the non-combustion cases at 9 MJ/kg. The open and closed triangles represent the static pressures on one thrust surface for mixing and fuel-off conditions, respectively. The corresponding pressures on the opposite thrust surface are indicated by the open square symbols. It can be seen that there is a significantly different pressure on the first half of each thrust surface when there is no combustion. The open and closed circles depict the pressures on the two thrust surfaces when there is combustion. In this case, the pressure distribution is essentially symmetrical. Figures 5 and 6 show the strain signals measured in each sting for the non-combustion and combustion cases just described. When there is a different pressure on each thrust surface, a different strain is measured in sting. It is for this reason that the strain signals from the two stings are being averaged to obtain the net thrust. However, this is to be further investigated.

The pressures inside the lip region and inside the nozzle shielding have been measured for all conditions. The flow which leaks into these regions only becomes significant approximately 3 milliseconds after the test time.

A Mach 4 contoured nozzle is used in the experiments. In the result shown in Figure 7, the thrust calculated by integrating the static pressure measurements on the on the thrust surfaces is compared with the deconvolved strain measurement of the net thrust for the cases of air only and hydrogen fuel injected into air at approximately 9 MJ/kg nozzle supply enthalpy. At this stage, no attempt has been made to quantify the skin friction. The gain in thrust due to combustion is visible in this result.

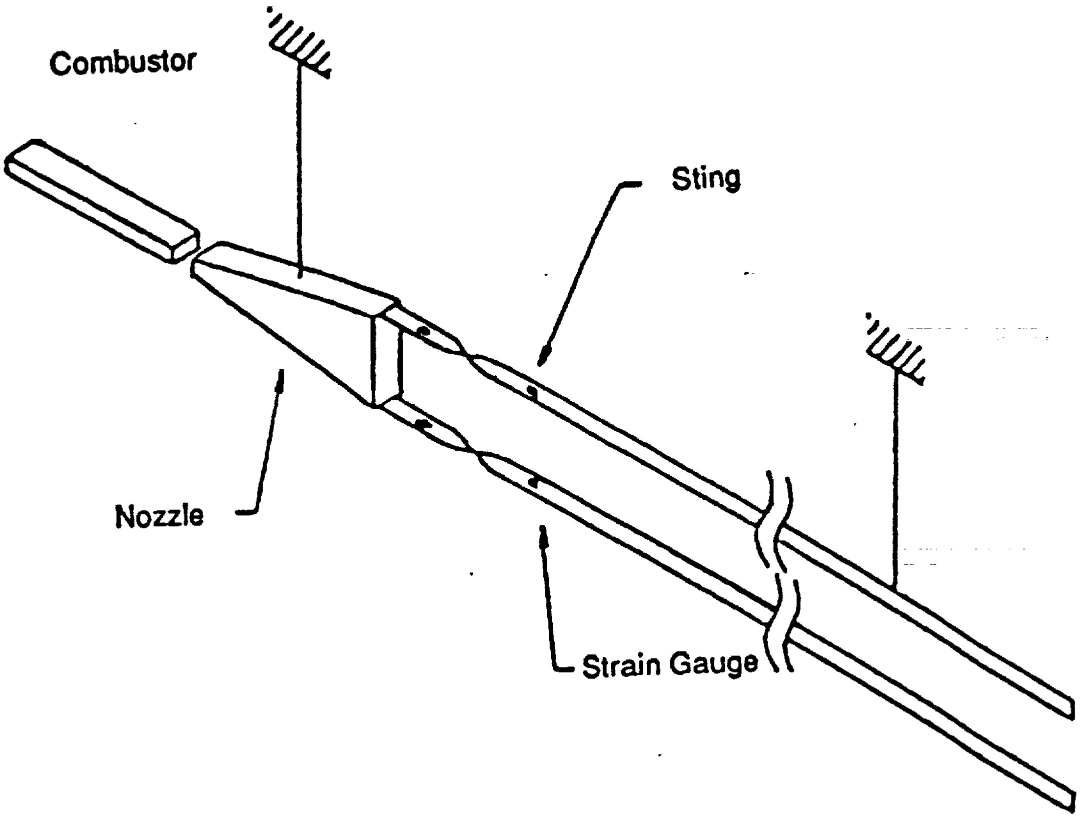

Thrust Nozzle Stress Wave Balance

FIG. 1

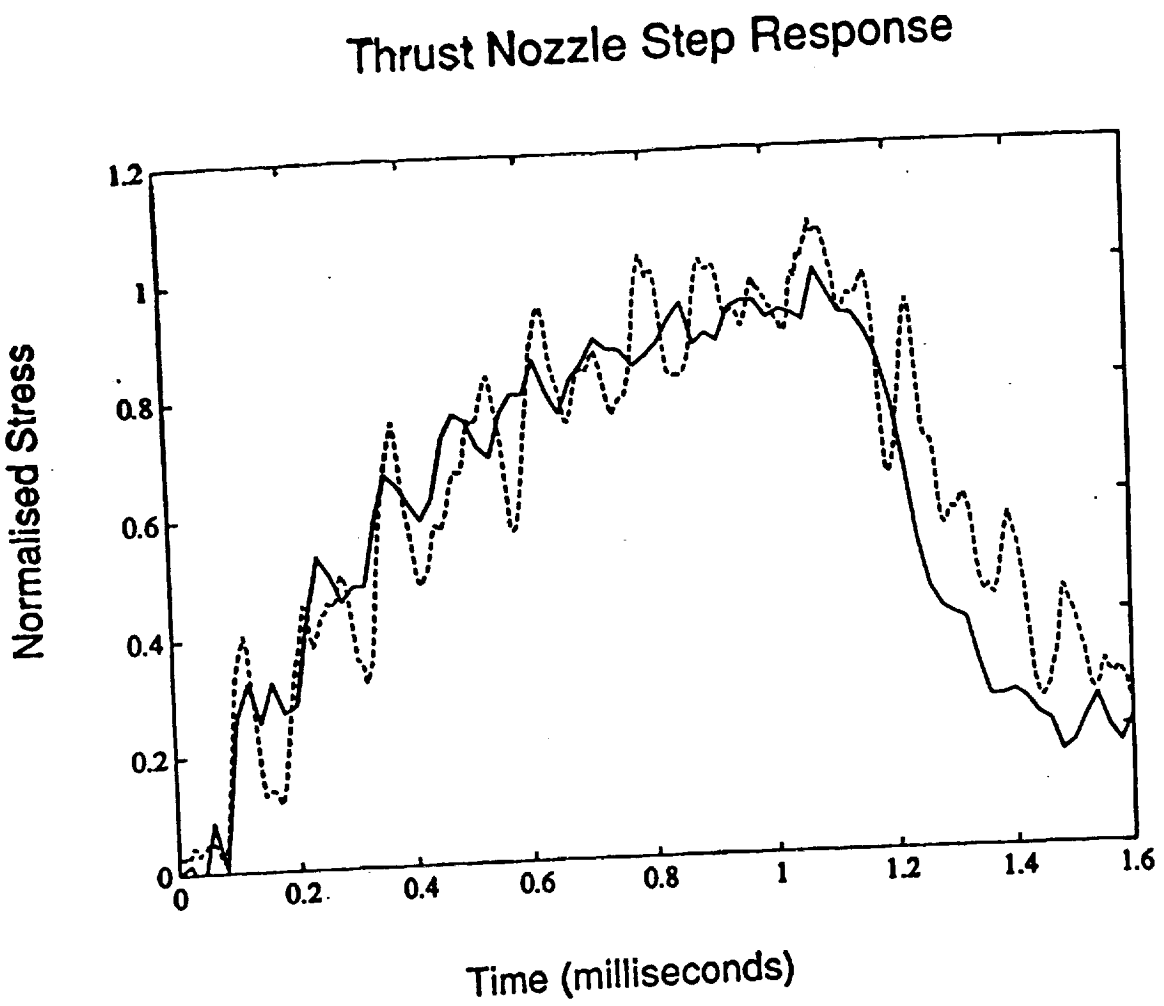
Thrust Nozzle Step Response
Normalised Stress
1.2
1
0.8
0.6
0.4
0.2
0
0
0.2
0.4
0.6
0.8
1
1.2
1.4
1.6
Time (milliseconds)

FIG 2.

Connection between Scramjet Combustor and Thrust Nozzle

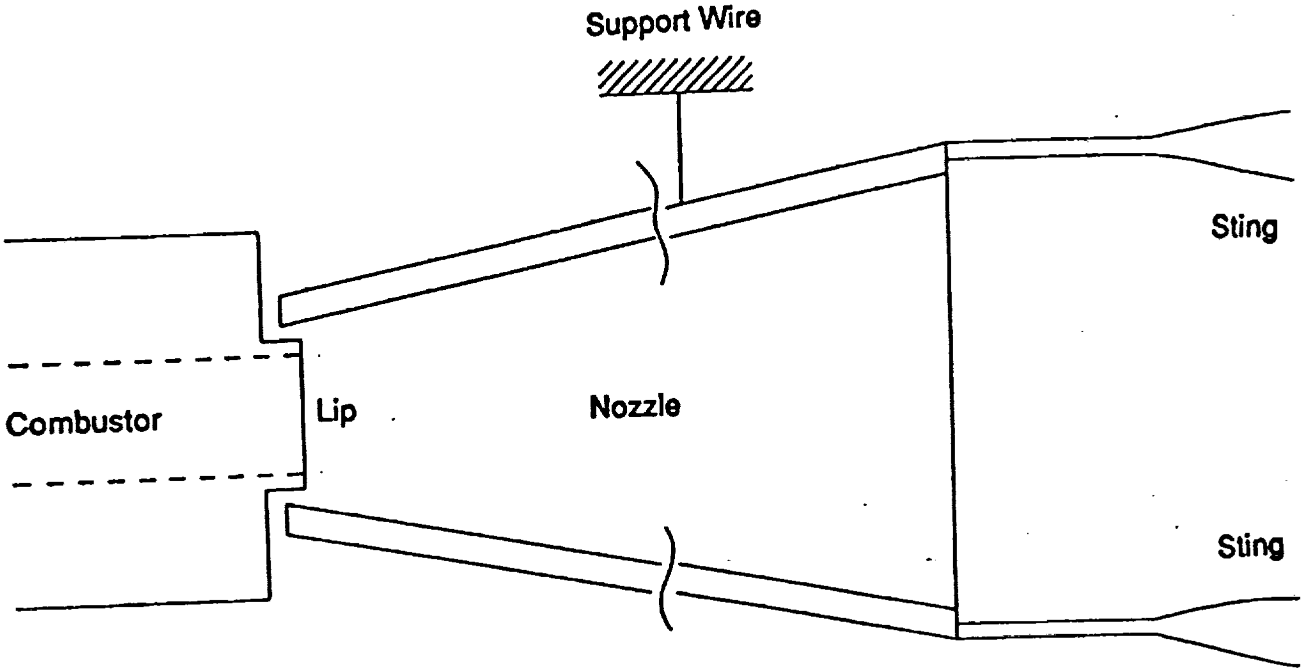

FIG 3.

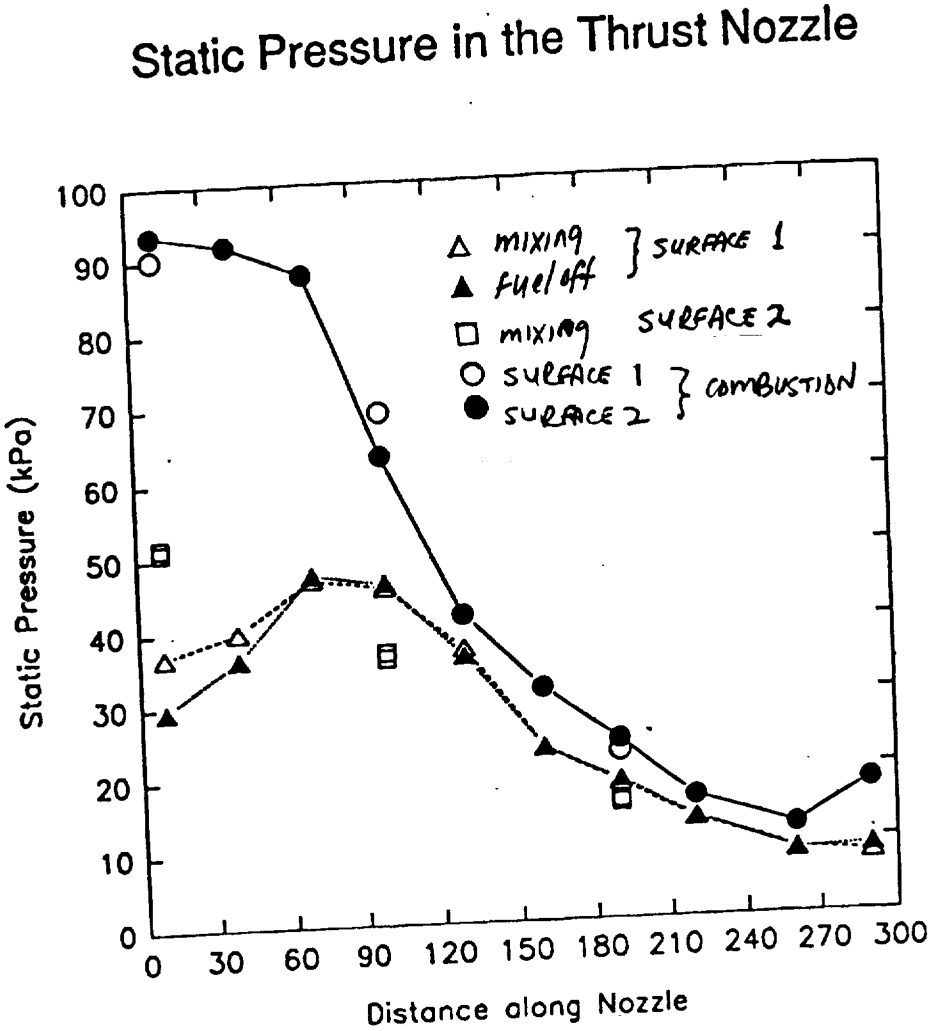

Static Pressure in the Thrust Nozzle

FIG. 4

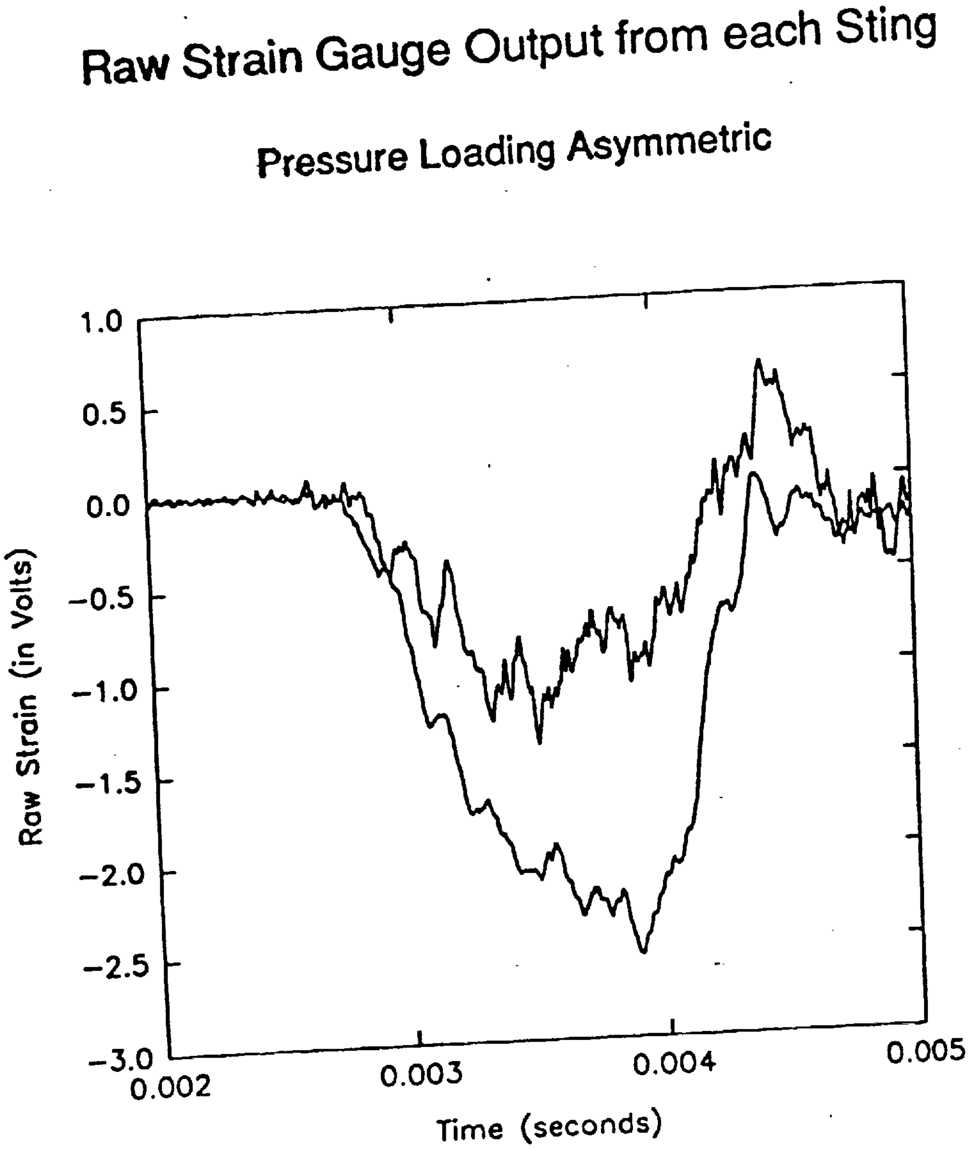
Raw Strain Gauge Output from each Sting

Pressure Loading Asymmetric

FIG 5.

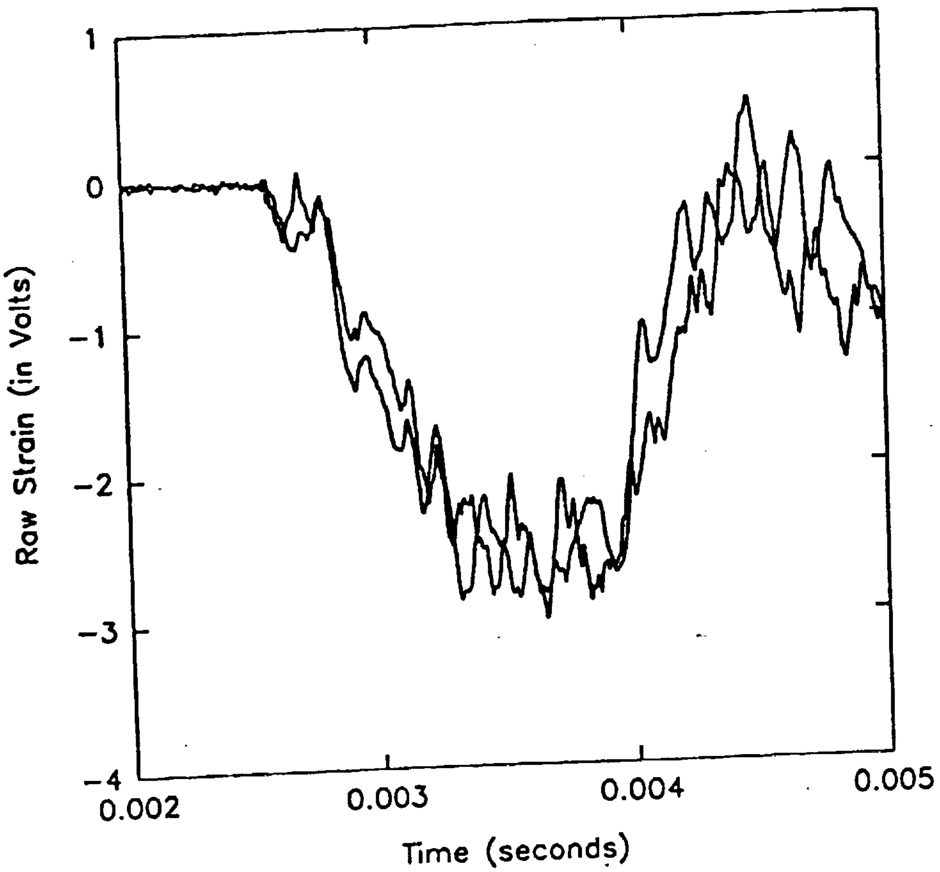
Raw Strain Gauge Output from each Sting

Pressure Loading nearly Symmetric

FIG. 6

Deconvolved Net Thrust & Pressure Thrust

with and without Fuel at 9 MJ/kg

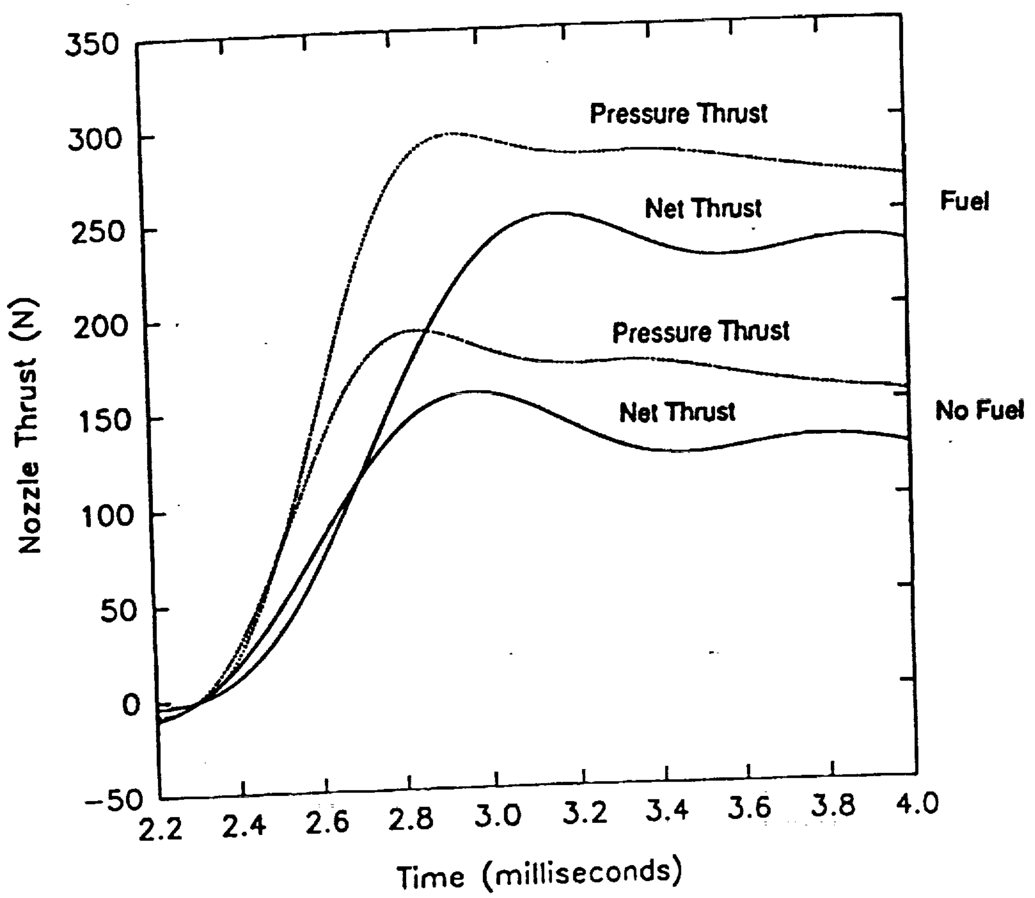

FIG. 7

N95- 25398

S4-25
45351

p. 4

SCALING IN A SCRAMJET COMBUSTOR

M.V. Pulsonetti and R.J. Stalker

1995118978

Studies of scramjet combustor scaling have been extended to include testing of a "small" combustor, thereby allowing comparison with results obtained in a "large" combustor of nearly identical configuration. As shown in the table and in Figure 1 the scale of the two combustors varied by a factor of 5.

It was anticipated that the combustion process would scale as the product of pressure with length if the temperature, the Mach number, the velocity, the free stream composition and the equivalence ratio were the same. To achieve this whilst allowing for the necessary difference in pressure the two models were tested with different shock tunnel nozzles. The large model was tested in a nominal M = 8 nozzle, with an intake consisting of a pair of opposing wedges preceding the model, which produced shocks to reduce the Mach number to approximately 3.4 before the flow entered the model inlet. It was then expanded to raise the Mach number again. The small model was tested in a nominal M = 4 nozzle, with the nozzle flow passing directly to the inlet of the model (i.e. "direct connect" mode).

The wedge intake for the large model was adjusted to yield similar combustion chamber Mach number for both models. Then, by matching the stagnation enthalpy, it was possible also to match the temperature and the velocity. The free stream composition was matched by operating at the same nozzle supply pressure. Since the nozzle throat, and the initial nozzle divergence angle were similar, the composition at which chemical "freezing" took place was approximately the same, and by ensuring that this was not changed by the shocks in the inlet of the large model, it was possible to arrange that the model flows experienced approximately the same free stream composition.

The two combustors were of constant area downstream of the injection strut. Thus the large combustor was of rectangular cross-section, 50 x 100 mm, and the small combustor was 10 x 20 mm. The injector strut spanned the large dimension of each duct, and was located in the mid plane of the duct. Unfortunately, manufacturing difficulties made it impossible to scale the thickness of the injector strut, and the large duct used an injector thickness of 10 mm, while the small duct injector strut was 3 mm thick. Since the flow expands to fill the duct cross-section as it passes the injector exit, this difference in relative injector thickness should not be significant.

Wall pressure distributions were measured along each of the ducts, and a comparison is shown in Figure 2. The pressure is normalised with respect to the pressure measured at a point opposite to the injector exit, and the distance downstream of the exit is normalised with respect to the height of the duct. It can be seen that, when normalised in this manner, both ducts produce quantitatively similar pressure distributions, confirming the initial hypothesis that the combustion process would scale as the product of pressure with length.

The flow conditions for the experiments are shown in the table. Using these conditions, the Reynolds' number, based on duct length, was 3.7×10^6 for both ducts. Therefore the mixing layer was turbulent.

When tests were done at lower stagnation enthapies the sudden pressure rise seen in previous tests (e.g. "Scaling and Ignition Effects in Scramjets" by M.V. Pulsonetti, Figure 2, Report on NASA Grant NAGW-674, Supplement 8, 1993) was in evidence in both the large and the small ducts. This also scaled approximately as the product of pressure with length. Further analysis of this data is under way.

H_{stag} = 7.4 MK/kg

	Large Scramjet	Small Scramjet
P	18.6 KPa	91.2 KPa
T	1500. K	1500. K
M	4.36	4.30
u	3400 m/s	3200 m/s
ϕ	1.36	1.27

Small Scramjet:
1/5 size of large scramjet

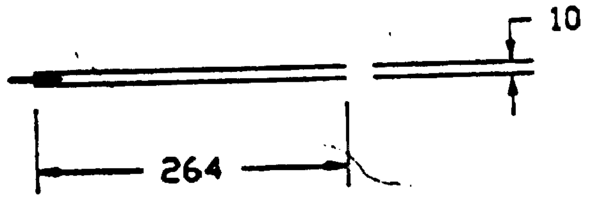

Large Scramjet:

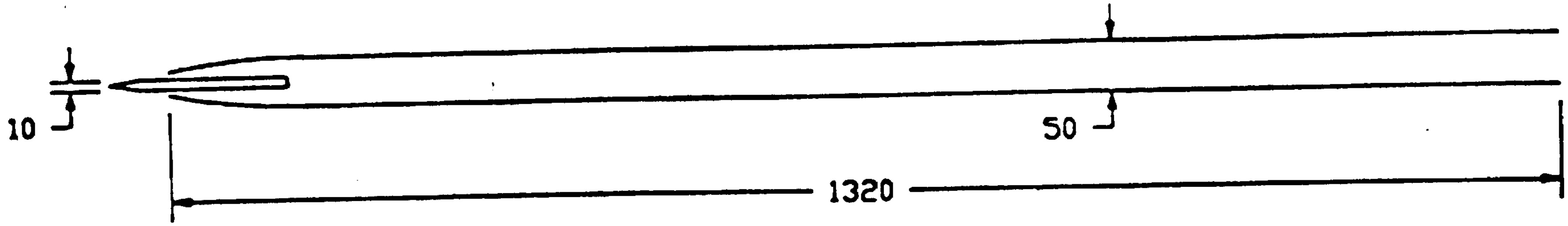

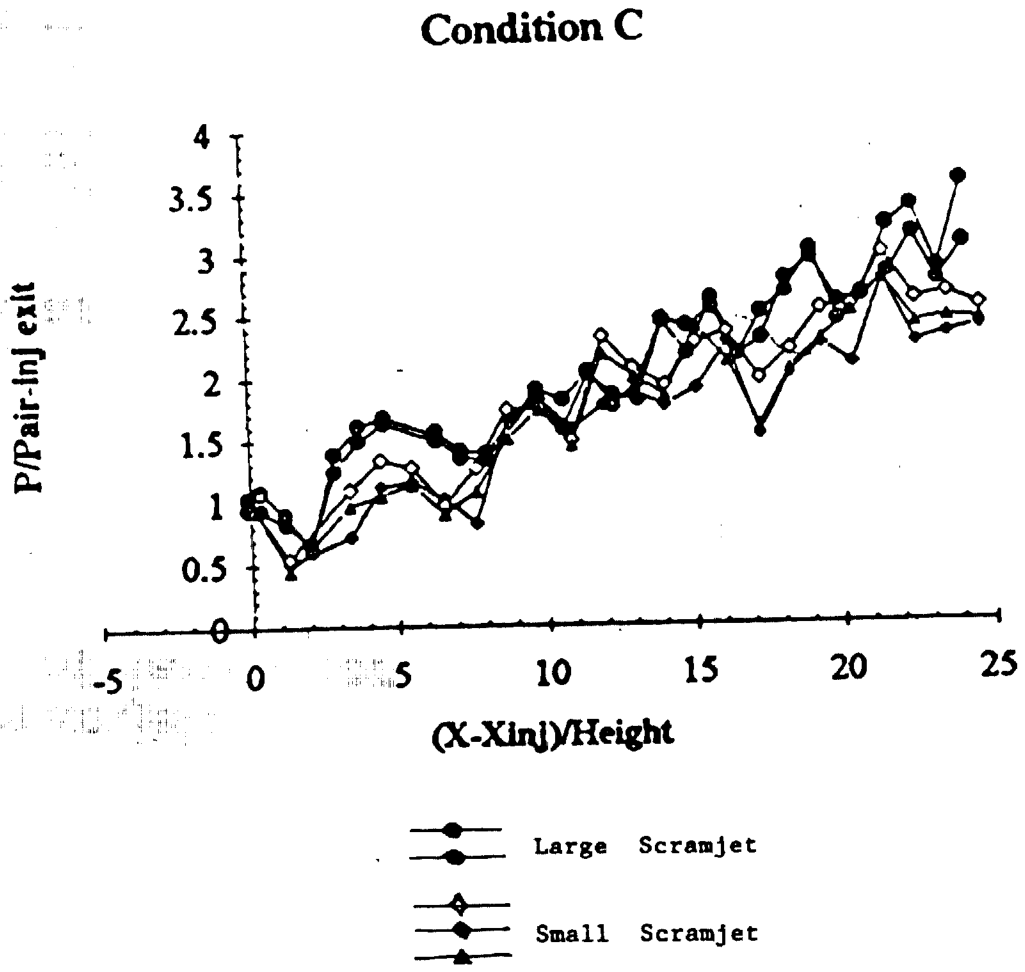
Condition C
P/Pair-Inj exit
4
3.5
3
2.5
2
1.5
1
0.5
0
-5
0
5
10
15
20
25
(X-Xinj)/Height
Large Scramjet
Small Scramjet

AIAA-93-2444

93A50196

HYPERSONIC IGNITION AND THRUST PRODUCTION IN A SCRAMJET

A. Paull

Mechanical Engineering Department
University of Queensland
St Lucia 4072 Australia.

Abstract

Experimental results are given for the specific impulse produced by a two-dimensional scramjet at flight speeds ranging between 2.5 and 5.5 km/s with a combustion chamber Mach number of 4.5. Both hydrogen and ethane fuels were used. Results show that provided sufficiently high pressures and sufficiently long combustion chambers are used specific impulses in excess of 1500 s can be obtained with hydrogen. Ethane produced specific impulses less than 600 s with the same conditions and model configuration.

Introduction

In the past ten years there has been renewed interest in air breathing engines for the purpose of hypersonic flight. One of the more promising engines is the scramjet. Many computational predictions of a scramjet's efficiency have been made (e.g. Kerrebrock (1992)), however, there is limited experimental data available which can be used to validate these predictions. One of the purposes of the experiments reported here was to obtain good experimental data which can be used to validate codes which predict the overall performance of a scramjet.

The overall performance of the scramjet is measured in terms of specific impulse. It is generally accepted that specific impulses in excess of 1000 s are required before scramjets can be a viable alternative to rocket propulsion. Experiments have been performed by Stalker and Morgan (1984) where the Mach number at the intake to the combustion chamber was nominally 3.7. They showed that the specific impulse peaks at a flight speed of 2.2 km/s and decreases rapidly to zero if the flight speed is less than 2.0 km/s and decreases monotonically with increasing flight speed and is zero at 4.0 km/s. Although the flight speed is a more relevant parameter to hypersonic flight, the temperature of the test gas is probably more relevant to the chemistry of combustion. In the experiments reported by Stalker and Morgan and the experiments reported here the flight speed is directly related to the test gas temperature. As the flight speed increases then so does the test gas temperature. (See table 1). The flight speed at which the specific impulse peaks in Stalker an Morgan's results has a test gas temperature of approximately 950 K. By using the global approximation proposed by Pergamont (1963) for the induction period of a hydrogen-oxygen reaction, it can be shown that the induction period becomes exponentially large for temperatures less than approximately 1000 K. Thus, as the combustion chamber duct length is finite there is insufficient time for the reaction to take place. Hence, the specific impulse drops to zero simply because the fuel has not burnt.

At higher temperatures the decrease in specific impulse does not primarily result from incomplete combustion due to insufficient combustor length, but is the result of a decrease in heat released. As the free stream temperature increases the percentage of water formed when the reaction reaches equilibrium, decreases. Therefore, there is less heat released at the higher temperatures. As a result, when the freestream temperature rises there is less energy available for thrust production and therefore the specific impulse decreases.

The scramjet is most efficient when the temperature at the intake to the combustor is the lowest which can produce combustion within the length of the combustor. This means that for reasonable size combustors the temperature at the intake must be maintained near 1000 K. Therefore, as the flight speed increases, if the peak efficiency is to be maintained, the Mach number at the entrance to the combustion chamber must increase.

The main aim of the experiments reported here was to determine the specific impulse as a function of flight speed (or temperature) at a Mach number greater than that used by Stalker and Morgan. A Mach number of nominally 4.5 was chosen.

Experiment Description

The experiments were undertaken in the free piston shock tunnel T4. Flight speeds range from 2.5 km/s to 5.5 km/s, the Mach number at the intake of the combustion chamber was nominally 4.5 and intake static pressure ranged from 30 kPa to 120 kPa. The tunnel was driven so that the static pressure and Mach number were steady through out the test time. The test time ranged from 1 to 2 ms depending on the test conditions. Flow properties at the intake to the combustion chamber were monitored by measuring the static and Pitot pressures. The remaining flow properties at the intake were determined numerically from the non-equilibrium codes NENZF (Lordi et.al.1966) and ESTC (McIntosh 1968). Table 1. displays the conditions at the intake to the combustion chamber for each experiment as predicted using theses codes. The test gas was air.

The scramjet consisted of a combustion chamber followed by a 11° divergent section as shown in figure 1. The scramjet combustion chamber had a rectangular cross section of dimensions 27 mm x 54.5

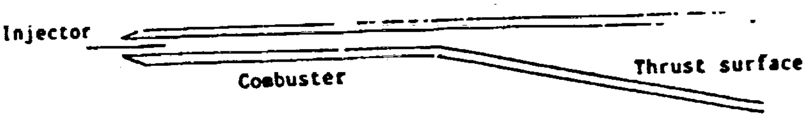

Figure 1. *Schematic of scramjet combustor and thrust surface.*

mm. The combustion chamber was 576 mm long. The fuel injector was 5mm thick and located in the centre of the duct as shown in figure 1. The exit plane of the injector was located 83 mm downstream of the leading edge of the combustion chamber and the fuel was always injected downstream through a supersonic nozzle. The leading edge of the injector was 73 mm upstream of the entrance to the combustion chamber.

Static pressure measurements were taken along the centreline of the wider wall. Measurements were taken at the exit plane of the injector, 30 mm and 10 mm upstream of the corner to the thrust surface and every 20 mm down the thrust surface. The transducers were mounted in mounts designed to suppress noise induced by vibration of the model. Measurements were taken from each transducer every 3 μs.

Experimental Analysis

The thrust or force produced in the upstream direction was determined from the wall pressure measurements made on the thrust surface. It was assumed that the pressure measured at each location was equal to the pressure over a rectangle with dimensions 20 mm x 54.5 mm centred on the point at which the measurement was made. The total forward thrust was obtained by summing the total force on the thrust surface as determined from the pressure measurements at any one time and determining the component of this force in the upstream direction (i.e. $\sin(11^{\circ})$ x total force).

The efficiency of the scramjet is measured in terms of the specific impulse. The specific impulse, ΔI, is defined as

$$\Delta I = \Delta T/\dot{m}/g \qquad (1)$$

where ΔT is the trust increment produced by the injection and burning of the fuel, $\dot{m}$ is the mass flow rate of the fuel and g=9.8 m/s^2.

The thrust increment is obtained by subtracting the thrust produced when fuel is injected (fuel-on) from the "thrust" produced when fuel is not injected (fuel-off). There is some variation in the conditions between the fuel-on and fuel-off runs. To take account of this variation in conditions the thrust is first normalized by the Pitot pressure and the difference between the normalized thrusts is obtained. To obtain the correct dimensionality this difference is then multiplied by the Pitot pressure from the fuel-off run. Thus,

$$\Delta T = \left(\frac{T_{on}}{P_{on}} - \frac{T_{off}}{P_{off}} \right) P_{off} \qquad (2)$$

The flow properties displayed in Table 1 are the flow properties of the fuel-off run. The flow properties of the fuel-on run were within 10% of the fuel-off properties.

The incremental specific impulse is an estimate of the specific impulse produced by a complete scramjet. That is, a scramjet which has an intake, in addition to a combustion chamber and thrust surface. This estimate is exact if there are no loses due to friction and the wave drag is reduced to zero. The incremental specific impulse is a good estimate if the frictional loses are small and the intake, combustion chamber and thrust surface are designed to minimize wave drag.

Experimental Results

Figure 2 displays a typical record of the static pressure during the duration of the flow. Fuel was injected at an equivalence ratio of one. This particular record is the pressure measured 20 mm downstream of the corner. The test time has been marked.

Figure 3 displays a typical distribution of pressure during the test time at the end of the combustion chamber and along the thrust surface when fuel is injected. The distance displayed on the x-axis is the wetted distance downstream of the combustor inlet. The beginning of the thrust surface occurs at 575 mm. It can be seen that there is a drop in pressure downstream of this point followed by a rise and a steady decrease to zero. The rise is also present in the fuel-off case, however, it is greatly reduced. The primary cause for this rise is the combustion of the fuel.

Figure 4 displays the thrust as a function of time for a typical fuel-on run. It can be seen that the thrust slowly rises then plateaus (to within 5%). The slow rise is reflecting the traversal of the shock down the thrust surface. The trust measurement is taken in the plateau region.

In the experiments presented the incremental specific impulse was determined as a function of flight speed for both hydrogen and ethane fuels.

Hydrogen Fuel Results

The hydrogen fuel was injected at mass flow rates which produced equivalence ratios of a half and one (stoichiometric). The specific impulse was

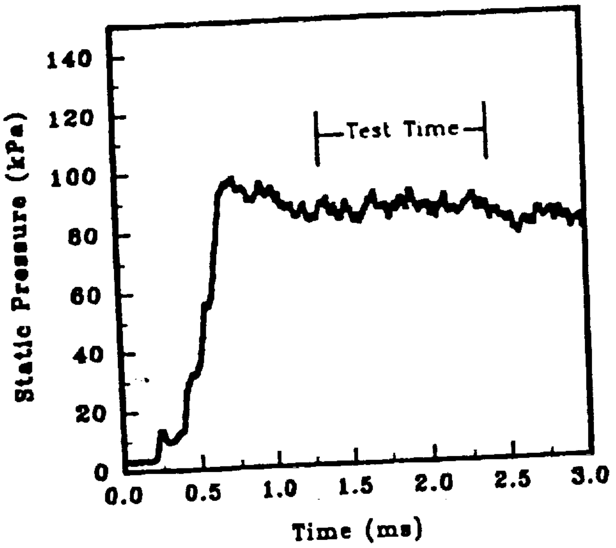

Figure 2. *Typical static pressure record.*

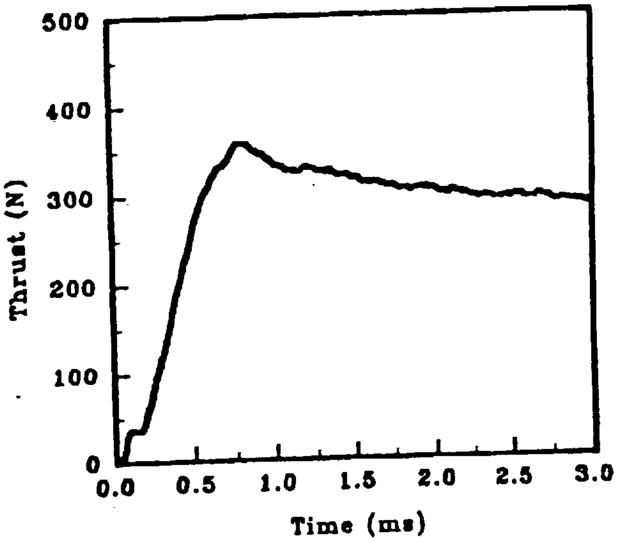

Figure 4. *Typical thrust record.*

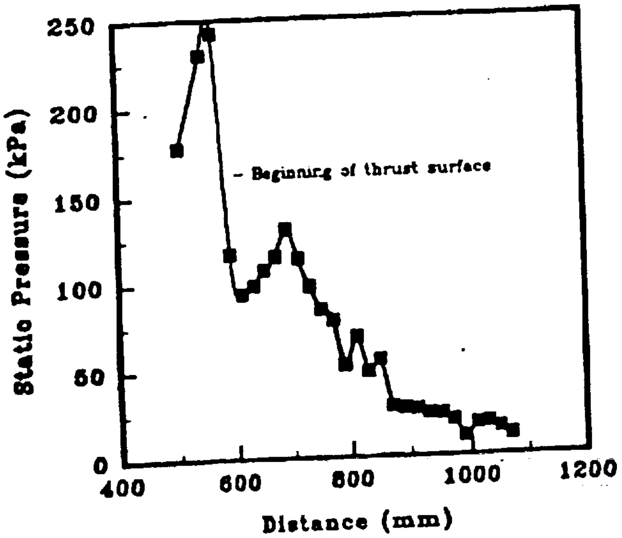

Figure 3. *Typical static pressure distribution at the end of the combustion chamber and along the thrust surface.*

obtained at each flight speed for two nominal intake pressures, 35 kPa and 100 kPa, although there was considerable variations in pressures for each nominal condition. (see Table 1). These two nominal conditions will be referred to as the low and high pressure conditions, respectively. Figure 5 displays the results of these experiments.

It can be seen from figure 5 that for an equivalence ratio of one and at the high pressure condition the general feature of the results are similar to those obtained by Stalker and Horgan, which are also displayed on figure 5. The major difference being that the peak specific impulse has decreased from 1800 s to 1600 s and, as is expected, the peak specific impulse is at a greater flight speed at the higher Mach number. The freestream temperature at the peak specific impulse at a Mach number of 4.5 is approximately 800 K, which is slightly lower than that recorded by Stalker and Horgan (950 K) for the lower Mach number condition.

These results are also qualitatively consistent with the calculations made by Kerrebrock (1992). There has been no attempt at this stage to quantitatively compare the predictions made by Kerrebrock with these experimental results.

At the low pressure condition it can be seen that at an equivalence ratio of one the sharp peak in the specific impulse which occurs at the higher pressure condition does not occur. In addition, the highest value of specific impulse is approximately half that at the higher pressure condition. This is believed to be the result of incomplete burning of the fuel. At the lower pressures there is insufficient length in the combustion chamber for either combustion or mixing of the fuel and air to occur.

At an equivalence ratio of a half the trends are similar to those observed at an equivalence ratio of one. However, it can be seen that the specific impulse produced at the lower equivalence ratio is generally higher. This is believed to be the result of a greater percentage of the fuel burning to form water. It is unclear at this stage if this is caused by better mixing or is a kinetic effect or both.

Ethane Fuel Results

Figure 5 also displays the specific impulse produced by ethane fuel when injected at the high pressure conditions. Ethane was injected through the same injector used for the hydrogen fueled experiments.

The fuel was injected at a mass flow rate which produce an equivalence ratio of a half. It can be seen that in this model a relatively small specific impulse is produced by the ethane. However, previous experiments presented by Paull (1992)

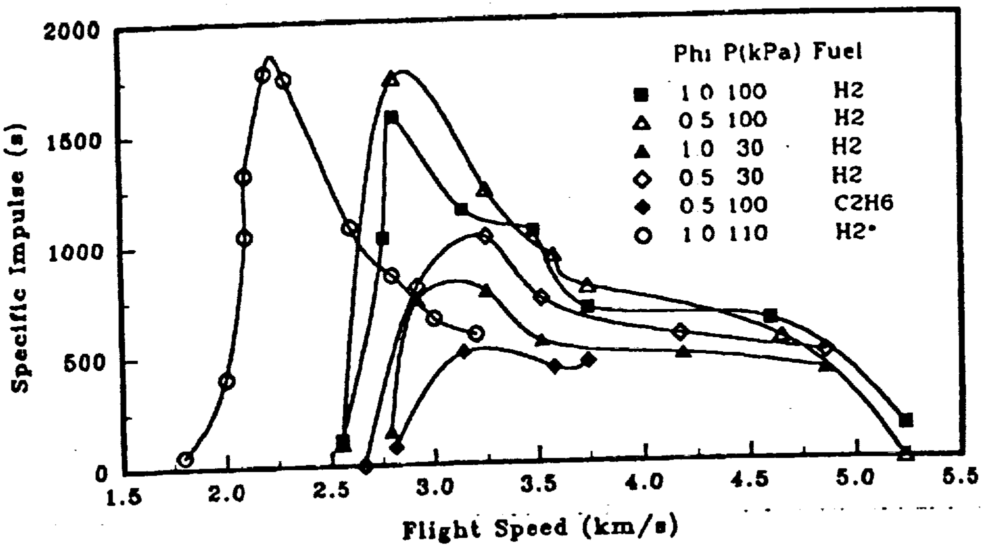

Figure 5. *Specific impulse as a function of flight speed at combustion chamber intake Mach number of 4.5.*
** Combustion chamber intake Mach number of 3.7.*

indicate that the length of a combustor required for ethane fuel is considerably longer than that for hydrogen. Hence, it is not surprising that a poor specific impulse was obtained using this model.

Conclusions

The change in specific impulse with flight speed at a combustion intake Mach number of 4.5 show similar trends to that observed at lower Mach numbers and are qualitatively similar to the trends predicted using kinetic theory for a hydrogen fuel.

Hydrogen fuel produces a greater specific impulse that ethane in the combustion chamber used in these experiments. This is the result of incomplete combustion of the ethane.

Acknowledgements

This work was funded jointly from the Australian Research Council and NASA Langley Research Centre. The author also wish to acknowledge the assistance of M.Giffin and L.Porter.

Notation

g	$9.8\ m/s^2$
H_s	Total Enthalpy
ΔI	Specific Impulse
M	Mach Number
$\dot{m}$	Mass Flow Rate
P	Static Pressure
P	Pitot Pressure
T	Thrust
T	Temperature
U	Gas velocity
V	Equivalent Flight Speed
ϕ	Equivalence Ratio
ϕ_1	H2 Equivalence Ratio which is nominally one
$\phi_{0.5}$	H2 Equivalence Ratio which is nominally a half

Subscripts

on	Fuel-on Properties
off	Fuel-off Properties

V km/s	Hs MJ/kg	T K	P kPa	ρ kg/m^3	M	U km/s	ϕ_1	$\phi_{0.5}$
				Low Pressure Runs				
2.8	3.9	700	35	0.189	4.5	2.4	0.9	0.42
2.9	4.3	870	30	0.11	4.4	2.6	1.0	0.41
3.3	5.3	1020	28	0.09	4.5	2.8	1.0	0.43
3.5	6.2	1230	30	0.09	4.4	3.0	1.0	0.55
4.2	8.8	1590	35	0.07	4.3	3.3	0.9	0.50
4.9	11.8	2370	39	0.05	4.3	3.8	1.0	0.49
				High Pressure Runs				
2.6	3.3	630	72	0.40	4.6	2.3	1.0	0.50
2.8	3.8	760	76	0.35	4.5	2.5	1.1	-
2.8	3.9	800	94	0.40	4.5	2.5	1.0	0.50
3.1	4.9	960	77	0.28	4.5	2.7	1.0	0.43
3.5	6.1	1270	87	0.24	4.4	3.0	0.9	0.50
3.7	7.4	1570	103	0.22	4.3	3.3	0.9	0.50
4.6	10.6	2530	121	0.16	4.2	3.7	1.0	0.45
5.2	13.7	3040	110	0.12	4.4	4.1	1.1	0.50

Table 1. *Free stream properties of the test gas at the entrance to the combustor when fuel was not injected. Hydrogen was used as fuel for both the high and low pressure conditions at $\phi=\phi_1$ and $\phi=\phi_{0.5}$. Ethane was used at the high pressure condition at $\phi=0.5$.*

References

Kerrebrock, J.L. 1992. Some readily quantifiable aspects of scramjet engine performance. Vol8 NO.5 pp 1116-1122 Sept-Oct. 1992 J. Prop. and Power.

Lordi, J.A., Mates, R.E. and Moselle, J.R. 1966. Computer program for numerical solution of nonequilibrium expansion of reacting gas mixtures. NASA CR-472.

McIntosh, M.K. 1968 Computer program for the numerical calculation of frozen and equilibrium conditions in shock tunnels. Dept. of Physics. ANU.

Paull, A. 1992 Hypersonic ignition in a scramjet. 11th Australasian Fluid Mechanics Conference.

Pergament, H.S. 1963. A theoretical analysis of nonequilibrium hydrogen-air reactions in flow systems. [Preprint] 63113. American Inst. of Aero. and Astro. April

Stalker, R.J. and Morgan, R.G., 1984. Supersonic hydrogen combustion and a short thrust nozzle. Combustion and Flame.

OMIT
to page
87

Supersonic Combustion in a Constant Area Duct.

by
Michael N. Wendt B.Eng. (Hons)

Submitted for Doctorate of Philosophy at the Department of Mechanical Engineering,
The University of Queensland.

February 1994

8.0 CONCLUSIONS

From a survey of the literature, little work was found on high enthalpy supersonic parallel central injection flows, downstream of the potential core. Of the work reported, most dealt with ignition or reaction limited flows. A detailed study was undertaken into the effect of fuel injection parameters on the mixing and combustion in a constant area duct with mixing limited high enthalpy flows. Transverse injection experiments were also performed for a comparison.

8.1 Displacement Thickness

The CFD parameter study showed that the wall pressure generated was mostly dependent on the stagnation temperature. This was because the temperature had a direct effect on the fuel velocity which was the most important parameter in generating turbulence. The mixing rate was virtually independent of the stagnation pressure of the fuel as it has little effect on the fuel velocity.

The displacement effect of the mixing layer on the pressure rise was studied. It was found that by reducing the area of the duct by the combined displacement thicknesses of the mixing layer and boundary layers, that the pressure could be predicted. The effect of heat addition was found to increase the displacement thickness by lowering the density of the mixing layer.

The effect of mass addition through boundary layer growth and mixing layer growth was found to be equally important to generating pressure as the heat addition from combustion. It was found that an incremental increase in displacement thickness produced a different amount of pressure rise depending on how close the total displacement thickness was to the height of the duct.

8.2 Temperature Effect

From examination of the literature, it was concluded that the effect of increasing the fuel stagnation temperature was its effect on the fuel velocity for mixing limited flow, and its effect on ignition for reaction limited flows.

From the results, only four runs had problems with ignition delay. These were all with cold injection. Heated injection at the same free stream conditions reduced the ignition delay by a least an order of magnitude. This was consistent with the observations from Neer and Drewery [1975] and Huber et al [1979].

Increasing the fuel stagnation temperature increased the velocity of the fuel stream. This decreased the velocity difference between the fuel and air streams which in turn reduced the mixing. This was consistent with the wall injection experiments of Hyde et al [1990]

The CFD results showed that the duct was very mixing controlled. The highest overall efficiency occurred with slow fuel injection, which increased the mixing efficiency and cold air conditions, which decreased the flame temperature and decreased the fraction of dissociated reaction products.

The velocity and density profiles showed that as the fuel stagnation temperature increased, the velocity gradient decreased and the mixing rate decreased. The decreased mixing decreased the displacement thickness and resulted in a lower pressure rise.

The different pressure rises between air conditions with the same amount of mixing was explained by examining the displacement thickness. The different mass flow rates of air for the different conditions resulted in different areas under the ρu profiles. For the same mixing layer width, this caused an increase in the displacement thickness with larger mass flow rates and a decrease in displacement thickness for lower flow rates.

In conclusion, the highest duct exit pressure was with low enthalpy air and low enthalpy fuel. This condition was close to the ignition point. Increasing the fuel temperature decreased the ignition length but also decreased the mixing rate.

8.3 Duct Height Effect

It was concluded that if we know the relationships for the displacement thickness of a mixing or combusting jet and for the boundary layers in a duct we can calculate the pressure in a duct of any height with the same jet by simply reducing the area of the duct by the total displacement thickness. If the growth rate of the mixing layer and boundary layers is small so as to not produce strong shocks, then the pressure can be calculated by one dimensional isentropic theory.

It was concluded the combined effect of mixing layer displacement thickness and boundary layer displacement thickness that causes the change in pressure between ducts of different sizes.

8.4 Equivalence Ratio Effect

The pressure results show that the rate of wall pressure rise grows linearly to an equivalence ratio of 0.65 and then changes slope. The rate of pressure rise then grows linearly from $\phi=0.65$ to $\phi=2.4$. The rate of increase of displacement thickness with equivalence ratio of the air+fuel experimental and CFD results after $\phi=0.65$ was the same as the nitrogen+fuel. This suggested that the further increase in wall pressure after $\phi=0.65$ was due to mass addition rather than heat addition. This was supported by the temperature of the duct exit which peaked at $\phi=0.75$.

Increasing the mass flow rate of fuel decreased the amplitude of the experimentally observed pressure fluctuations. This was consistent with the observations of Gilreath and Schetz [1971] and Sullins and Anderson [1982].

Increasing the mass flow rate of fuel caused an increase in ignition delay. This was consistent with the observations of Synder et al [1965] and Huber et al [1979]

The CFD mixing efficiency increased as mixture became more fuel rich or fuel lean. This was consistent with observations by Northam and Anderson[1986].

8.5 Comparison of Transverse Injection and Parallel Injection

Transverse injection experiments with cold and heated fuel injection showed little to no effect of fuel stagnation temperature on the duct exit pressure. The heated injection created a much greater disturbance to the oncoming flow resulting in large fluctuations in the measured wall pressure near the injector. This is consistent with the work of Charns and Collins [1970] who reported that the stagnation temperature had no effect on mixing but increased the radius of the bow shock formed by the jet.

When the waves were normalised by dividing by the nitrogen+fuel runs, the proportional pressure rise showed remarkable similarity between all fuel and free stream conditions. An ignition length of approximately 150mm was recorded for all conditions.

When the transverse injection was compared to parallel injection with the same fuel and air mass flow rates, similar pressure rises were found. This was consistent with the simple mixing theory of Northam and Anderson [1986].

The longer ignition times of the transverse injection with cold walls and cold fuel were consistent with the observations of Huber et al [1979].

6. SCRAMJET COMBUSTION SURVEYS

6.1 INTRODUCTION

For reasons outlined in Chapter 1, supersonic combustion of hydrogen has received new interest in recent years. As a result, the amount of research literature devoted to the feasibility, design, and performance of supersonic combustion engines has reached the level where entire books are dedicated to the review of current research. It is not feasible to go into detail on scramjet design here and the reader is referred to Murthy and Curran (1991) for a review of the topic. The purpose of this chapter, then is to present concentration measurements taken with the mass spectrometer across the fuel jet downstream of a parallel injector in hypersonic air.

Scramjets are essentially simple in geometry because the energy associated with hypersonic flow can burn through thin or intrusive elements of the engine. Because of the inherent simplicity of shape, scramjet combustors can be modeled for experimental studies at a reduced scale and well approximated by rectangular ducts (Stalker and Morgan, 1984). Extracting optimum performance from the engine relies upon maintaining control over the mixing, and stabilizing the combustion in a short region upstream of the thrust surfaces, (Stalker, 1991). The control of the mixing and combustion can principally be achieved through the means of fuel injection, making the study of jet mixing important for scramjet design.

6.1.1 Parallel Injection from a Strut

Four principle means of injecting fuel into the supersonic air flow have been proposed for scramjet engines:

1. Parallel injection from a strut or struts in the free-stream;
2. Parallel injection from a slot in the wall of the combustor chamber;
3. 'Vectored' injection from orifices flush mounted in the wall but inclined to the flow direction; and
4. Transverse injection from orifices in the wall of the combustor.

Of these methods, parallel injection from a strut is the simplest and the obvious starting point for a mass spectrometric analysis of supersonic combustion. This is because the model is two-dimensional and has the simplest geometry with no wall effects.

Parallel injection from a strut involves passing hydrogen through the downstream end of a long narrow injector aligned parallel to the air flow direction (Figure 6.1). The two coflowing streams then mix at a rate that is dependent on the velocities, densities, compressibility, initial turbulence of each gas stream, and the reaction rate of the mixing gases.

Ferri, Moretti and Slutsky (1965) first noted that if the temperatures were high enough, then as the fuel and air mix diffusively, the rate of reaction was controlled by the rate at which the diffusive mixing of the hydrogen and oxygen occurs. This is known as a 'diffusion controlled flame'. An alternate form of the diffusion controlled flame in supersonic flow occurs when the fuel mixes at lower temperatures and densities so that the ignition is delayed. In this case, after ignition, the diffusion of heat through the premixed gases controls the rate of heat release and the location of the reaction region.

The advantage of strut injection, as opposed to parallel wall injection, is that the fuel is introduced into the centre of the free-stream so that the fuel jet mixes on both sides and the flame front is kept away from the engine structure. Experiments have shown that where the flame front intersects a wall there is much increased local heat transfer, (Kanury, 1975). Experiments in shock tunnels have also shown that the combustion pressure rise from parallel wall injection is lower than parallel strut injection, (Stalker and Morgan, 1984). The major disadvantage of the strut in the free-stream is the heat transfer to the strut. Transverse injection from an orifice forms a complicated, three-dimensional flame structure which has a faster mixing rate but may cause too rapid a combustion at low hypersonic flight speeds.

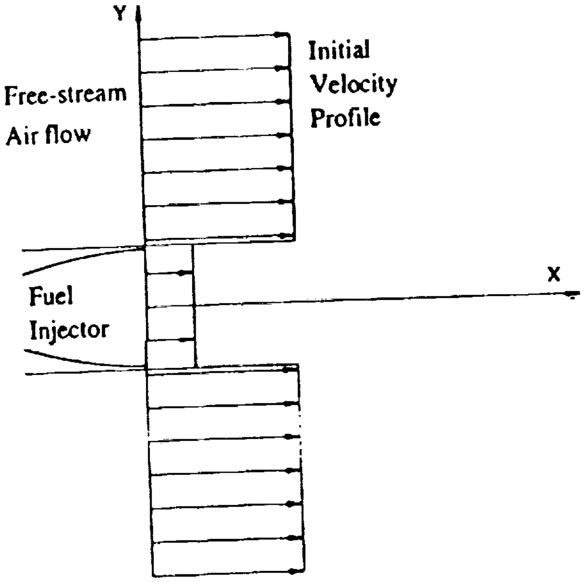

Figure 6.1 Parallel Fuel Injection in a Supersonic Flow

6.1.2 Theory of Supersonic Mixing and Combustion

Understanding of the physics of supersonic turbulent mixing has so far been mostly driven by empirical results. The equations of motion of compressible turbulent shear layers are so complex that, as yet, no analytical solution has been found. Numerical simulations are also currently unable to adequately predict the behaviour of the turbulence in highly compressible flows. Incompressible, constant density modeling of parallel injection has been successful at an analytical level by using simplified parabolic equations and simplified transport properties, (Schlichting, 1968; Weinstein, Osterle and Forstall, 1956).

The success of the incompressible solutions for velocity has led some researchers (Libby and Schetz, 1963; Cassacio, 1964; Zeiberg and Kaplan, 1965) to attempt to account for the change in density throughout the flow field by transforming the incompressible plane to the compressible plane using co-ordinate stretching techniques based on the local density. The success of this technique has been limited in hypersonic flows, even in the absence of chemical reactions, (Casey, 1991). Principally, the conclusion drawn from this lack of success is that the compressibility and the variation in transport properties are, in themselves, important to the production of turbulent mixing (Dimotakis, 1991). Brown and Roshko (1974) found that gas compressibility was a more critical influence on the growth rate of the mixing region thickness than the density ratio between the two streams. Currently, the knowledge of supersonic jet mixing relies upon empirical correlations and therefore further experimental research in previously unexplored flow regimes is a valuable aid to further understanding.

6.2 EXPERIMENTS AND RESULTS

In order to examine the amount of mixing and reaction of hydrogen injected into a hypersonic air stream, the mass spectrometer was used to measure the species concentrations at several transverse locations downstream of a hydrogen jet. For the same experimental conditions, at the same location, the pitot pressure was measured, to compare the momentum flux jet thickness with the concentration jet thickness. Generally, the peak definition of the spectra produced by the mass spectrometer for these experiments was superior to any of the previous experiments, although the higher densities sometimes caused arcing between electrodes.

6.2.1 The Experimental Test Flow Conditions

Four different nominal test conditions were used. That is to say that the initial shock tube conditions were identical for experiments at each condition, but there was a small spread in the final calculated test conditions. These experiments were performed with 5 mm diaphragms in the shock tunnel in order to produce sufficient levels of static pressure for combustion to occur. The specific enthalpies of the four conditions are listed in Table 6.1 along with the conditions in the test gas calculated using NENZF. These conditions were chosen because they covered the range of flight speed from 3.4 km/sec to 4.9 km/sec which might correspond to Mach 5.5 combustor flow (see Figure 1.2). Since the Mach number of the flow through the combustor was Mach 5.5, the static temperatures of the flow ranged from

1000 to 1700K, which was the expected range of optimum temperature in the combustion cycle. The densities chosen were the highest obtainable at which the mass spectrometer could be made to operate, given the problems encountered with the arcing and spreading of the peaks. These densities ranged around 0.05 kg/m^3.

The expected contamination levels of the test gas at these conditions were, based on measurements of Chapter four, less than 10 % by mole fraction. The exception was the highest enthalpy condition which was expected to have a contamination level of around 10 % by number. At the highest nominal enthalpy of 12.5 MJ/kg this may have reduced the effective specific enthalpy to around 11.5 MJ/kg, based upon the room temperature specific heats of helium, argon, and air. As the influence of the driver gas could not properly be incorporated into the calculation of the nozzle flow, the nominal conditions are used. As the mass of the helium is very small, the influence of the contamination on the energy balance in the flow was not large but the transport properties could be altered. It was possible that the reduction in temperatures and pressures caused by the loss in enthalpy could be off-set by an increased release of internal energy due to recombination in the nozzle flow. It was really only a concern at the highest nominal enthalpy condition.

The stagnation and static pressure of the test gas in flows produced by the shock tunnel varied with time, so that in the interval of 0.5 to 1 msec after the start of flow, the stagnation pressure generally fell slightly. The amount of this variation was kept to a minimum by the addition of argon to the driver gas (Jacobs 1993), but the pressure was still not exactly constant. The variation can be seen in Figure 6.2 which shows the stagnation and pitot

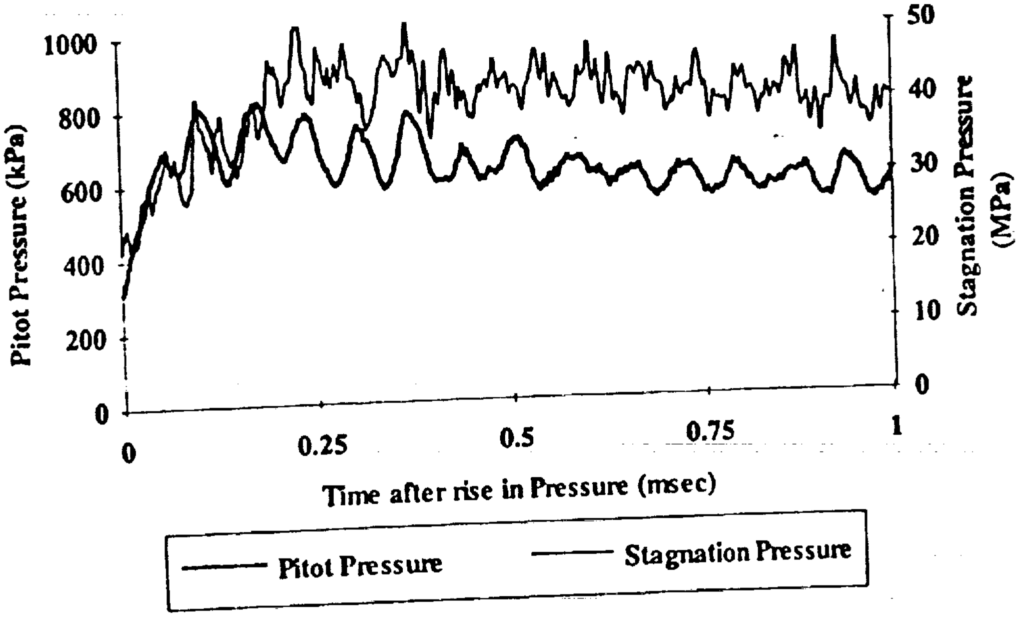

Figure 6.2 The Variation of the Pitot Pressure and Stagnation Pressure with Time for a sample run at Condition D (Run 114)
(The test time is defined from 0.5 to 1 msec and the stagnation pressure has been delayed by 0.19 msec to allow for flow starting)

pressure as a function of time from the start of flow to the end of the defined test region of flow. The variation in the stagnation pressure and the pitot pressure is included in Table 6.1, having been obtained from the change in the mean level of the flow as obtained from the line of best fit through the data for the test period. Generally the change in pressure level was less than 10%. The duration of the test period corresponded approximately to 3 passes through the model, so the variation during a single pass was negligible in this instance.

The NENZF calculations were obtained without taking into account the nozzle boundary layers or, for the highest enthalpy condition, the possible contamination of the test flow. According to the results of Chapter 5, this meant that the NENZF calculations probably overestimated the levels of atomic oxygen and underestimated the levels of nitric oxide. To examine the influence of the non-equilibrium chemistry, the nozzle flow calculations were also performed with equilibrium chemistry for each of the four test conditions. These calculations gave a static temperature and static pressure higher than were obtained in the non-equilibrium case where the dissociation absorbed some of the energy of the flow. Non-equilibrium calculations could not be performed for Condition D due to limitations in the chemical modeling in NENZF.

Table 6.1 The Experimental Test Flow Conditions

Measured Quantity	Condition A	Condition B	Condition C	Condition D
Driver gas composition	12%Ar88%He	17%Ar83%He	23%Ar77%He	25%Ar75%He
Shock tube fill pressure (kPa)	55	80	105	160
Total pressure (MPa)	40.3	39.9	39.7	40.3
Pitot pressure (kPa)	643	581	583	586
Static pressure (kPa)	19.6	16.7	12.9	11.1
Calculated Reservoir Conditions				
Enthalpy (MJ/kg)	12.2	9.4	7.8	5.6
Total temperature (K)	6880	5770	5110	4150
Non-Equilibrium Calculation				
Mach number	5.2	5.4	5.6	—
Temperature (K)	1750	1340	1050	—
Static pressure (kPa)	19.4	17.6	15.8	—
Density (kg/m^3)	0.037	0.045	0.052	—
Velocity (m/sec)	4260	3840	3550	—
Speed of sound (m/sec)	819	716	631	—
Ratio of specific heats	1.32	1.32	1.34	—
Pitot pressure (kPa)	625	615	605	—
Equilibrium Calculation				
Mach number	4.8	5.1	5.3	5.7
Temperature (K)	2278	1594	1266	761
Static pressure (kPa)	24	20.5	17.6	15.1
Density (kg/m^3)	0.036	0.045	0.05	0.069
Velocity (m/sec)	4358	3908	3610	3119
Speed of sound (m/sec)	908	766	681	547
Pitot pressure (kPa)	629	632	599	618

The measured pitot pressure and static pressure for each of the conditions are also given in the data. These two quantities represented the only experimental verification of the calculated conditions from the test section other than the use of the mass spectrometer. The measured pressures were lower than the calculated pressures although the fractional difference was within the combined errors in the two values.

6.2.2 The Experimental Model Configuration

The injector and duct geometry used in these experiments are shown in Figure 6.3. The model was designed by Buttsworth (1994). The duct internal measurements are 80 mm wide by 164 mm high. This meant that the maximum radial location of the nozzle exit flow entering the duct was 91 mm. The actual test core had a radial extent which had not properly been quantified but based upon the calculations used by the designers, had a radial extent of 72 mm, 83 mm downstream of the exit plane of the nozzle (Jacobs, 1993). The location of the nozzle exit plane with respect to the inlet of the duct was 40 mm upstream (i.e. 197 mm upstream of the injector exit). Some of the flow was therefore not part of the test core of the nozzle. The results of pitot pressure measurements in the exit plane, however, have shown that the velocity and density do not vary greatly outside the test core and that the model should not suffer extremely because of these variations.

The large size of duct was chosen to avoid complicating problems with boundary layers which have occurred in duct studies in the past (Casey, 1991). The large duct also provided as close a simulation of a free-jet as was possible. The width represented the largest injector which could reasonably be used to provide a uniform flow, and the height was chosen by Buttsworth (1994) to accommodate a shock producing wedge to study shock induced mixing and ignition in high energy air flows.

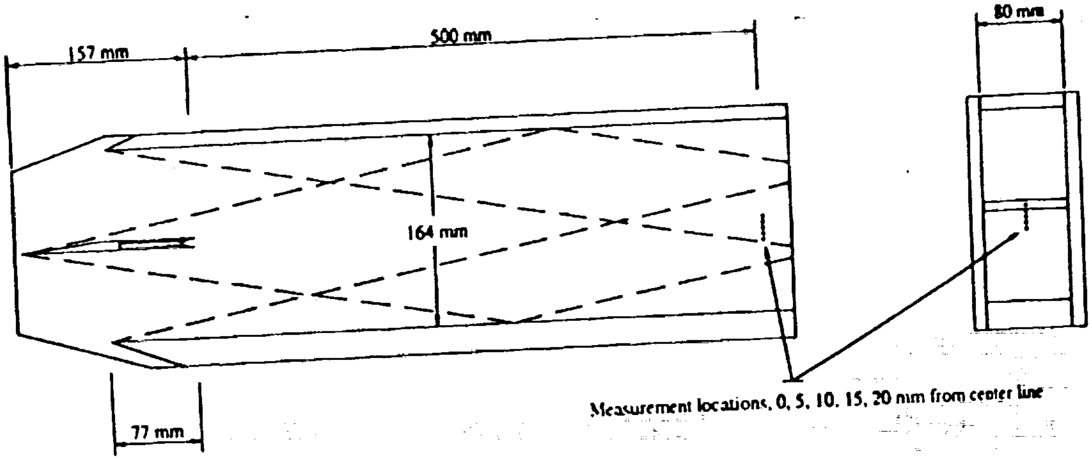

Figure 6.3 Diagram of the Scramjet
(The dotted lines show the trajectories of Mach waves from the leading edges in a Mach 5.5 flow)

As the ratio of the height of the duct to the duct width is 2:1, the duct cannot be said to be truly two-dimensional. To produce a two-dimensional free-jet in the shock tunnel test region was not a possibility however, and this configuration represented the best approximation. The jet may reasonably be considered as free in the transverse direction since the distance to the injector from the walls in this co-ordinate gave a line of influence traveling along a Mach line which intersected the centre of the duct at 370 mm downstream of the injector. This meant that the influence of the upper and lower walls would, at most, be a single weak compression wave from the boundary layer growth. Reducing the height of the duct would allow these waves to reflect across the duct several times in an equivalent distance. This was what, in fact, happened in experiments by Casey and he reported this as one of the major drawbacks of his experimental model.

The strongest wave present in the duct would have been the wave originating from the front of the injector on the inclined side to the flow. This wave would have been able to reach the centre of the duct after reflecting off the upper wall in the distance beyond which the concentration measurements were taken. The effect of the injector therefore, was minimised by having only a short length for the growth of the boundary layer, whilst also avoiding the problems of the bow shock interfering with the mixing of the free-jet injection. The only influence which the injector strut provided was the slight mismatch in pressure in the two streams because of the different strengths of the shocks on either side.

The injector strut, being 152 mm in length and 7.59 mm thick, is shown in Figure 6.4. For reasons to do with the experiments performed by Buttsworth, the injector strut was asymmetric, having an angle of 6.6 degrees on one side and 0 degrees on the other. The result of the asymmetry was to produce a slight mismatch in the static pressures on either side of the injector. This was calculated by Buttsworth as being of the order of 0.1% difference. The measurements were taken on the side of the injector which did not experience the bow shock off the 6.6 degree wedge.

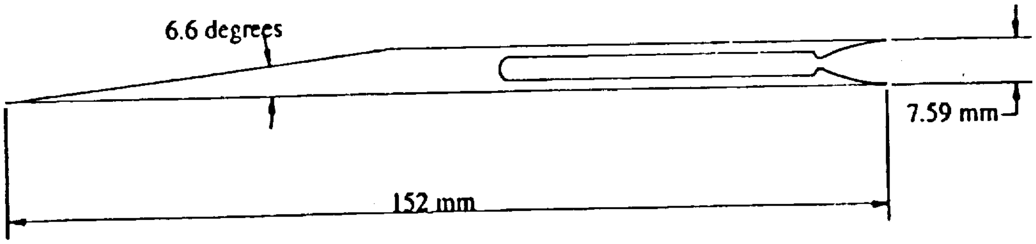

Figure 6.4 Diagram of the Hydrogen Injector

Hydrogen was supplied to the injector from a Ludwieg tube 25 metres in length with an internal diameter of 25.4 mm. The hydrogen was released from the Ludwieg tube by a high speed valve actuated from the injection pressure, (Stalker and Morgan, 1988). The opening time of the valve was about 1 msec. Measurements of the dynamic pressure between the valve and the injector showed that peak pressures were reached around 3 msec after the valve opened. The valve was opened 8 msec prior to the arrival of the test flow and was triggered off the recoil of the tunnel produced by the piston motion in the compression tube. At the time when the test flow occurred, the pressures measured by the dynamic pressure transducer had fallen by 8% from the peak values.

The hydrogen was expended through a contoured nozzle to a Mach number of about 3. The thickness of the throat was 1.74 mm and the height of the injector exit plane was 7.21 mm. The rear ends of the injector were each 0.19 mm thick.

The conditions in the hydrogen jet were obtained from calibrations performed by Buttsworth (1994). Buttsworth measured the pitot pressure at the exit plane of the injector and at the throat of the injector for a range of reservoir filling pressures and obtained empirical curves for the static pressure of the fuel jet as a function of the reservoir pressure. This empirical relation was required to account for pressure losses in the flow from the Ludwieg tube to the injector. The area ratio of the injector nozzle was 4.14, which determined the Mach number and assuming a total temperature of 296K, gave a static temperature and velocity which were independent of the injection pressure. The theoretical Mach number from the area ratio was 2.98 while the pitot pressure measurements gave a Mach number of 3.02. The conditions in the exit plane of the hydrogen injector are given in Table 6.2.

Table 6.2 The Conditions in the Hydrogen Fuel Jet

	Condition A	Condition B	Condition C	Condition D
Conditions in the Exit Plane				
Mach number	3.19	3.19	3.19	3.19
Temperature (K)	97.5	97.5	97.5	97.5
Static pressure (kPa)	10.4	9.9	7.84	6.46
Density (kg/m^3)	0.026	0.025	0.02	0.016
Velocity (m/sec)	2390	2390	2390	2390
Speed of sound (m/sec)	750	750	750	750
Pitot pressure (kPa)	136	130	102	85
Height (mm)	7.21	7.21	7.21	7.21
Conditions after Compression to Free-Stream Pressure				
Mach number	2.8	2.8	2.9	2.8
Temperature (K)	117	114	113	114
Static pressure (kPa)	19.6	16.7	12.9	11.1
Density (kg/m^3)	0.041	0.036	0.028	0.024
Velocity (m/sec)	2280	2300	2310	2300
Speed of sound (m/sec)	823	810	806	812
Pitot pressure (kPa)	195	175	137	115
Height (mm)	4.8	5.2	5.3	5.1

The injector pressures used were supposed to approximate the static pressure of the free-stream, but this was not achieved in practice. The free-stream static pressure was generally higher than the static pressure of the hydrogen jet at the exit of the injector. The physical result of this mismatch was an expansion of the free-stream gas and an associated compression of the hydrogen jet at the end of the injector. The effect of the pressure oscillations propagated away from the injector and in the current geometry, after the initial perturbation played no further influence on the mixing at sufficient distance downstream. The need to adjust the state of the hydrogen led to the assumption that the conditions in the hydrogen jet and the effective jet height could be found by assuming an isentropic compression from the exit conditions to the free-stream static pressure, and that the adjustment took place in a distance which was negligible compared with the distance to the measurements. The adjusted conditions after assuming isentropic compression to the free-stream pressure are also included in Table 6.2.

The profile of the injection wake was measured 500 mm downstream of the injector which represents 66 injector heights downstream of the injector exit. The transverse locations of the concentration measurements were 0, 5, 10, 15, and 20 mm as measured from the centre of the duct. The distance from the injector and the possibility that the flow was not parallel introduced the possibility that the centre of the velocity profile from the injector did not occur exactly at the location of the centre of the duct. This was examined by the pitot pressure measurements.

6.2.3 Measured Pitot Pressure Profiles

To compare the velocity profiles across the mixing region with the concentration profiles, and to obtain the value of the spreading coefficient, the pitot pressure was measured for each of the four experimental conditions. This was achieved using a rake of in-line transducers connected behind a stainless steel tubing of 2.65 mm external diameter and 2.04 mm internal diameter and spaced 5 mm apart. The rake is shown in cutaway in Figure 6.5. The transducers used for these measurements were PCB 112A piezoceramic type transducers, which are standard instrumentation for shock tunnels. The manufacturer's calibration was used for the sensitivities of the individual gauges but they were adjusted slightly by a relative calibration technique (Stacey, 1989). The same pressure (~ 75 kPa) was applied to all gauges simultaneously and the relative calibrations were adjusted until the measured pressure as a function of time co-incided. The average level of the measured pressure was not changed and the corrections to individual gauge's sensitivities were only a few percent at most.

Absolute calibrations were not obtained by this method as the error in the measurement of the calibration pressure was 15%. This error was the result of the absolute error in the Bourdon gauge used to fill the calibrator and the change in pressure caused by the expansion process in applying the calibration pressure. Additionally, as the measured levels in the experiment were in order of magnitude larger than could be obtained in the calibrator, the value of 75 kPa was not used to provide an absolute calibration.

The signals provided by the pitot pressure rake in the mixing region were quite noisy. Examples of the unfiltered pressure signals sampled at a rate of 1 MHz are shown in Figure 6.6. The time shown is from 0.5 to 1 msec after the start of flow. It is likely that the noise was not a representation of the turbulence of the flow, but instead the resonant oscillation of the cavity ahead of the transducer. The dimensions of the transducer cavity were 2 mm diameter with a total length of 27.5 mm length, of which the initial length was 21 mm. Using the calculated free-stream speed of sound of 600 to 800 m/sec, these dimensions gave resonant frequencies of 300 to 400 kHz, 22 to 29 kHz, or 28 to 38 kHz. The observed dominant frequencies were approximately 30 kHz, which corresponded to the lower predicted frequencies for longitudinal resonance. This was also supported by the observation that the pitot pressure in adjacent gauges followed each other for much of the test period. Were the oscillations of the order 30 kHz to represent genuine free-stream turbulence, then the scale of the turbulent structure would have to be in the order of a hundred millimetres - larger than the dimensions of the mixing region.

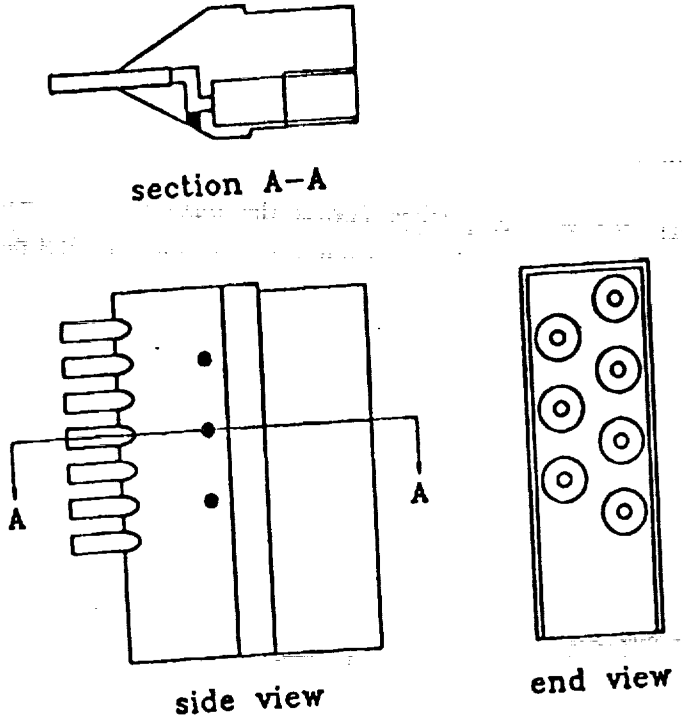

Figure 6.5 The Pitot Pressure Probe Rake
(From Buttsworth, 1994, Fig 4.14)

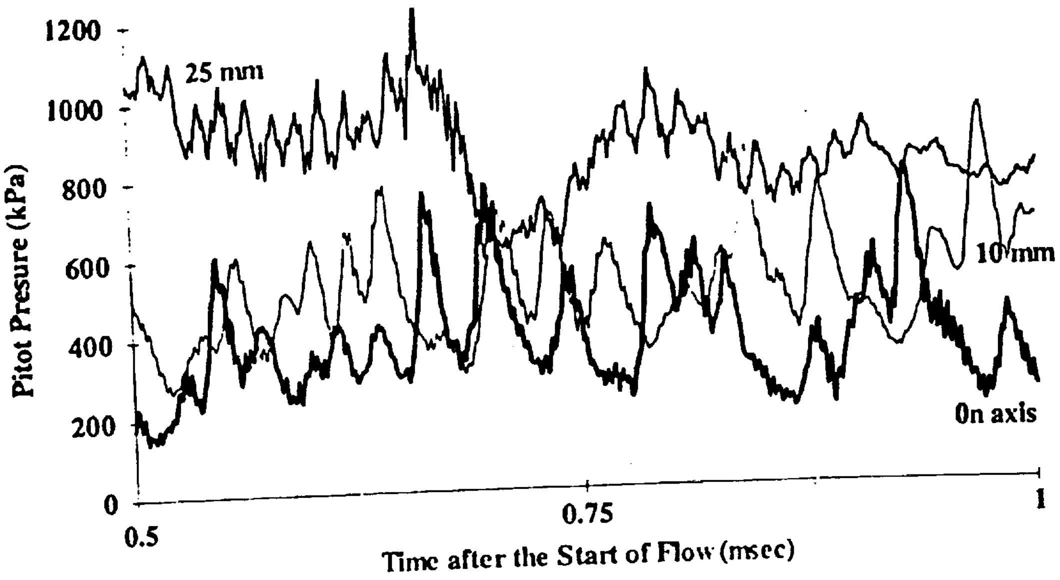

Figure 6.6 Sample Time Histories of the Pitot Pressure in the Mixing Region Flow for Run 148, Condition A
(Samples from locations 25 mm, 10 mm and 0 mm from the centre of the duct)

The measured values of pitot pressure are shown in Figures 6.7 to 6.10 for the four different test conditions listed in Table 6.1. The measured pitot pressure at the entrance of the duct is shown as a reference line, as is the calculated value of the free-stream pitot pressure provided by the non-equilibrium NENZF calculation. The predicted and measured values agree quite well but the pitot pressure at the edge of the jet shows a consistent rise to larger levels of pitot pressure than the expected free-stream values. This observation is consistent with previous measurements of pitot pressure in hypersonic ducts and indicates that the free-stream gas has undergone a compression. This compression may have resulted from the waves from the boundary layers on the walls and from the injector strut. Alternately, the compression in the free-stream rose from the entropy rise due to the mixing process and the subsequent growth in displacement thickness of the mixing region. The magnitude of the increase was greatest in the highest enthalpy case.

A further observation about the general shape of the profiles is that the measured values of pitot pressure at ±5 mm are not equal in three out of the four cases. The implication is that the axis of symmetry of the pitot pressure profile had been shifted slightly (≈2 mm) into a positive location in the duct. This corresponds to a shift towards the side of the injector without the 6.6° wedge, which is away from the side of the injector that has experienced a stronger shock and therefore should have a slightly larger static pressure.

The displayed error in the measurements represents the variation in the mean value of pitot pressure during the defined test period. As the pressure fell slightly during the test time, the mean value of the pressure was determined by finding the line of best fit through the data using least squares regression. The standard deviation of the pitot pressure signals was much larger than this variation in the mean level. As discussed earlier, this large spread was not representative of the free-stream variation and therefore did not indicate that the error in the mean value was large, only that the oscillation of the pressure in the gauge cavity was quite large.

Table 6.3 Measured Values of Pitot Pressure across Duct at 500 mm Downstream from the Injector

	Condition A	Condition B	Condition C	Condition D
Inlet	601	633	623	571
NENZF	625	615	605	618
Location (mm)				
-5	351 ± 56	480 ± 44	388 ± 29	357 ± 14
0	307 ± 30	431 ± 21	354 ± 13	345 ± 04
5	323 ± 39	433 ± 78	382 ± 22	408 ± 21
10	408 ± 61	481 ± 09	412 ± 33	505 ± 13
15	607 ± 52	602 ± 40	519 ± 46	607 ± 30
20	719 ± 75	654 ± 16	617 ± 69	624 ± 03
25	688 ± 84	668 ± 33	—	—

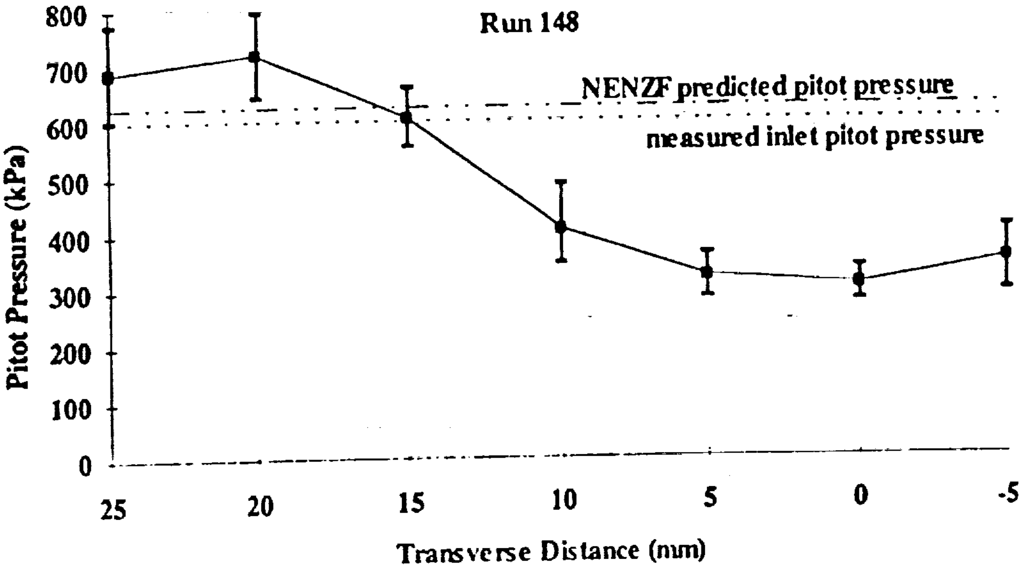

Figure 6.7 Pitot Pressure Profile across the Mixing Region for Test Condition A. (Air Enthalpy 12.2 MJ/kg)

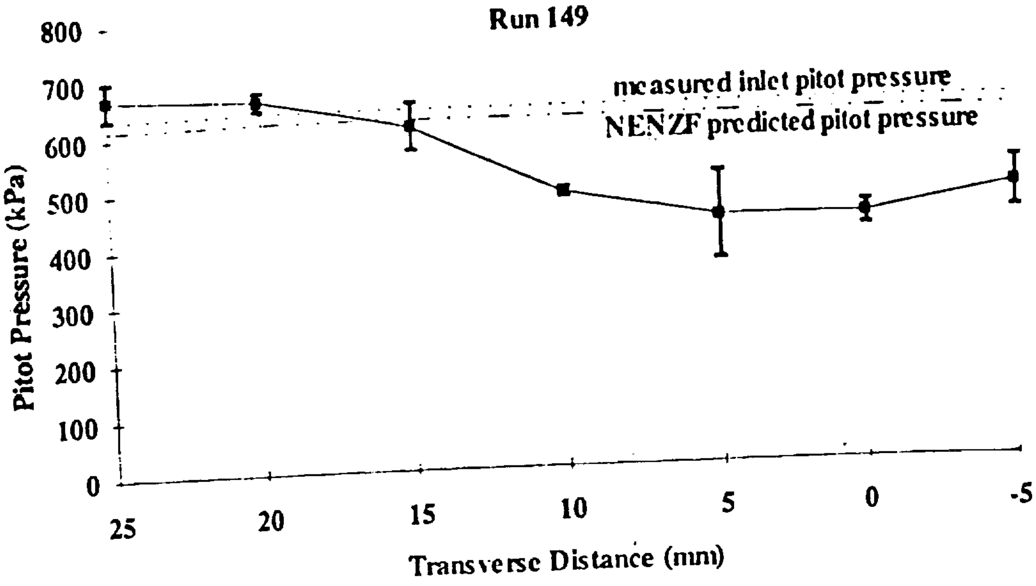

Figure 6.8 Pitot Pressure Profile across the Mixing Region for Test Condition B. (Air Enthalpy 9.4 MJ/kg)

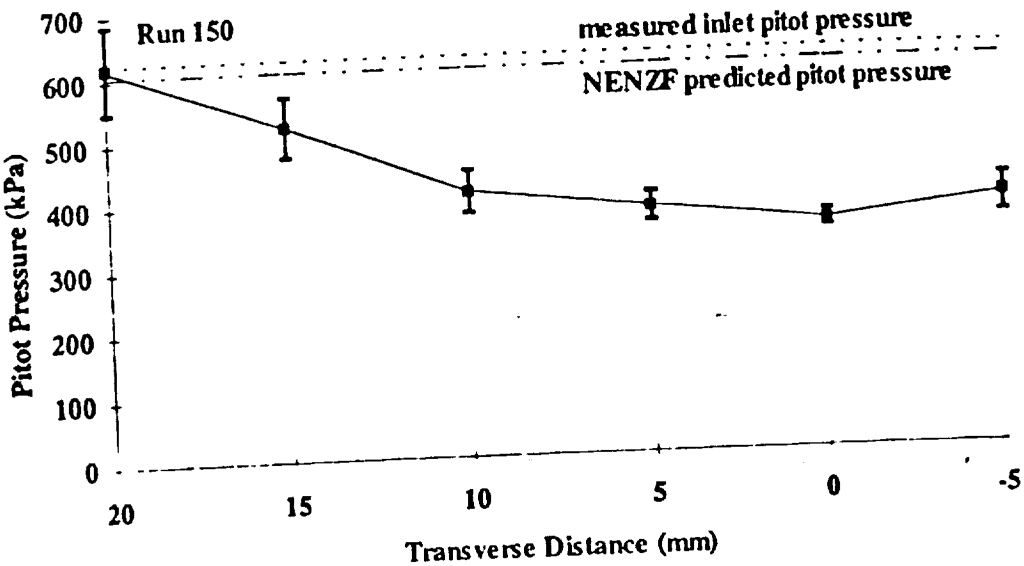

Figure 6.9 Pitot Pressure Profile across the Mixing Region for Test Condition C. (Air Enthalpy 7.8 MJ/kg)

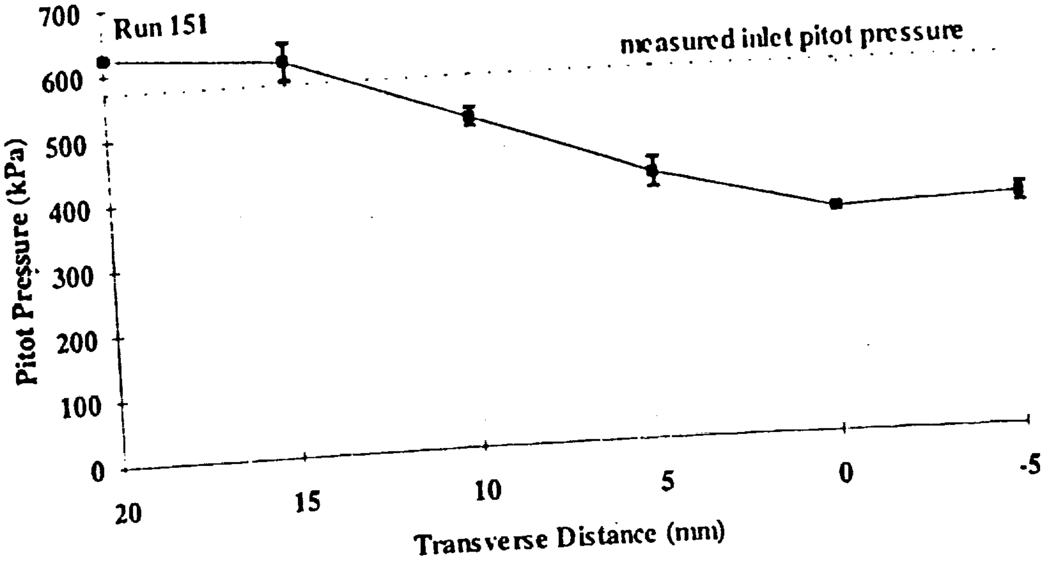

Figure 6.10 Pitot Pressure Profile across the Mixing Region for Test Condition D. (Air Enthalpy 5.6 MJ/kg)

'36

6.2.4 Measured Concentration Profiles

The concentrations at the measurement stations across the hydrogen jet were found by the mass spectrometer in Runs 110 to 141. Because only the concentrations during the test time were of interest the resolution of the data recorder was increased to allow more samples to be taken within the limits of each peak, thereby reducing the error encountered earlier with the thin peaks such as the helium. The duration of the data recording was only 2.5 msec at the higher resolution but the test time was defined as being from 0.5 to 1 msec in any case. The quality of the spectra was generally very good with most spectra showing complete separation of the nitrogen, nitric oxide and oxygen peaks. Some spectra produced hydrogen peaks which were large enough to saturate out the particle detector signal in the early stages of the flow when the density was greatest. For these runs and in the few cases where arcing occurred, the test time was sometimes reduced or moved back past the 1 msec cutoff. The runs used for the measurements are listed in Table 6.4, which shows the experimental conditions, test times used and the concentrations measured for these experiments.

Before presenting the analysis of the mass spectrometer measurements, a word of caution must be given. The conditions in the mixing region behind the injector were strictly not identical to the conditions in the free-stream where the mass separation calibrations occurred (see Section 3.7). Principally, the pitot pressure and the Mach number of the gas entering the first skimmer were lower than in the free-stream. Also, the wake region experienced a gradient of conditions across the orifice at the front of the first skimmer. The front orifice through which the sample was drawn was 2 mm in diameter which, from the pitot pressure profiles, could have experienced a difference in pitot pressure across it of up to 80 kPa or 16%. This has been assumed to be negligible with regard to the effect on mass separation and the freezing of the flow inside the skimmer. (In regions closer to the fuel injector, where the difference in flow properties can become very large in a transverse distance of 2 mm, the use of the mass spectrometer sampling system would need serious attention to be justified. The problem could be reduced by decreasing the size of the front skimmer).

Of the species of interest, the mass spectrometer was only calibrated for the relative concentrations of hydrogen, argon, and helium with respect to nitrogen. The lack of comprehensive calibration data meant that assumptions had to be made about the behaviour of the mass spectrometer before quantitative estimates could be made of the relative number density. For molecules of similar mass and structure to nitrogen, the calibration factors were assumed to be 1. This assumption was adopted in Chapter 5 and gave reasonable results. This meant that the nitric oxide and oxygen were assumed to behave in the same way as nitrogen molecules throughout the processing by the mass spectrometer.

The remaining species of interest consisted of water, the hydroxyl radical, and the free atomic hydrogen, oxygen, and nitrogen (H_2O, O, N, OH, or H). The assumption was made that there was no free atomic species or hydroxyl present in the flow. The calculated levels of free-stream atomic nitrogen using NENZF were zero in all conditions. The calculated levels of free-stream atomic oxygen were small in all except for Condition A. This is supported by the results of Chapter 5 which showed little variation in the size of the atomic peaks relative to the molecular peaks as the enthalpy increased to 10 MJ/kg, and showed inconsistent variation at higher enthalpies. Also, theoretical estimates of the combustion reaction rates predicted that the reaction time was of the order of 10 μsec (Stalker and Morgan, 1982), implying that the residence time of reactive species was small. Finally, the experimentally measured areas of the peaks produced by the atomic species and the hydroxyl radical were not large compared with the signal from diatomic species, so, excepting an extreme artificial depletion of these species relative to other species, it was unlikely that there was a large contribution to the number density from the dissociated species. While not discounting the presence of such species, their presence should not alter the mole fractions of the stable species significantly, certainly not beyond the error already present in these measurements.

A last assumption must now be made to provide a calibration factor for the measurement of the water molecule. For reasons of simplicity as much as anything else, this was taken to be 1. The actual calibration constant is not likely to be far from 1 as the calibration constant for helium (the largest measured) is only 1.7 at these pitot pressures and the calibration constant for hydrogen is 1 also. As the helium and argon are monatomic and the mass ratios for these species are more severe that the mass ratio of water to nitrogen, the error in the estimate of 1 for the relative calibration of water is assumed to be 25%, which is to say that the calibration might be as much as 1.25 or as low as 0.75. With this final assumption the mole fractions of the seven species can be calculated from the individual relative concentrations to nitrogen.

The fractions for the seven species were calculated from the areas under the peaks in the recorded spectra and used the following formulas:

$$\frac{[H_2]}{[N_2]} = 1 \times \frac{1.68}{0.557} \frac{\text{Area } H_2}{\text{Area } N_2} \tag{6.1}$$

$$\frac{[O_2]}{[N_2]} = 1 \times \frac{1.68}{1.57} \frac{\text{Area } O_2}{\text{Area } N_2} \tag{6.2}$$

$$\frac{[NO]}{[N_2]} = 1 \times \frac{1.68}{1.89} \frac{\text{Area NO}}{\text{Area } N_2} \tag{6.3}$$

$$\frac{[H_2O]}{[N_2]} = 1 \times \frac{1.68}{1.31} \frac{\text{Area } H_2O}{\text{Area } N_2} \tag{6.4}$$

$$\frac{\text{Driver}}{[N_2]} = 1.7 \times \frac{1.68}{0.313} \frac{\text{Area He}}{\text{Area } N_2} + 1.25 \times \frac{1.68}{1.87} \frac{\text{Area Ar}}{\text{Area } N_2} \tag{6.5}$$

Here the absolute mole fractions are obtained by dividing the relative mole fractions by the sum of the relative mole fractions of each species. The mole fractions for a sample of the runs as a function of time are presented in Figures 6.11 to 6.13. In these figures the traces are divided into hydrogen and water in part (a), the components of air in part (b) and the driver gas contamination level of the sample in part (c). It can be seen that the traces show a variation with time but that the concentrations are reasonably constant with time in the interval from 0.5 to 1 msec after the start of the flow.

Concentration profiles across the mixing region have been obtained from the measurements from the individual runs. These are shown in Figure 6.14 to 6.17 for the test conditions A to D. The error bars represent standard errors of the mean of the measurements from all spectra for each run and do not include systematic errors from the assumptions regarding the calibrations. The data presented in these figures is included in Table 6.5 The same results expressed as mass fractions are given in Figure 6.18 to 6.21. In Figure 6.22 the average molecular weight of the gas sample is plotted as a function of transverse distance.

Table 6.4 The Conditions for the Test Runs for the Measurements of Species Concentration

Run	Test Condition	Location (mm from axis)	Comment	Measured Total Pressure (MPa)	Measured Pitot Pressure (kPa)	Enthalpy (MJ/kg)	Total Temp. (K)	Pressure (kPa)	Density (kg/m^3)	Velocity (m/s)	Temp. (K)
109	B	0	arcing	39.3	577	9.3	5739	17.5	0.045	3827	1325
110	D	0	H_2 sat.	42.2	618	6.1	4368	16.6	0.068	3228	644
111	C	0	H_2 sat.	36.5	584	7.5	4964	14.4	0.051	3485	998
112	B	5	good	37.2	520	9.0	5582	16.3	0.044	3766	1263
113	C	5	good	38.3	538	7.5	4991	15.2	0.053	3495	998
114	D	5		39.3	577	5.5	4081	14.6	0.069	3086	738
116	B	10	good	40.6	592	9.8	5950	18.5	0.045	3910	1408
117	C	10		39.0	616	7.7	5056	15.3	0.051	3533	1033
118	A	10	v good	40.3	686	12.6	7047	19.5	0.035	4327	1805
119	D	10		40.8	579	5.4	4041	15.0	0.073	3064	722
120	B	15	small	38.3	582	9.1	5653	16.9	0.045	3794	1291
131	B	20		41.8	—	9.7	5913	19.0	0.047	3893	1394
135	C	20		39.8	—	—	—	—	—	—	—
136	D	20		39.8	—	5.6	4105	14.9	0.07	3097	745
137	A	20		39.8	—	11.9	6796	19.0	0.037	4230	1717
138	A	15		39.8	—	12.0	6815	19.0	0.037	4238	1721
139	C	15		41.4	—	8.0	5196	16.6	0.053	3595	1089
140	A	5		39.6	—	11.7	6702	18.9	0.038	4175	1683
141	A	0		40.9	—	12.1	6869	—	—	—	—

Table 6.5 Measured Mole Fractions

Condition	Location	H_2	H_2O	N_2	NO	O_2	Driver	# of Data Points	Start Time (msec)	End Time (msec)
A	0	0.63 ± 0.04	0.09 ± 0.00	0.20 ±0.00	0.02 ± 0.00	0.02 ± 0.00	0.05 ± 0.02	7	0.69	1.02
	5	0.69 ± 0.05	0.06 ± 0.01	0.18 ± 0.01	0.03 ± 0.00	0.03 ± 0.00	0.00 ± 0.01	8	0.66	1.03
	10	0.56 ± 0.05	0.12 ± 0.01	0.22 ± 0.01	0.03 ± 0.00	0.02 ± 0.00	0.05 ± 0.01	10	0.52	1.00
	15	0.50 ± 0.03	0.12 ± 0.02	0.28 ± 0.01	0.01 ± 0.00	0.04 ± 0.01	0.04 ± 0.02	4	0.86	1.02
	20	0.08 ± 0.05	0.07 ± 0.01	0.48 ± 0.01	0.06 ± 0.01	0.12 ± 0.00	0.20 ± 0.01	6	1.21	1.48
B	0	0.68 ± 0.18	0.18 ±0.02	0.17 ± 0.03	0.03 ± 0.01	0.05 ± 0.02	0.05 ± 0.01	3	1.17	1.76
	5	0.66 ± 0.04	0.04 ± 0.05	0.22 ± 0.01	0.02 ± 0.00	0.05 ± 0.00	0.01 ± 0.00	6	0.71	0.97
	10	0.51 ± 0.05	0.05 ± 0.03	0.30 ± 0.01	0.06 ± 0.00	0.08 ± 0.00	0.03 ± 0.01	10	0.51	0.99
	15	0.35 ± 0.05	0.05 ± 0.02	0.34 ± 0.01	0.09 ± 0.01	0.16 ±0.01	0.04 ± 0.01	10	0.50	0.98
	20	0.13 ± 0.04	0.04 ± 0.06	0.46 ± 0.01	0.06 ± 0.00	0.15 ± 0.01	0.14 ± 0.01	6	1.03	1.31
C	0	0.64 ± 0.05	0.04 ± 0.00	0.23 ± 0.01	0.02 ± 0.00	0.06 ± 0.00	0.01 ± 0.00	10	0.53	1.01
	5	0.47 ± 0.05	0.03 ± 0.00	0.35 ± 0.01	0.05 ± 0.00	0.10 ± 0.00	0.00 ± 0.00	10	0.51	1.00
	10	0.34 ± 0.05	0.02 ± 0.00	0.44 ± 0.01	0.07 ± 0.00	0.13 ± 0.00	0.01 ± 0.01	10	0.53	1.01
	15	0.24 ± 0.03	0.04 ± 0.00	0.47 ± 0.02	0.04 ± 0.01	0.15 ± 0.01	0.06 ± 0.01	4	0.92	1.08
	20	0.06 ± 0.03	0.05 ± 0.00	0.60 ± 0.03	0.03 ± 0.01	0.16 ± 0.02	0.11 ± 0.02	4	1.40	1.56
D	0	0.68 ± 0.04	0.04 ±0.01	0.21 ± 0.00	0.03 ± 0.00	0.06 ± 0.00	0.01 ± 0.00	6	0.98	1.25
	5	0.40 ± 0.05	0.05 ± 0.02	0.39 ± 0.01	0.05 ± 0.00	0.15 ± 0.00	0.00 ± 0.01	10	0.49	0.97
	10	0.24 ± 0.05	0.05 ± 0.02	0.49 ± 0.01	0.05 ± 0.01	0.22 ± 0.01	0.00 ± 0.00	10	0.49	0.97
	20	0.02 ± 0.04	0.04 ± 0.02	0.70 ±0.01	0.04 ± 0.02	0.19 ± 0.01	0.03 ± 0.01	5	1.51	1.73

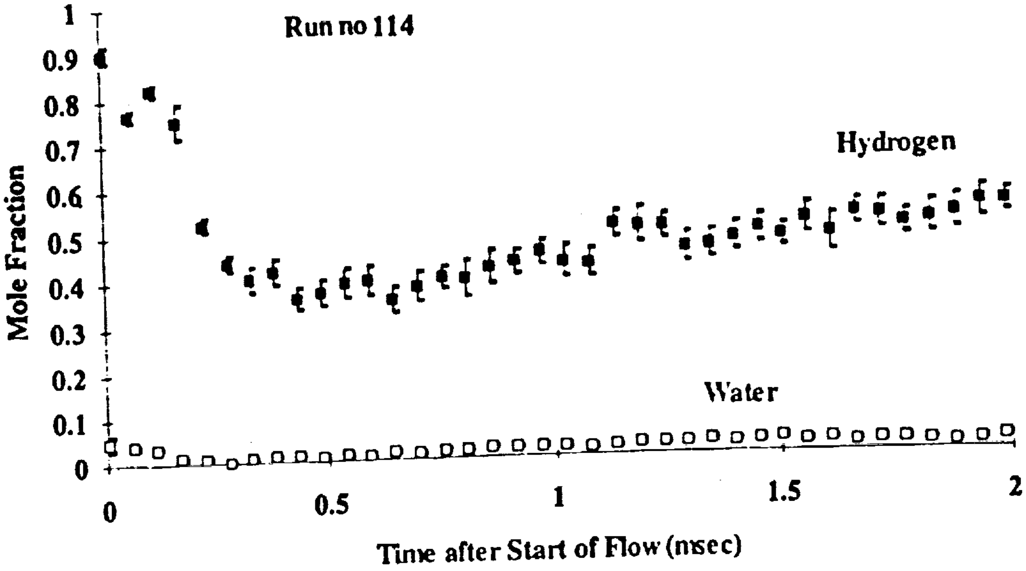

Figure 6.11 (a) The Mole Fraction of Hydrogen and Water as a Function of Time (Condition D and 5 mm off Axis)

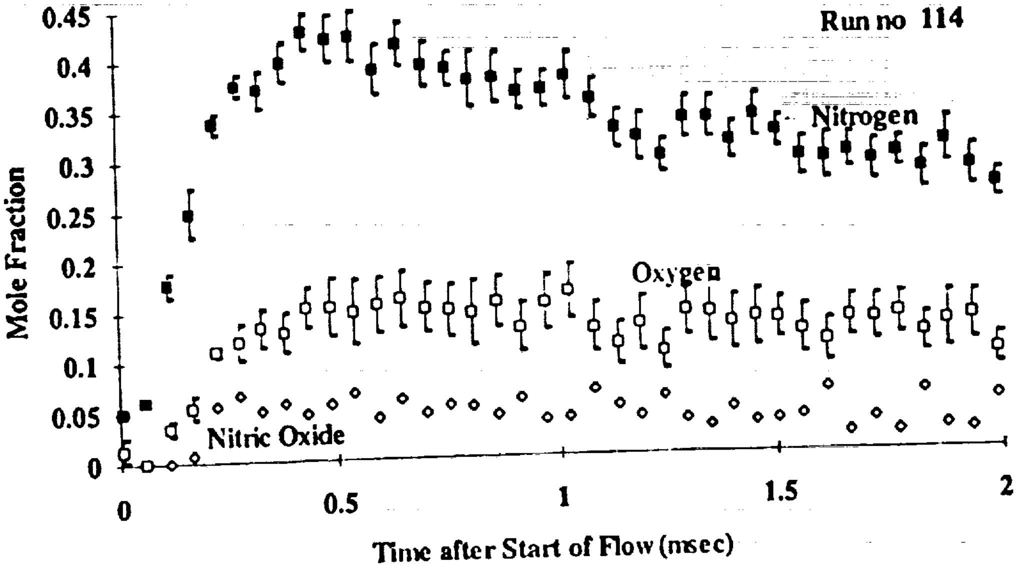

Figure 6.11 (b) The Mole Fraction of Nitrogen Oxygen and Nitric Oxide as a Function of Time (Condition D and 5 mm off axis)

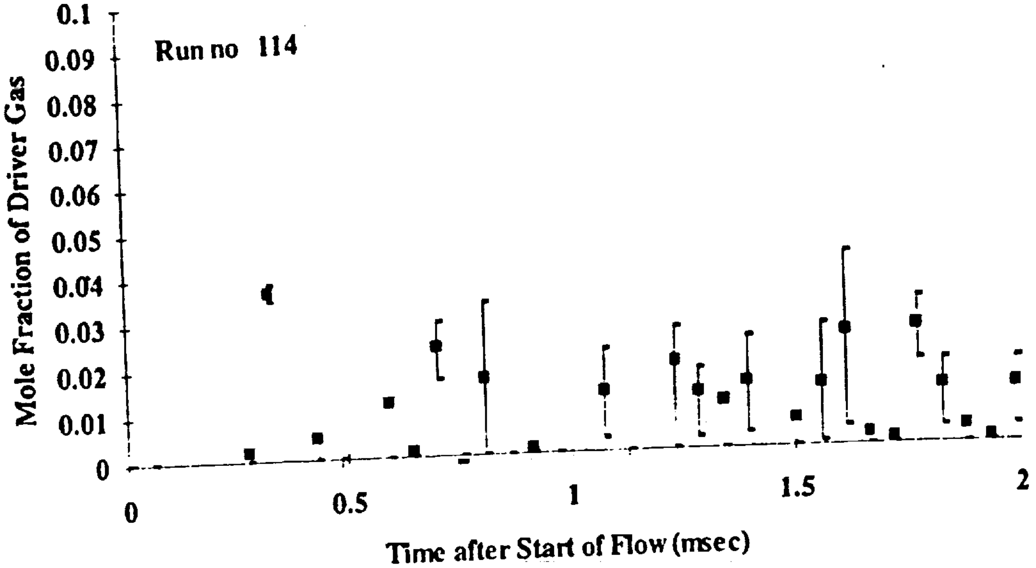

Figure 6.11 (c) The Contamination Level of the Test Gas
(Condition D and 5 mm off axis)

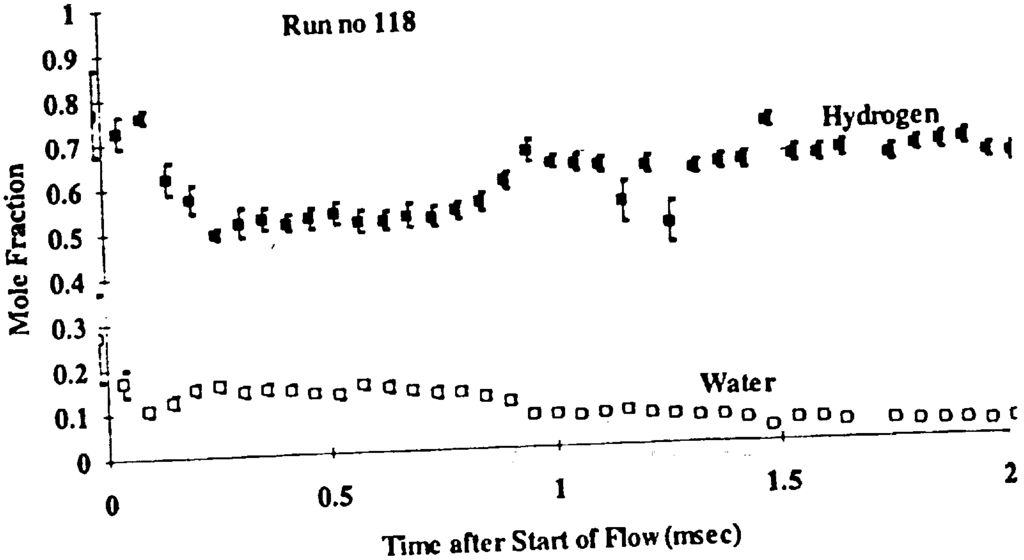

Figure 6.12 (a) The Mole Fraction of Hydrogen and Water as a Function of Time
(Condition A and 10 mm off axis)

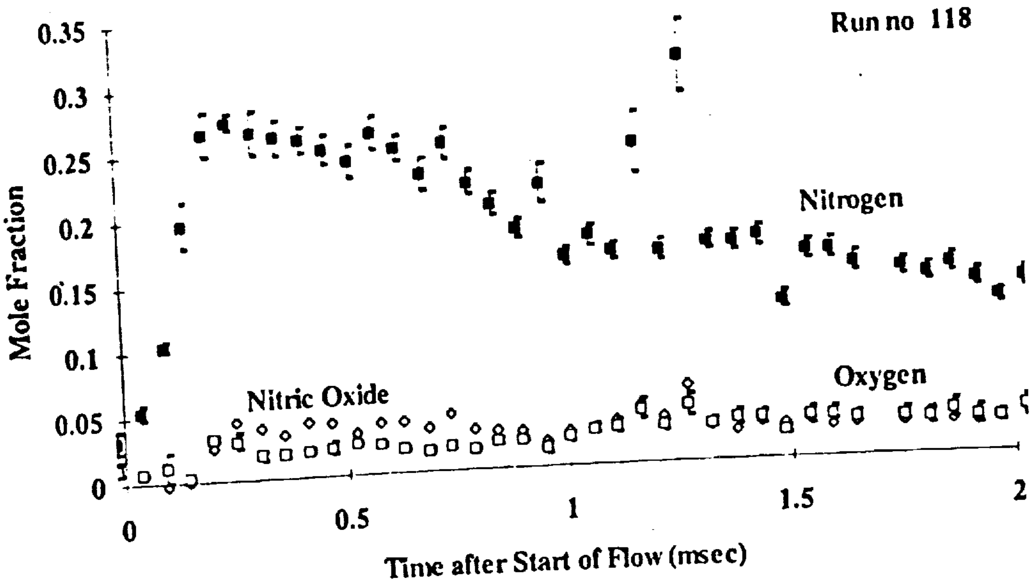

Figure 6.12 (b) The Mole Fraction of Nitrogen Oxygen and Nitric Oxide as a Function of Time (Condition A and 10 mm off axis)

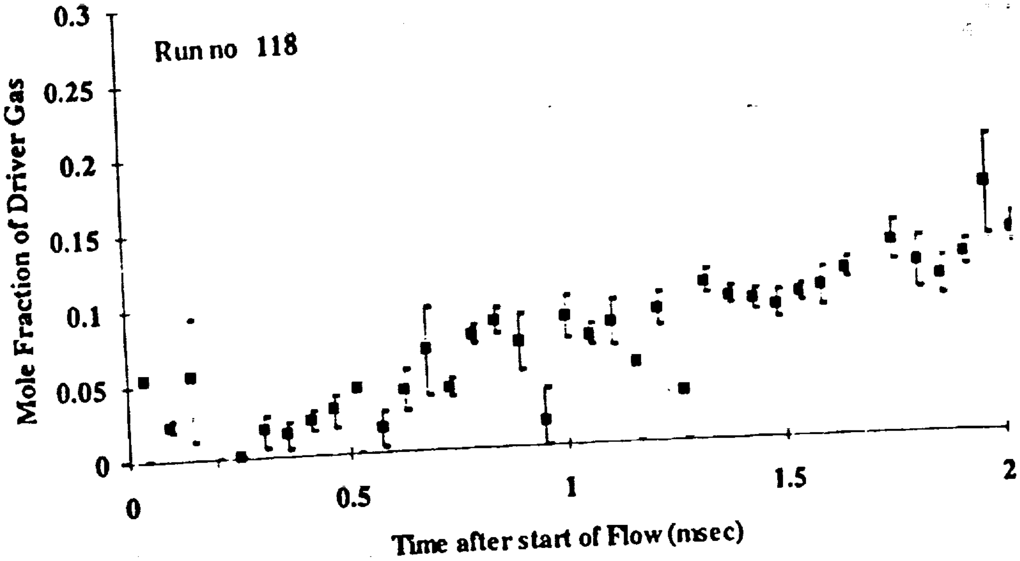

Figure 6.12 (c) The Contamination Level of the Test Gas (Condition A and 10 mm off axis)

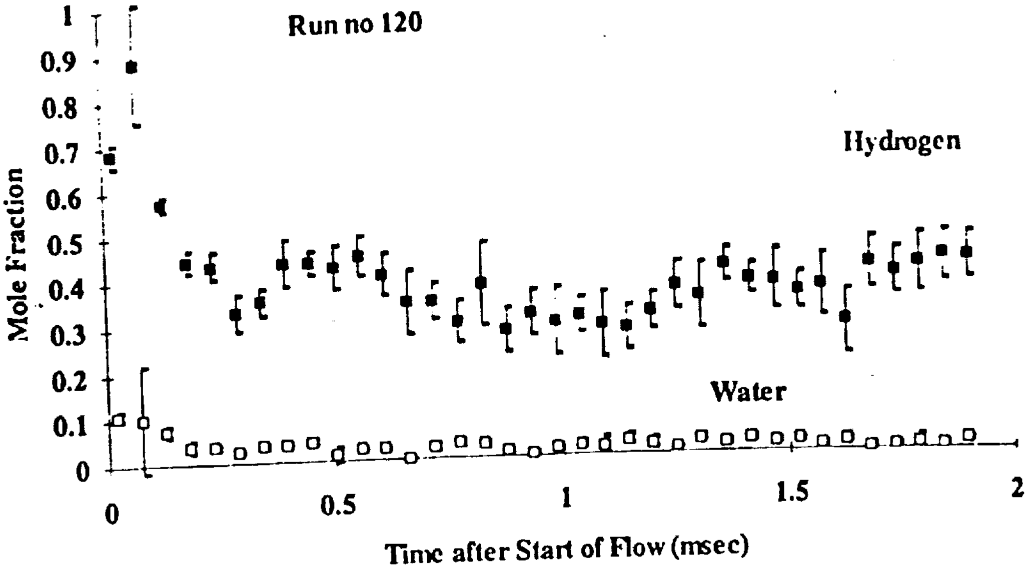

Figure 6.13 (a) The Mole Fraction of Hydrogen and Water as a Function of Time (Condition B and 15 mm off axis)

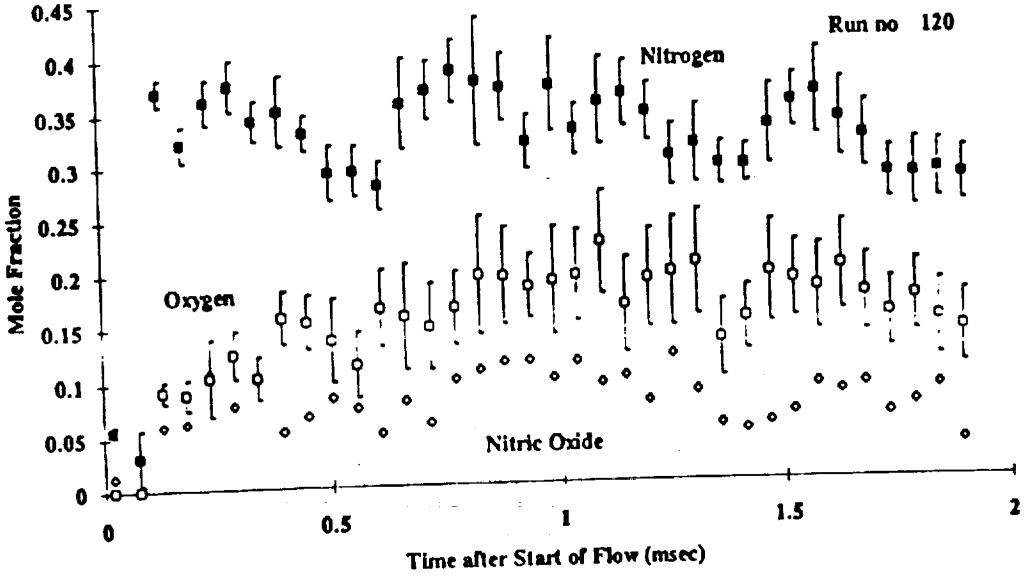

Figure 6.13 (b) The Mole Fraction of Nitrogen Oxygen and Nitric Oxide as a Function of Time (Condition B and 15 mm off axis)

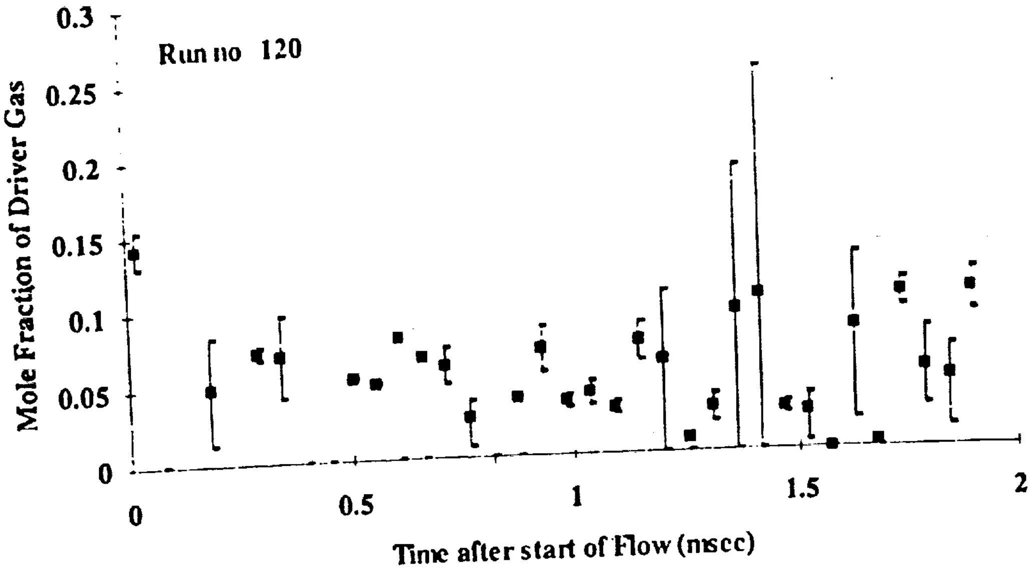

Figure 6.13 (c) The Mole Fractions of the Driver Gas
(Condition and 15 mm off axis)

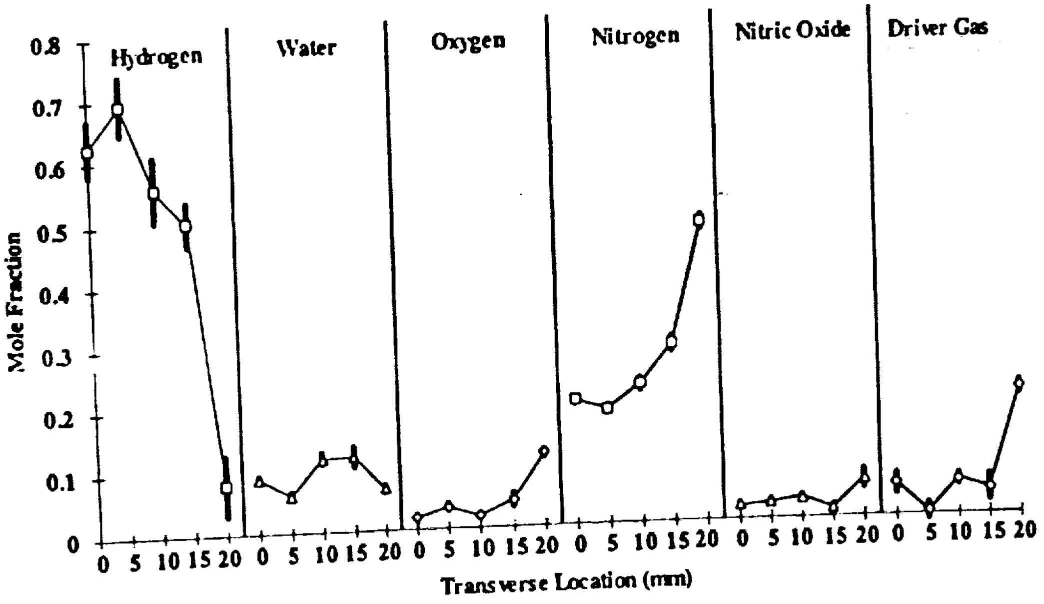

Figure 6.14 Mole fractions as a Function of Transverse Location
Condition A (12.2 MJ/kg)

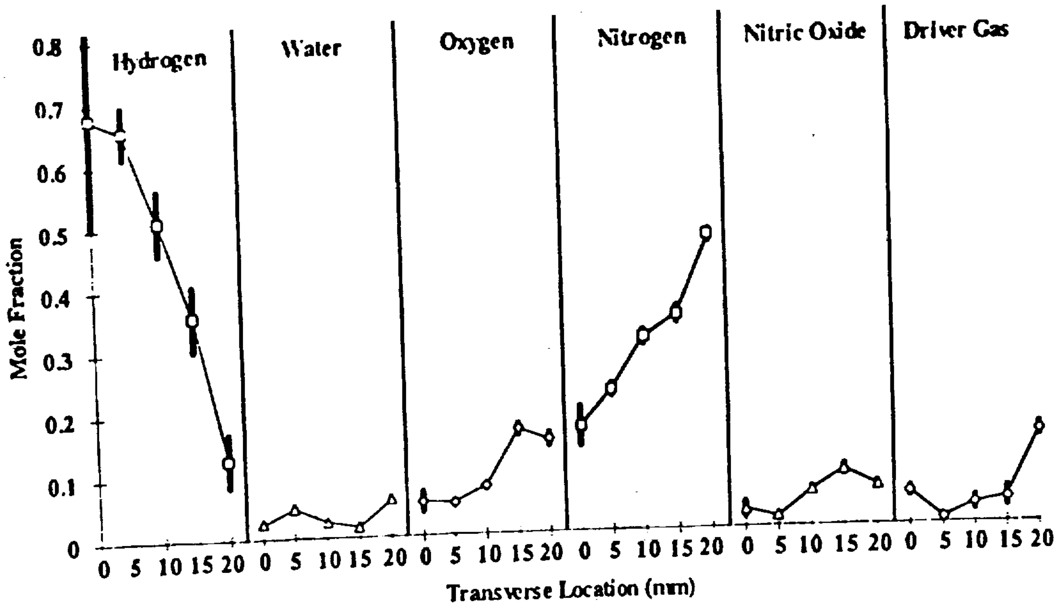

Figure 6.15 Mole Fractions as a Function of Transverse Location Condition B (9.4 MJ/kg)

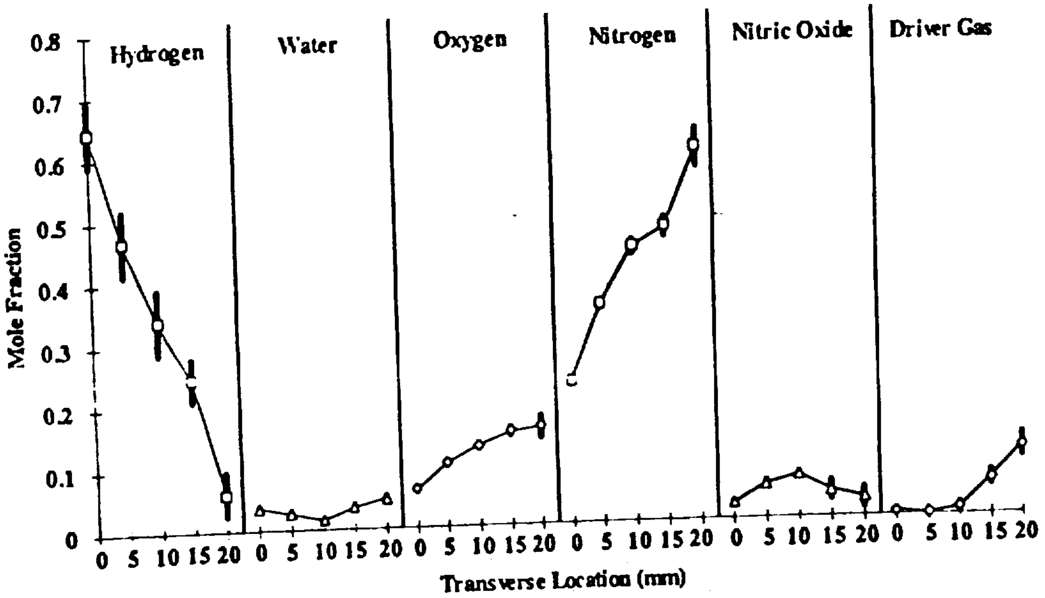

Figure 6.16 Mole Fractions as a Function of Transverse Location Condition C (7.8 MJ/kg)

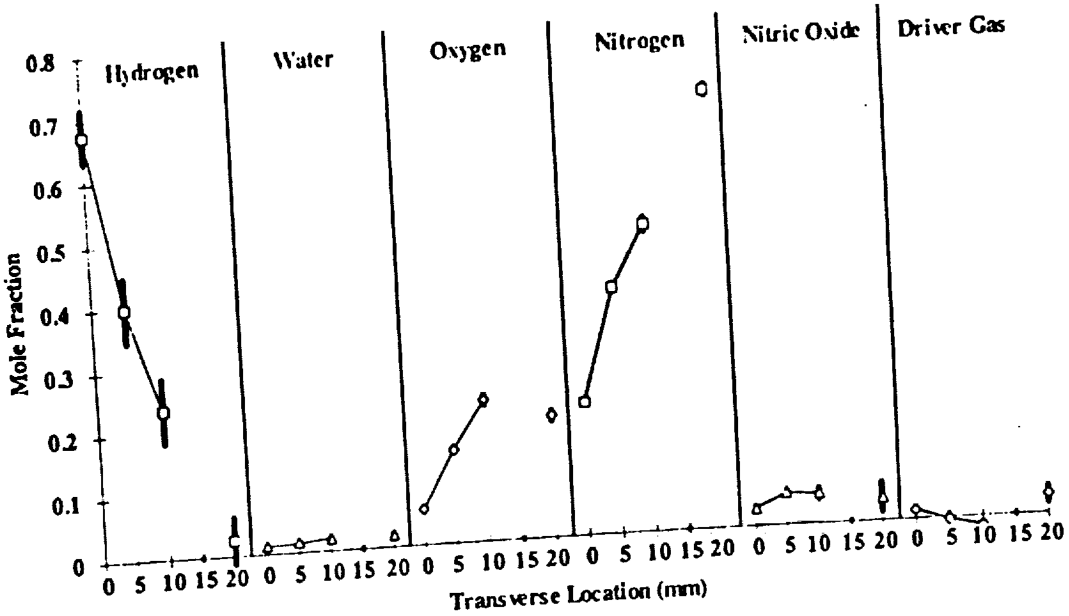

Figure 6.17 Mole Fractions as a Function of Transverse Location
Condition D (5.6 MJ/kg)

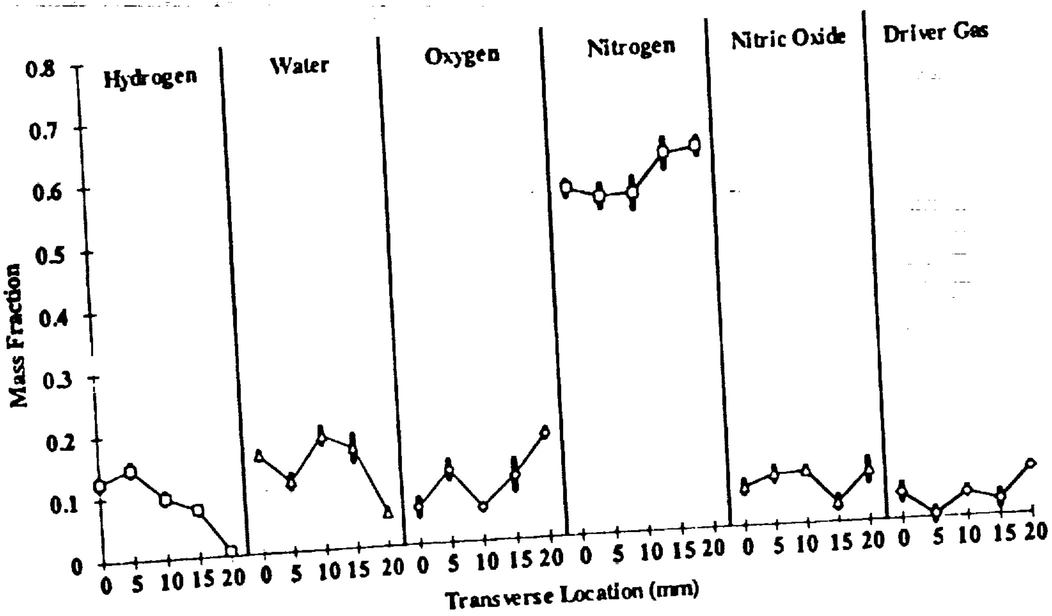

Figure 6.18 Mass Fractions Condition A (12.2 MJ/kg)

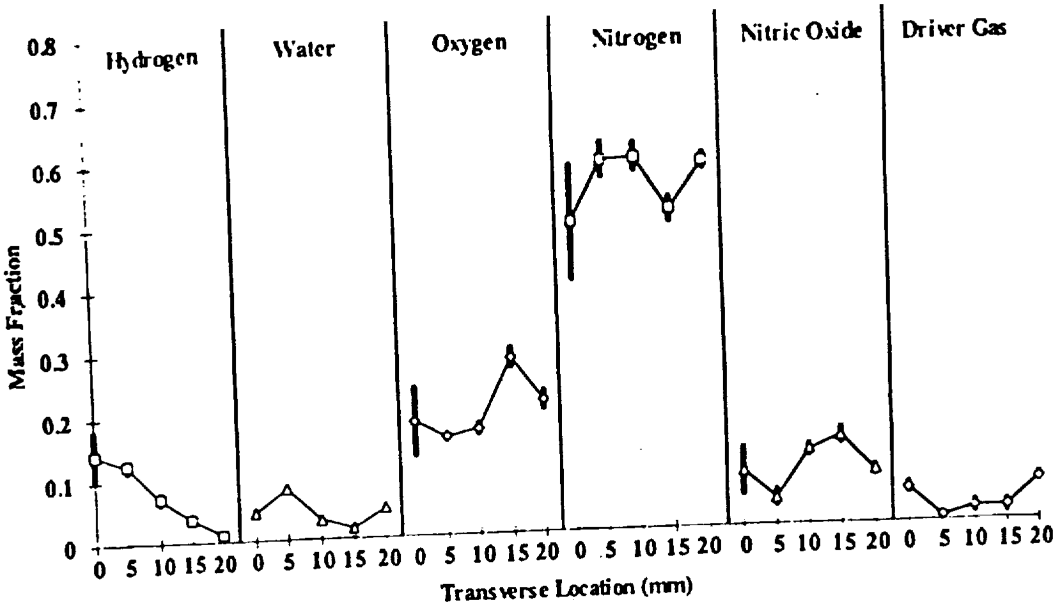

Figure 6.19 Mass Fractions Condition B (9.4 MJ/kg)

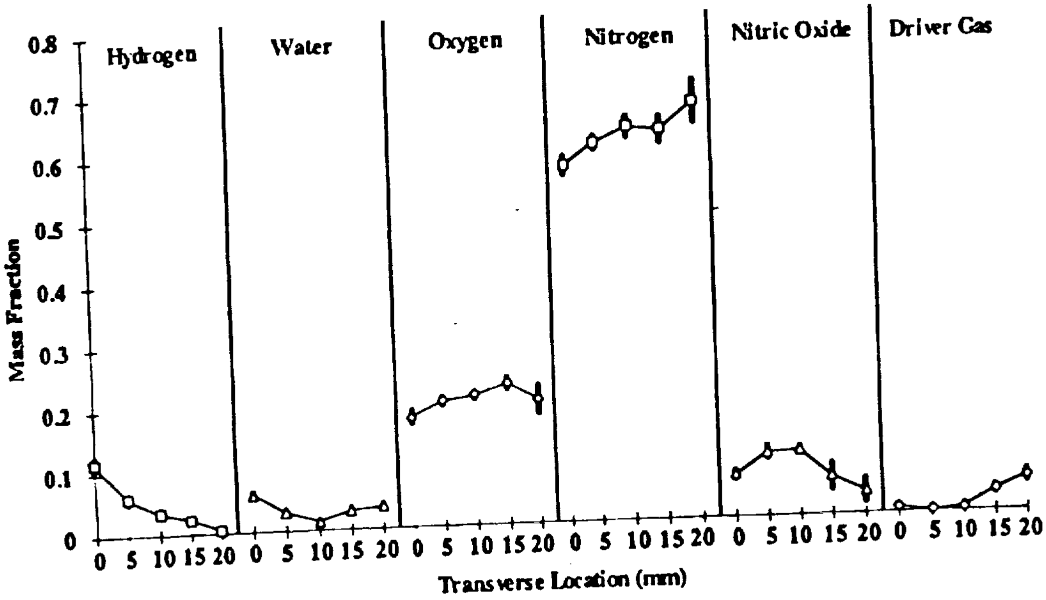

Figure 6.20 Mass Fractions Condition C (7.8 MJ/kg)

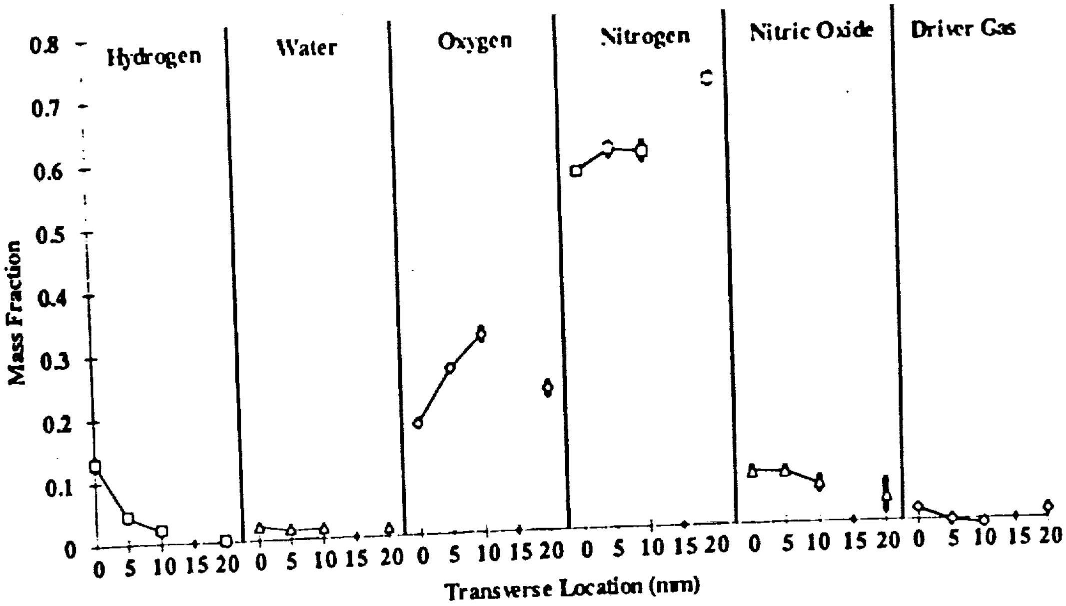

Figure 6.21 Mass Fractions Condition D (5.6 MJ/kg)

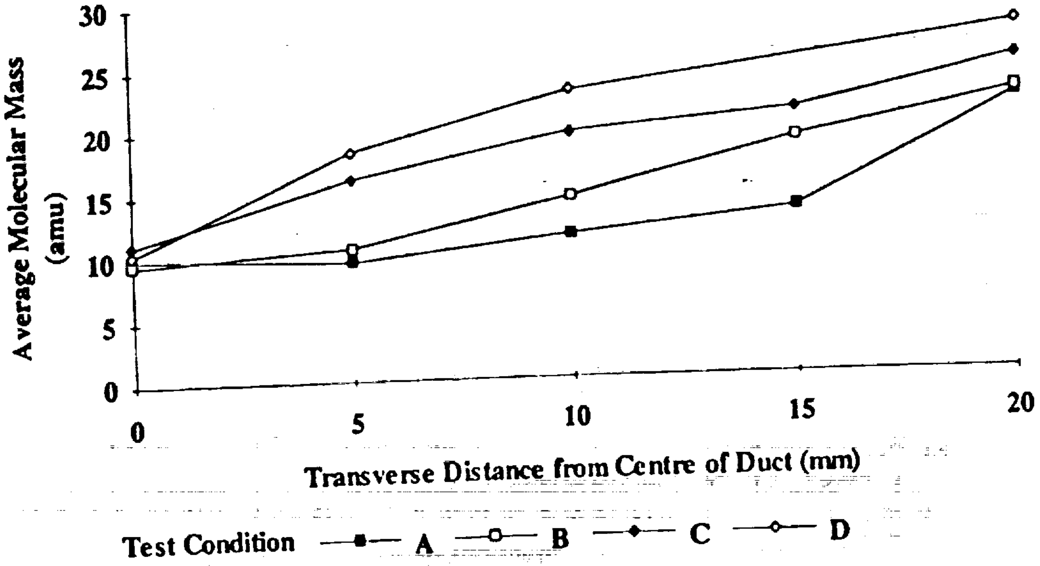

Figure 6.22 Average Molecular Weight across the Fuel Jet Mixing Region

6.3 DISCUSSION

Generally, the accuracy of the measurements was not as good as those of the driver gas. This was due to the problems with calibrations and performance of the instrument. The systematic error in the measurement of hydrogen was 20%, water 25%, nitrogen 10%, nitric oxide 10%, oxygen 10%, helium 5% and argon 10%. These estimates were dominated by the estimated error in the calibration constant. The random error in each measurement (due to the sampling rate or lack of peak definition) is included as an error bar for each measurement. Considering that this was the first time that measurements of this type had been performed, this level of error was not unexpected. Despite this, there is still a considerable amount of information contained in the measurements, much of it unique.

An additional difficulty with the results can be seen in the traces of the concentrations as a function of time (Figure 6.11, 6.12 and 6.13). That is, that the concentrations at each location in the flow were not steady with time. The general trend was for air-component concentrations to fall with time after peaking at around 0.5 msec of flow, while the hydrogen concentration rose with time after 0.5 msec. Where there was noticeable water, the water concentration fell with increasing time. An obvious explanation for this was that the effective height of the hydrogen fuel jet (after adjusting to the ambient static pressure) was increasing with time as the static pressure of the test gas fell. Such variations were independent of the operation of the mass spectrometer, and are therefore not so much a problem with the measurement, as with the interpretation of the data. In fact, this observation highlighted the importance of the instrument's ability to obtain time resolved measurements, as single instant concentration measurements would not reveal the unsteadiness of the combustion.

A comparison of the results from the different test conditions, indicated that the highest enthalpy air flow, Condition A, showed a considerable amount of water across the fuel jet. A small amount of water appeared to have been produced in Condition B, while in the two lower enthalpy conditions, there was no measurable amount of water produced. In all three of the lower enthalpy conditions there was significant penetration of the oxygen into the fuel jet without reaction. In Condition A, the amount of oxygen measured inside the fuel jet was not significant. This indicated that at only the highest enthalpy condition had complete reaction of the mixed air and fuel occurred, and that the combustion of the fuel was mixing-limited. In the three lower enthalpy conditions (B, C, and D), the fuel and air mixed but did not react. Condition B may be reaction-limited, since there was some water present, while Conditions C and D showed no evidence that ignition occurred. In all conditions, the measurement of large amounts of hydrogen within the jet indicated that nothing close to complete mixing of the fuel jet occurred.

At the defined test time, the transverse extent of the mixing region taken from the concentration measurements and the thickness of the momentum flux defect both increased with the increase in test flow enthalpy. Although the initial effective fuel jet thickness also increased with increasing enthalpy, this did not account for the relative size of the increase in jet height 500 mm downstream. The pitot pressure profiles and the mole fraction of the components of air are plotted simultaneously for the four test conditions in Figure 6.23. To obtain a measure of the penetration of the free-stream molecules into the fuel stream, the water was included as if it were dissociated into molecular hydrogen and oxygen. Therefore the mole fractions of test gas in the figure include the oxygen present in the form of water as well as the mole fraction of driver gas.

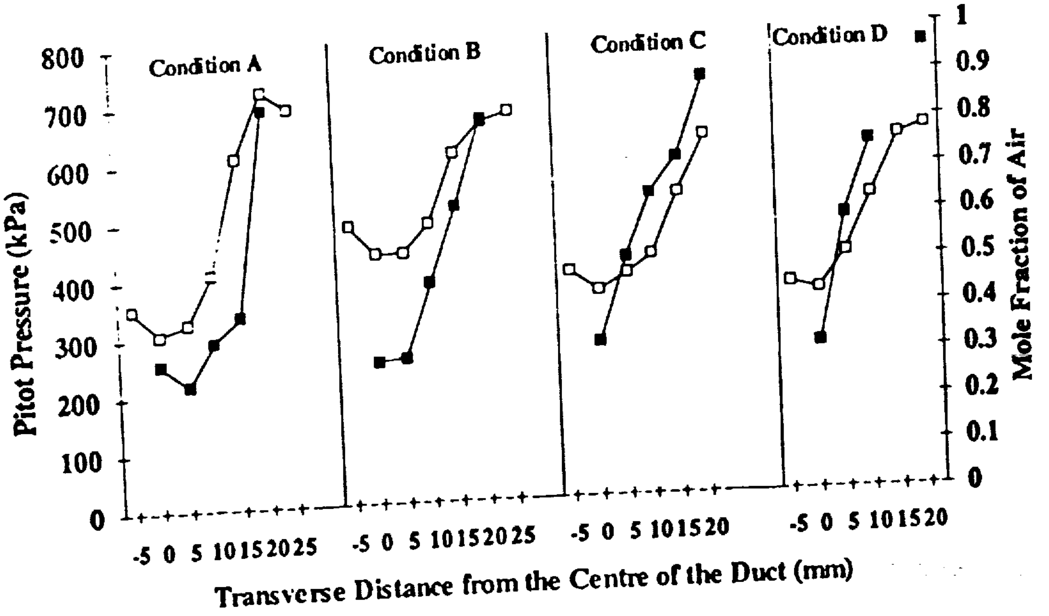

Figure 6.23 Comparison between the Pitot Pressure and the Air Mole Fraction 500 mm Downstream of the Injector.

(□ - Pitot pressure; ■ - Mole fraction of test gas (including water and driver contamination))

The free-stream pitot pressure and the hydrogen jet pitot pressure were predicted to increase as the enthalpy increased. This was reflected in the pitot pressure measurements, except in the centre of the jet at Condition A. In Condition A, the centre line pitot pressure was significantly below the expected levels, and represented a greater deficit in momentum flux (below the free-stream momentum flux) than the original momentum flux deficit of the fuel jet. That this occurred co-incident with combustion possibly indicated that the density was falling on the centre of the fuel jet as the temperature increased. If this was so, then the thickness of the fuel jet concentration profile would be expected to increase and the free-stream pitot pressure would be increased by the compression waves generated by the expansion of the stream tubes in the combustion zone. There was a greater increase in free-stream pitot pressure in Condition A than in the other test conditions. In Conditions B, C and D, the rise in free-stream pitot pressure was interpreted as a result of mixing stimulated compression waves.

The momentum flux profiles and the concentration profiles given in Figure 6.23 show a roughly equivalent height of the mixing region. This was expected in the case of a turbulent mixing region where the turbulent diffusion dominated over the molecular transport. In a free turbulent shear layer between two semi-infinite fluids, the growth rate of the height of the mixing region has been observed to grow linearly with downstream distance, (Figure 6.24), with the constant of proportionality being denoted the spreading coefficient, (Schetz, 1980). The spreading coefficient in a compressible flow has been found to be a function of the velocity ratio between the fuel and air streams, the density ratio, the level of density fluctuations, the Mach number of the turbulent structure in the shear layer, the rate of heat release in a chemically reacting flow and the initial turbulence levels in the free-stream flows, (Dimotakis, 1991). Even in the case of equal stream velocities, where intuition would suggest that the mixing would be slight, the initial turbulence and density fluctuations act to produce stronger mixing than molecular diffusion (Brown and Roshko, 1974).

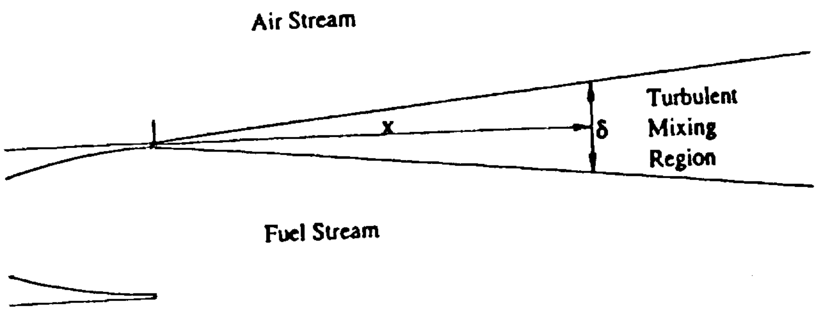

Figure 6.24 Definition of the Spreading Coefficient $\frac{\delta}{x}$

Shear layer growth of compressible flows at low Mach number can be adequately modeled by incompressible relations (Brown and Roshko, 1974). In incompressible non-reacting flows the spreading rate of a shear layer between two semi-infinite fluids has been correlated to the function (Dimotakis, 1991):

$$\frac{\delta}{x}(r,s) \approx C_\delta \frac{(1-r)(1+s^{1/2})}{2(1+s^{1/2}r)}\left(1 - \frac{(1-s^{1/2})/(1+s^{1/2})}{1+2.9(1+r)/(1-r)}\right) \qquad (6.6)$$

where r is the velocity ratio and s is the density ratio between the two streams. The constant depends on the facility and other unknown factors and has fallen in the range $0.25<C<0.45$. Values of density and velocity ratios are listed in Table 6.6 for test conditions A to D.

Table 6.6 The Empirical Predictions of Spreading Coefficient and Mixing Region Height for the Experimental Conditions

	Condition A	Condition B	Condition C	Condition D
Velocity Ratio, $U_j:U_\infty$	0.5	0.6	0.65	0.74
Density Ratio, $\rho_j:\rho_\infty$	1.1	0.8	0.54	0.35
Incompressible Spreading Coefficient	0.11	0.09	0.07	0.05
Convective Mach Number	1.2	1	0.87	0.6
Predicted Compressible Spreading Coefficient	0.02	0.02	0.02	0.02
Predicted Mixing Region Height (mm)	11	10	10	12

An extension to compressible non-reacting shear layers has been suggested by Papamoschou and Roshko (1988). They introduced the concept of a convective Mach number as a measure of the compressibility of the flow. In a flow with uniform ratio of specific heats, the convective Mach number is defined by

$$M_c = \frac{U_1 + U_2}{a_1 + a_2} \tag{6.7}$$

where M_c is the convective Mach number, U is velocity and a the speed of sound, with 1 and 2 denoting each stream. This equation represents the Mach number of the large scale turbulent structure with respect to the gas free-stream. For the experimental conditions of the current measurements, the convective Mach number is given in Table 6.6. Using this as the defining measure of compressibility, the spreading rate is reduced below that predicted by Equation 6.7 as the convective Mach number increases. The experimental measurements are correlated by an empirical relation:

$$f(M_{c1}) = 0.8\,e^{-3M_{c1}^{2}} + 0.2 \tag{6.8}$$

Where f represents the reduction in the compressible spreading rate from the incompressible. This relation is plotted in Figure 6.25 along with the experimental data which it is meant to represent (sources not included). As can be seen the majority of data is taken at convective Mach numbers less than one. The spreading coefficient predicted from the convective mach numbers of the current test conditions are also given in Table 6.6. As can be seen, the opposing effects of velocity and density variations and the convective Mach number combine to produce an equivalent predicted spreading coefficient for each experimental condition.

In the experimental situation described here, immediately behind the injector, two shear layers are present, one on either side of the fuel jet. Each is expected to spread with downstream distance, although not necessarily independently from the influence of the other. The two shear layers would be coupled by the waves they produced. Each set of waves would travel through the opposite shear layer, possibly generating additional turbulence and increasing the mixing rate. At some point downstream, the two shear layers would intersect and the nature of the flow would change from dual shear layers to a jet/wake flow. After this had occurred, (though perhaps before, due to the coupling), the empirical results from semi-infinite shear layer growth would no longer apply to the growth of the mixing region.

Upstream of the intersection of the two shear layers, the properties on the centre of the jet would remain close to the original properties and the pitot pressure and concentration profiles should show axial values equivalent to those at the start of the jet. This region of near constant properties is referred to as the potential core. Downstream of the potential core, the axial flow properties approach the free-stream properties, and the decrease in difference in quantities usually follows an inverse power law form with distance. In the far downstream, the transverse gradients of velocity and temperature become small and the growth of the shear could be approximated quite well by the incompressible growth rates (Bradshaw, 1977).

Assuming that the coupling between the two shear layers was not significant, the length of the potential core could be estimated from the height of the fuel jet and the predicted compressible spreading coefficient. In these experiments, this length is 120 to 130 mm, indicating that for most (75%) of the distance between the injector and the measurements, the

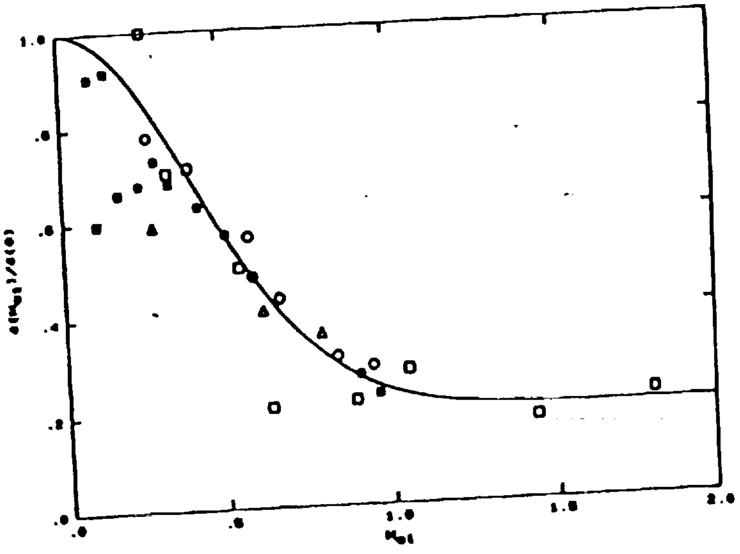

Figure 6.25 Ratio of Compressible to Incompressible Shear-Layer Growth as a Function of Convective Mach Number
(Dimotakis, 1991, Fig 4)

mixing region will be behaving as a jet/wake flow and the empirical correlations for semi-infinite shear layers will not apply. It remains of interest, however to discover how much greater the growth rate is in a jet/wake mixing layer than in a free shear layer, and if the predicted independence of the spreading rate with experimental conditions also applies to the jet/wake flow.

From the measurements, the half-height of the total mixing region was approximately 20 to 25 mm for Conditions A, B, and C and approximately 20 mm in Condition D. If the initial distance required for the isentropic compression of the fuel jet to the ambient pressure was ignored, then the spreading rate was about 40/500 or 0.08 (0.07 for Condition D). This was much larger than the predicted spreading coefficient for free shear layers and represented a much faster mixing and entrainment of the jet and free-stream gas than did a single shear layer. The incompressible spreading coefficient for free shear layers was larger than, but much closer to, the measured spreading rates. This was consistent with the conclusions reached by Casey (1991) from strut injection measurements in a narrow duct. His experiments were also conducted far enough downstream for the flow to become jet/wake dominated. The independence with test conditions does not seem to apply to the jet/wake flow since the height of the mixing layer is seen to grow with increased enthalpy.

Few other measurements of species profiles in shear layers have been reported, and none in a high temperature, high Mach number flow. The few measurements that have been taken imply that the transport of momentum, energy and species between the two streams does not take place at equal rates. Chriss (1968) found that the centre line variations of hydrogen concentration and momentum along the axis of a free-jet followed different functional forms. Ginevskii (1966) found that the transport of heat occurred twice as fast as the transport of momentum across shear layers in incompressible flows. The current results indicate that for these experimental conditions the transport properties are very similar.

Past research has shown that turbulence levels in the facility have an influence on the growth rate of the mixing layer. This was not quantified in these experiments, although the noise level in the pressure measurements was quite large.

In summary then, the state of knowledge of the mixing between supersonic fuel and air behind a parallel injector is not sufficient to theoretically explain the existing measurements nor to predict the outcomes of new experiments. In such a situation, measurements of concentration profiles across the mixing region downstream of such a combustor must be a valuable addition to the measurements of density and pressure which are routinely obtained. Confidence in numerical simulations relies upon the ability of the equations used to model the flow being able to reproduce experimentally obtained results. For these reasons also, the exploration of new measurements in new flow conditions is essential to the development of better understanding and modeling of the physically dominant processes in supersonic combustion.

These experiments in hypersonic combustion have only scratched the surface of the potential mass spectrometry offers to this field. The presentation of these results and their consequences has been necessarily brief, as further detail is beyond the scope of this thesis. The information obtained from these initial experiments pose more questions than answers and highlight many further avenues for research. In particular, research is required to more clearly define the mechanisms controlling the spreading rate in parallel injection in a supersonic flow as well as to sample the gas closer to the injector in order to determine whether the spreading rate changes significantly in the far downstream. It would also be valuable to perform numerical simulations of the current experimental conditions in order to gain a greater understanding of the turbulent mixing present in supersonic combustion.

91A46342

Transition of compressible high enthalpy boundary layer flow over a flat plate

Y. HE
Department of Aerospace and Mechanical Engineering,
University College, University of New South Wales,
Australia

and

R. G. MORGAN
Department of Mechanical Engineering,
University of Queensland,
Australia

ABSTRACT

This paper presents the results of an experimental investigation into the characteristics of boundary layer transition to turbulence in hypervelocity air flows. A series of experiments was conducted using a flat plate model, equipped with static pressure and thin film heat transfer transducers, in a free piston shock tunnel. Transition was observed in the stagnation enthalpy range of 2·35 to 19·2 MJ/kg. The transition Reynolds number correlates well with the unit Reynolds number through a simple empirical relation. The influences of Mach number, pressure and wall cooling are examined. The measured heat transfer rates in laminar and turbulent regions are compared with empirical predictions. Freestream disturbances of the test flow were also measured and analysed.

NOTATION

a	speed of sound
A	wave amplitude in unstable region
A_0	wave amplitude at the neutral point
A_1	amplitude of the sound radiated from the nozzle wall boundary layer
C	constant of proportionality
D	diameter of the nozzle
E	normalised power density
f	frequency (Hz)
f_p	peak frequency (Hz)
F	dimensionless frequency = $f\nu/u^2$
F_m	dimensionless frequency of the most amplified mode
H	specific enthalpy (J/kg)
L	model length (m)
M	Mach number
p	pressure (Pa)
p_a	atmospheric pressure
P_t	pitot pressure (Pa)
q	heat flux (W/m^2)
R	specific gas constant (kJ/kg K)
Re	Reynolds number based on the distance from the leading edge
Re_e	transition end Reynolds number
Re_t	transition onset Reynolds number
Re_u	unit Reynolds number (1/m)
St	Stanton number = $\frac{q_w}{\rho U(h_r - h_w)}$
t	time (s)
T	temperature (K)
U	flow velocity (m/s)
γ	ratio of specific heats; intermittency factor
η	fraction of transition zone defined by Equation (9)
λ	driver gas compression ratio
ρ	density (kg/m^3)
τ	test time (s)
υ	kinematic viscosity (m/s)
< >	average quantity

Subscripts

0	stagnation quantity
w	quantity at the wall
r	recovery quantity

Superscript

'	fluctuating quantity

Manuscript received 1 March 1993, revised version received 30 September 1993, accepted 23 December 1993.
Paper No. 1939.

INTRODUCTION

The prediction of boundary layer transition is generally a problem related to high Reynolds number flows. Transition has been closely investigated for many flow situations in the past, but there has been little investigation into the transition phenomena relating to hypersonic, high enthalpy flows. The boundary layer has a significant influence on the external flow fields of re-entry bodies, such as the Space Shuttle, and would have a critical influence on hypersonic duct flows such as those created in scramjet engines.

In the case of subsonic and supersonic flows of low enthalpy, boundary layer instability and transition have been accepted to be related to the unit Reynolds number, Mach number and the cooling of the wall(1). The existence of unsteady waves in the boundary layer has been substantiated by linear stability theory and revealed by experiment(2). The onset of boundary layer transition is marked by the departure from linear boundary layer characteristics which were associated with the appearance of local ber- turbulent (non-linear) events. The corresponding Reynolds num- ber, in cases of zero pressure gradient flow over flat plates and cones, was of the order 10^6. When correlated with the influential parameters, transition Reynolds number always showed an increasing trend with increases in unit Reynolds number, Mach number and boundary layer cooling. It was thought at one time that sufficient surface cooling could result in complete boundary layer stability and the possibility of maintaining the laminar status indefinitely(3).

When flow speed becomes hypersonic, however, some funda- mental changes occur in the early stages of transition, which are associated with the development of linear instability waves(4). Lin- ear stability analysis demonstrated that in addition to some low frequency, or first mode instability waves which are dominant in subsonic and supersonic boundary layer flows, there exist higher frequency, or second mode instabilities, in hypersonic boundary layers. This second mode overtakes the role of the first mode and becomes dominant in the process leading to transition. Linear sta- bility theory(4) indicates that boundary layer cooling, as deter- mined from wall to stagnation temperature ratio, will enhance sec- ond mode instability in hypersonic boundary layer and thus reduce the effect of first mode disturbances. Linear stability exper- iments conducted by Stetson and Kimmel(5) discovered that the wavelength of the second mode disturbances was equal to twice the boundary layer thickness. This assumed that the wave velocity was the same as the velocity at the boundary layer edge. Stetson and Kimmel speculated that second mode disturbances were un- likely to be dominant in the transition process. Consequently, sur- face cooling should delay transition in the hypersonic boundary layer. However, when second mode disturbances were known to be dominant, cooling of the surface would promote transition of the boundary layer. This was also supported by Seddougui's(6) nu- merical study which stated that surface cooling enhances the Tollmein-Schlichting viscous mode activity, and accelerates the transition process in the compressible boundary layer.

Previous hypersonic transition experiments by various re- searchers have yielded inconsistent conclusions. Deem and Mur- phy(7), and Ross(8) have indicated that there was little influence of wall to recovery temperature ratio T_w/T_r on the location of the transition point. Demetriades(9) observed in experiments conduct- ed with a conical model that wall cooling definitely caused a sub- stantial upstream movement of the transition zone. Shock tunnel experiments by Stetson and Rushton(10) demonstrated a reduction in transition Reynolds number as the temperature ratio T_w/T_r was reduced. The results of Richards and Stollery(11) showed that the increase of T_w/T_r may cause transition reversal and re-reversal. The conclusion reached by Cary(12) was opposite to all of the above. He observed a moderate increase in transition Reynolds number with wall cooling and no transition reversal.

All of the above mentioned hypersonic transition experiments had relatively low stagnation temperatures or enthalpies and hence the flow velocities were also relatively low. The test conditions of these experiments were unlikely to cover the velocity range encountered by future space planes. Therefore, transition data on hypervelocity boundary layer flows are still required.

One of the features of hypervelocity and high enthalpy flow is that high temperature and high heat transfer rate is generated when the flow is bounded by a solid wall. In other words, surface cooling is relatively severe. Also, chemical reactions, such as the dissociation of oxygen and nitrogen molecules, are bound to occur in high temperature flows. The real gas effects are unknown fac- tors in any transition study. In the present work an attempt is made to investigate the influence of freestream unit Reynolds number, pressure, and wall cooling, on the transition under such conditions.

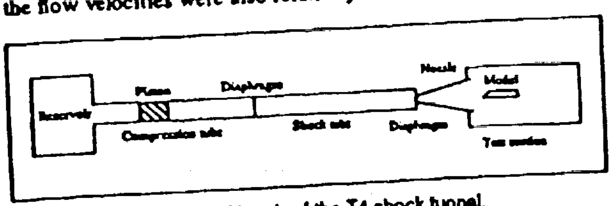

Figure 1. Sketch of the T4 shock tunnel.

EQUIPMENT AND EXPERIMENTAL CONDITIONS

Experiments were conducted at the University of Queensland(13) using the T4 free piston shock tunnel (Fig. 1). A contoured nozzle with a fixed area ratio was used and the nominal Mach number was 5·0. A flat plate model (Fig. 2) with a 30° sharp wedge was placed in the test section. The bluntness of the model leading edge was 0·08 mm, the total length of the plate was 600 mm and its width 230 mm. A fence (not shown in Fig. 2) was attached to each side of the model to curtail the disturbances generated at the corner of the leading edge. The first transducer hole was 50 mm from the leading edge, the second 74 mm and the third 100 mm. Consecutive transducers were 17·5 mm apart.

The stagnation enthalpy of the flow varied in the range 2·35–26 MJ/kg. The nominal conditions were T_0 = 2130–9130K, p = 4·8–26 kPa and M = 5·2–6·6. The flow speed varied from 2·1 to 6·0 km/s. The change in static pressure was achieved by vary- ing the thickness of the primary diaphragm in the shock tube. Thin film gauges were flash mounted along the model to measure sur- face temperatures during the tests, and temperature traces were then integrated to obtain heat transfer rates. A pressure transducer was also mounted in the plate to obtain a reference static pressure and to determine the steady flow conditions.

The main objective of the present investigation was to detect the transition phenomenon in hypersonic and high enthalpy boundary layer flows. However, the enthalpy range over which transition is observed is limited by the lengths of the test core and the model. In shock tunnel tests with a fixed nozzle, high enthalpy is achieved by increasing stagnation and static temperatures. The reduced density ($\sim 1/T$) and increased viscosity ($\sim (T)^{0.5}$) offset the increased velocity ($\sim (T)^{0.5}$), leading to an overall reduction of unit Reynolds number with the test flow velocity. As the flow enthalpy increased, the unit Reynolds number decreased and the Reynolds number based on the distance from the leading edge also

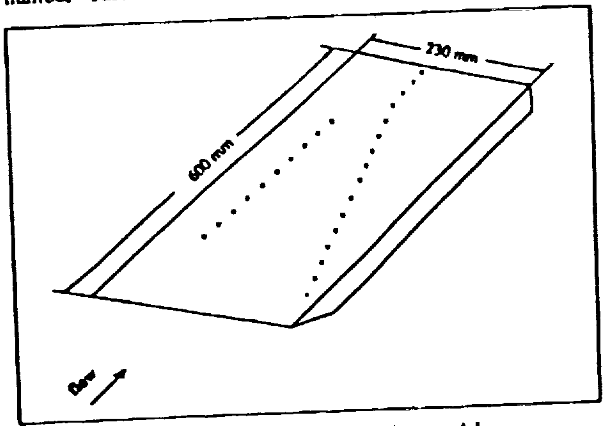

Figure 2. Sketch of the flat plate model.

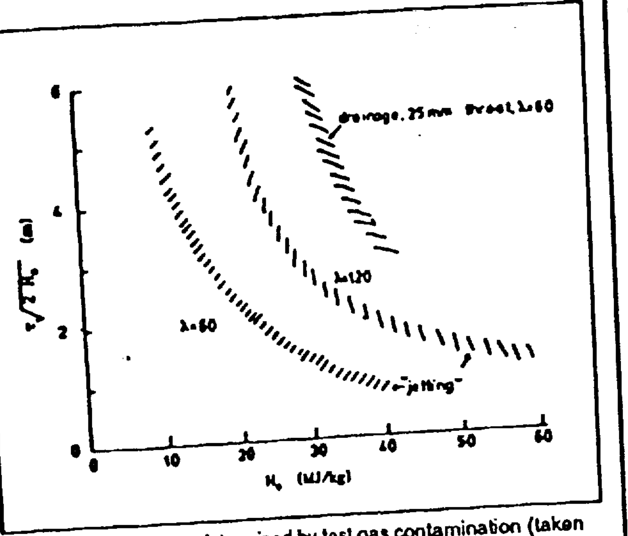

Figure 3. Test time determined by test gas contamination (taken from Stalker and Morgan(13)).

decreased. Therefore, the onset of transition was delayed further downstream from the leading edge at high enthalpy, and finally beyond the model length. The maximum stagnation enthalpy of the flow tested was 26 MJ/kg but no onset of transition could be detected for stagnation enthalpies over 19·2 MJ/kg.

The decay of stagnation pressure could be a concern when a steady flow over the test model is required for the examination of transition. If the flow speed at the test section is U and the model length is L, then the time required for flow to pass the entire model is

$$t=\frac{L}{U} \qquad \ldots(1)$$

The behaviour of stagnation pressure during this time interval is crucial for the establishment of test flow over the model. For the worst case, i.e. when the flow speed is the lowest, we have

$$t=\frac{0\cdot 6}{2100}=2\cdot 9\times 10^{-4}\,\mathrm{s}=290\,\mu\mathrm{s}$$

Over this period the reservoir pressure is reduced by 20%. This amount of decay did not substantially influence heat transfer measurement through which transition was detected as discussed later. It should be noted that the laminar region of the boundary layer was shorter than the model length. The pressure decay during the period when the test flow passed the entire laminar region was smaller than that estimated above. Therefore, the test flow produced in the T4 shock tunnel was considered reasonably steady for the study of boundary layer transition.

To investigate the influence of decaying total pressure on transition, a series of runs was performed with 20% argon and 80% helium driver gas mixture. This reproduced the flow conditions at an enthalpy of 3·5 MJ/kg, but with no decay in stagnation pressure. No difference in transition onset point was detected. However, both the maximum stagnation enthalpy and contamination free test time achievable by mixed driver gases were smaller than those achieved by helium driver.

The test time in a high-enthalpy reflected shock tunnel was limited by the driver gas contamination of the test gas. The gas at the vicinity of the shock tube wall undergoes a bifurcated reflected shock, and suffers a smaller change in velocity than the centralised gas which passes through a normal reflected shock. It therefore forms a jet penetrating into the test gas region along the wall, which in turn reduces the test time. This problem had been investigated by Stalker and Crane(14) who formulated a theory to estimate the length of useful test time produced by reflected shock tunnel facilities. Using this theory, Stalker and Morgan(13) calculated the test time in terms of test slug length $\tau(2H_0)^{0.5}$ vs the stagnation enthalpy at the diaphragm rupture pressure of 57 MPa (Fig. 3). For $\lambda = 60$ and $H_0 = 20$ MJ/kg the test slug was about 2 m which was more than three times the model length. The stagnation enthalpies of all data-acquiring test runs of the present investigation were less than 20 MJ/kg and the test slugs were always longer than 2 m according to Fig. 3. It can be concluded that the T4 free piston shock tunnel provided sufficient test time for the establishment of transitional boundary layer flow over the flat plate model used. This conclusion was also supported by the establishment of steady heat transfer rate within that test period.

The nozzle reservoir stagnation conditions were calculated using the ESTC(15) computer program. It uses the initial shock tube filling pressure, temperature and the measured incident shock speed to calculate the stagnation condition behind the reflected shock. It then isentropically expands this stagnation condition in equilibrium until the stagnation pressure matches the value measured during the useful test flow period. The gas is assumed to be stationary at this expanded condition, thereby leading to a loss in total enthalpy from shock reflection conditions.

The test section freestream conditions were calculated using the NENZF computer program(16). Given the stagnation conditions in the nozzle reservoir, i.e. the end of the shock tube, the program computes the expansion of the test gas through the nozzle. The following calculation scheme was used. Chemical equilibrium was assumed for the flow upstream of the throat. Chemical nonequilibrium calculations began downstream of the throat and the chemical kinetics provided by Lordi *et al*(16) were used. The thermodynamic properties of the constituent gases were modelled by fitted polynomial curves for temperatures greater than 5000K and by a harmonic oscillator model below this temperature. All vibrational modes were assumed to be in equilibrium with the flow temperature throughout the nozzle. The above calculation scheme was verified by the measurement of pitot and static pressures in the test section of the tunnel. The differences between the calculated and the measured quantities were estimated to be within ±15% for the enthalpy range within which the transition experiment was conducted.

FREESTREAM DISTURBANCE MEASUREMENT

Experiments examining the intensity of freestream disturbances were conducted in the T4 shock tunnel. A pitot rake was mounted vertically in the test section about 158 mm downstream of the nozzle exit, and consisted of six pitot pressure probes with a distance of 30 mm between each adjacent probe. A PCB pressure transducer with a response time of less than 2 µs, was mounted in each of the probes. The response frequencies of the pitot probes were not less than 400 kHz, and the pressure signals were sampled at a rate of 500 kHz. The maximum frequency discernible from the recorded data was not less than 250 kHz.

Pitot pressure measurements were taken for a range of test conditions. Figure 4 demonstrates the variations of the fluctuation intensity with the unit Reynolds number. It does not indicate the existence of any correlation between pitot pressure fluctuation intensity and the unit Reynolds number. Each data point represents the averaged value of fluctuation intensities of the pitot probes mounted in the rake.

Direct measurement of continuous flow velocity in the shock tunnel facility was not possible. The flow disturbance or the noise level which is often indicated by freestream velocity fluctuation intensity was therefore difficult to obtain by direct measurement. However, it is possible to get an indirect estimate of this quantity from pitot pressure measurements. The relation between fluctuation intensity of the velocity and that of pitot pressure is discussed below.

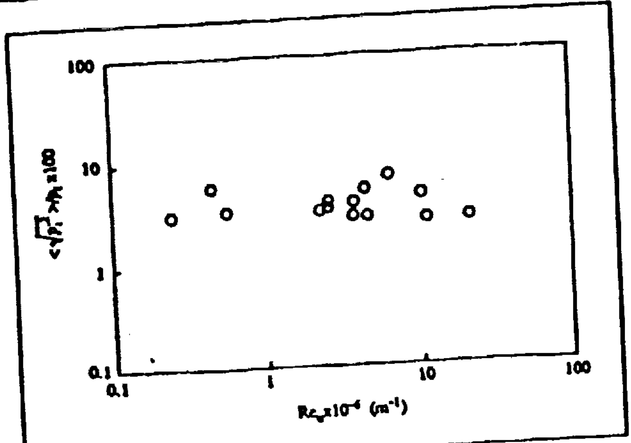

Figure 4. Pitot fluctuation intensity *vs* unit Reynolds number.

From the Rayleigh pitot tube formula the following relation for the pitot pressure P_t in a hypersonic flow field can be obtained, assuming the gas is perfect,

$$P_t = C\rho u^2 \qquad \ldots(2)$$

where C is a constant and

$$C = \left(\frac{\gamma+1}{2}\right)^{\frac{\gamma+1}{\gamma-1}} \gamma^{\frac{2-\gamma}{\gamma-1}} \qquad \ldots(3)$$

Taking the logarithm of both sides of Equation (2) and then differentiating yields

$$\frac{dP_t}{P_t} = \frac{d\rho}{\rho} + 2\frac{du}{u} \qquad \ldots(4)$$

Since radiated noise is predominant in hypersonic wind tunnels, it was assumed that velocity fluctuation was caused by sound waves travelling in the flow field, and that the contribution from vorticity fluctuation was negligible. The continuity equation which governs the variations in velocity and density due to acoustic waves can be written as follows, assuming one dimensional flow,

$$\frac{d\rho}{\rho} = \frac{du}{a} \qquad \ldots(5)$$

where a is the local speed of sound. By introducing Mach number into the above equation yields

$$\frac{d\rho}{\rho} = M\frac{du}{u} \qquad \ldots(6)$$

Substituting this into Equation (4) gives

$$\frac{dP_t}{P_t} = (M+2)\frac{du}{u} \qquad \ldots(7)$$

The fluctuating components P_t' and u' can be treated as small perturbations dP_t and du. Equation (7) then becomes

$$\frac{P_t'}{P_t} = (M+2)\frac{u'}{u} \qquad \ldots(8)$$

Therefore, we have

$$\sqrt{\frac{\langle u'^2\rangle}{u}} = \frac{1}{M+2}\sqrt{\frac{\langle P_t'^2\rangle}{P_t}} \qquad \ldots(9)$$

It can thus be seen that for hypersonic flow, where M >> 1, the velocity fluctuation intensity is much smaller than that of pitot velocity fluctuation intensity is only pressure. For M = 5, the velocity fluctuation intensity is only about 14% of the fluctuation intensity measured with pitot probe.

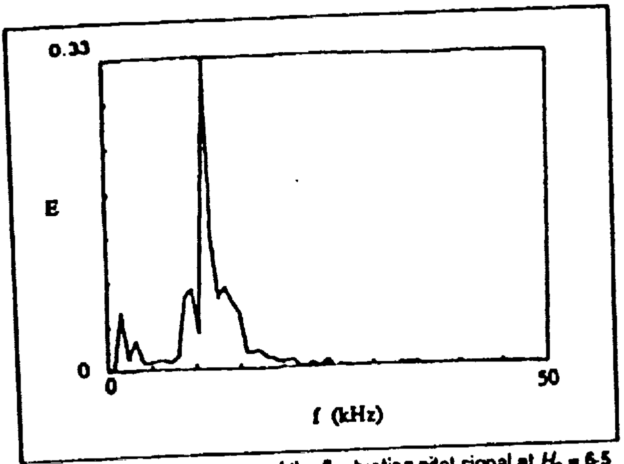

Figure 5. Power spectrum of the fluctuating pitot signal at H_0 = 6·5 MJ/kg. E = fraction of total fluctuation energy /(kHz).

Fourier transform was performed on the fluctuating pitot pressure signals, and a dominant frequency was observed in each of the power spectra. Figure 5 shows a typical power spectrum of the fluctuating component of the pitot signal. The power density E is normalised so that

$$\int_0^{\infty} E df = 1 \qquad \ldots(10)$$

Further analysis showed that this dominant frequency was proportional to the square root of the flow temperature (Fig. 6). Since the speed of sound in the test gas was proportional to the square root of temperature, it was expected that, with a characteristic length D, the characteristic frequency would be

$$f_p - \frac{a}{D} = \frac{\sqrt{\gamma RT}}{D} - \sqrt{T} \qquad \ldots(11)$$

where γ and R are assumed to be constant. Generally, Equation (11) can be written as,

$$f_p = C\sqrt{T} \qquad \ldots(12)$$

where the constant of proportionality C incorporates the properties of test gas, the geometry of the nozzle, and the mode of oscillation. The value of C was found to be 391 $s^{-1}K^{-1/2}$ through regression analysis. The origin of the dominant frequency in freestream disturbance has not been investigated but it was speculated that it may be pertinent to the fluctuation of the sonic surface at the exit of the nozzle throat.

The freestream disturbances discussed above were eventually

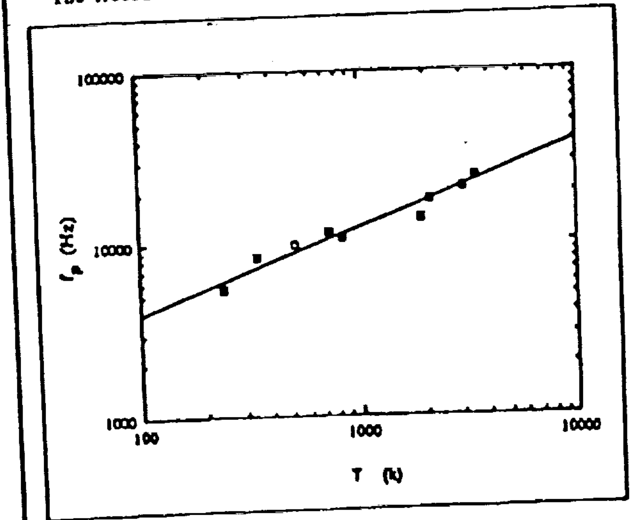

Figure 6. Peak frequency as a function of temperature.

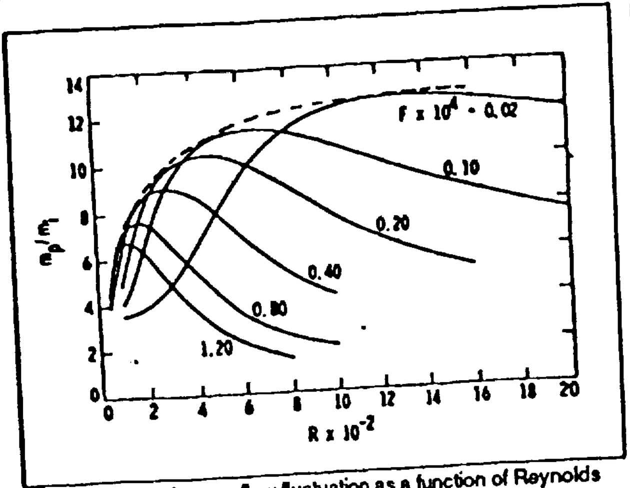

Figure 7. Peak mass flow fluctuation as a function of Reynolds number for six frequencies. Viscous forcing theory; M = 4·5, $\psi = 0°$, c = 0·65. Taken from Mack (1984). The envelope is added by the present authors. $R = (Re)^{0.5}$.

received and amplified by the boundary layer flow over the flat plate model, leading to transition to turbulence. During this amplification process, the boundary layer was selective about the frequencies carried in the disturbances. At a defined Reynolds number and Mach number, there is a most preferred, or the most amplified, frequency. This frequency generally depends on Mach number M, Reynolds number Re and wall to stagnation temperature ratio T_w/T_0. Linear stability forcing theory can be used to calculate the ratio of the stability wave amplitude A_0 at the neutral point to the amplitude A_1 of the sound radiated by the turbulent boundary layer on the nozzle wall. The calculation is often carried out in terms of mass flow fluctuation. If m_p is the peak value of the local mass flow fluctuation, and m_i is the amplitude of mass flow fluctuation of incoming instability waves, the ratio m_p/m_i represents, in a similar manner to the amplitude ratio A/A_0, the amplification of instability waves. Mack[4], using viscous forcing theory, computed the peak mass-fluctuations for six frequencies at Mach 4·5. His numerical result (re-plotted in Fig. 7) showed that the most amplified frequency, or the frequency that has the highest amplitude ratio, is relatively high at low Reynolds number. As Reynolds number increases, the most amplified frequency decreases. This trend coincides with the boundary layer growth. If the wavelength of the most amplified mode is scaled with the boundary layer thickness, it should increase as the boundary layer grows with Reynolds number. Hence, the frequency of the most amplified mode decreases, provided that the phase velocity of the waves remains constant. Note that the modes of the waves are not distinguished in forcing theory since it applies only up to the neutral point.

An envelope may be added to the curves representing the amplitude ratio for various dimensionless frequencies in Fig. 7. The tangent point of this envelope with each particular curve represents the Reynolds number where that particular mode becomes the most amplified. Plotting the frequencies against the Reynolds number at their tangent point yields Fig. 8. This figure indicates that F_m is proportional to Re^{-n}, where $n \sim 3/4$, i.e.

$$F_m = C\left(Re^{-\frac{3}{4}}\right) \qquad \ldots(13)$$

where C is the constant of proportionality. By differentiating the above equation the following are obtained

$$dF_m = -\frac{3}{4}C\left(Re^{-\frac{7}{4}}\right)dRe \qquad \ldots(14)$$

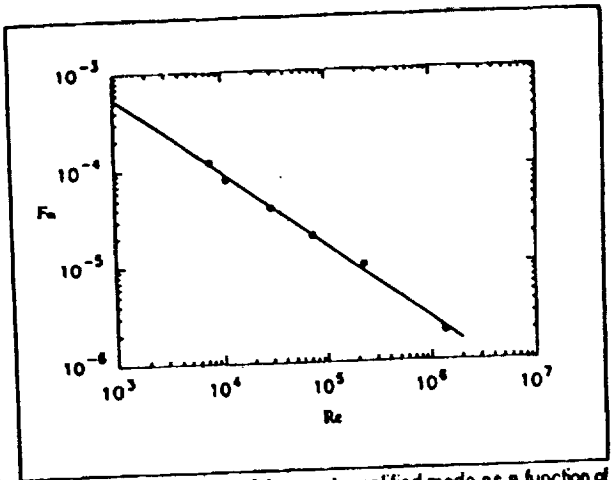

Figure 8. The frequency of the most amplified mode as a function of Reynolds number.

or

$$|dF_m| = \frac{3}{4}C\left(Re^{-\frac{7}{4}}\right)|dRe| \qquad \ldots(15)$$

It can be seen that the variation of the most amplified frequency would be very small at high Reynolds number range. Hence, a characteristic frequency may be chosen to represent the most amplified frequencies for a large Reynolds number range. For boundary layer flow at Mach 3·5, Chen *et al*[17] found that $F_m = 1{\cdot}25\times10^{-5}$. In the present work the numerical result of Mack[4] was used as a reference even though the nominal Mach number of the experiments was slightly higher than the Mach number involved in his calculation. For the Reynolds number range covered by the flat plate model, F_m was estimated to be in the order 5×10^{-6}.

The dimensionless peak frequencies of measured fluctuating pitot pressure signals, under various test conditions, are plotted in Fig. 9. These dominant frequencies in the freestream noise were at least an order of magnitude lower than the most amplified frequency predicted by linear stability theory.

Although freestream disturbances may have a strong influence on boundary layer transition, and it is a general trend that transition Reynolds number decreases with increasing freestream disturbance level[18], large freestream parameter fluctuation intensities do not always mean strong disturbances to the boundary layer instability and transition. The support of this conclusion came from Wells's[19] experimental investigation of the effect of freestream turbulence on boundary layer transition for zero pressure gradient at low speed. He compared his measurements with

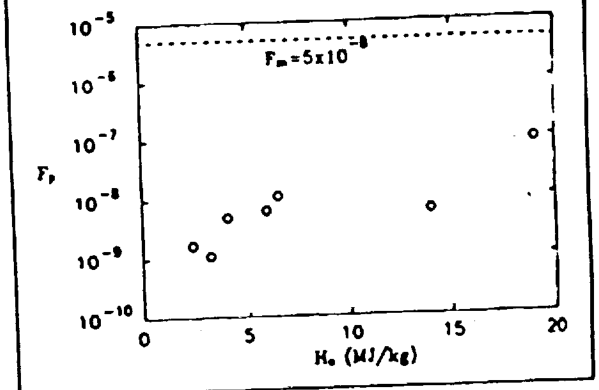

Figure 9. Plot of the nondimensionalised dominant frequency against stagnation enthalpy.

those of Schubauer and Skramstad(20) and Boltz *et al*(21) and it was found that at the same freestream velocity fluctuation intensity, the transition Reynolds number could be expected to have different values. For example, at $(\langle u'^2\rangle/u)^{0.5} = 0{\cdot}1\%$, the transition Reynolds number obtained by Wells was greater than that by Schubauer and Skramstad by nearly a factor of two. To estimate the magnitude of the freestream disturbances in regard to transition, the power spectrum of the fluctuating quantity must be examined as the waves, whose wavelengths are scaled with the boundary layer thickness, control the process of transition. In fact, Stetson and Kimmel(5) discovered experimentally that the major second mode disturbances have wavelengths approximately twice the boundary layer thickness.

If the velocity of each Tollmien-Schlichting wave is equal to the flow velocity at the boundary layer edge, then at the same frequency the wavelength of sound which travels at the speed of sound relative to the flow is not much different from the wavelength of the TS wave for hypersonic flow. Therefore, a correspondent relation between the two may be expected, as far as the growth of disturbance in the boundary layer is concerned. In the present investigation, a large percentage of freestream disturbance energy was distributed in a frequency band that had a corresponding wavelength much longer than the boundary layer thickness. It would not be favoured by the amplification process in the boundary layer of the flat plate model. Disturbances of frequencies higher than the detected maximum frequency might in fact exist in freestream. However, the contribution from these frequencies to the total disturbance energy would not be expected to be significant. Since sound wave disturbance in freestream was originated from the turbulent boundary layer of the nozzle wall, its power spectrum was closely related to that of the turbulent fluctuations in the boundary layer, which decayed rapidly with wave number.

DETECTION OF TRANSITION

Many physical quantities are sensitive to variations in the state of the boundary layer, and any of these properties may be used as a criterion for determining transition. Owen *et al*(22) defined the onset of transition as the point where the Stanton numbers first consistently exceeded the laminar value. However, even within the laminar boundary layer, the measured Stanton number may not always be consistent with the value predicted by laminar theory. Based on the fact that for a flat plate with uniform pressure, the heat transfer rate decreases with the distance from leading edge unless the laminar nature of the flow is disturbed, the transition point is defined, for the present work, as the point where the Stanton number has a minimum value.

ANALYSIS OF EXPERIMENTAL DATA

Model vibration can be a source of disturbance which would trigger instability waves in the laminar boundary layer. In the case of quiet subsonic wind tunnel tests by Pilipenko and Shapovalov(23) it was found that there existed a pronounced correlation between the Tollmien-Schlichting waves and the vibrations of the model. The vibration frequencies seemed to be synchronised with that of instability waves. It was believed that the same mechanism which induced instability waves from body vibration in subsonic boundary layer flow could drive the development of instability and transition in hypersonic flows.

Body vibration was picked up by pressure transducers mounted in the flat plate model. The frequency of the vibration was higher than the expected TS frequencies. This vibration was attributed to the stress wave travelling through the shock tunnel test section wall and the model suspension.

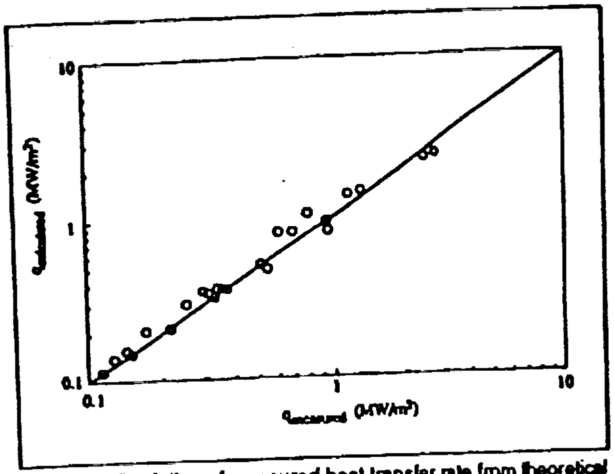

Figure 10. Deviation of measured heat transfer rate from theoretical prediction at x = 50 mm.

Shock tubes by nature create a flow which is fundamentally unsteady, and care must be taken when applying steady state analysis to the results of such experiments. During the period when uncontaminated test gas is passing over the model, the stagnation and static pressure levels are not constant but decay with time by an amount which is a function of the tunnel operating conditions. However, a region of flow exists where the ratio of pressures across the expansion nozzle is steady, and the Mach number of the flow can be considered constant. The ratio of stagnation pressure to dynamic pressure will also be constant, and for the flow field around any body shape to be steady, the locally measured static pressures must be steady when normalised with respect to stagnation pressure. Provided these pressure ratios are constant, then a small change in the overall pressure level will not cause substantial change to the overall flow field or the shape of the streamlines, and a steady state analysis may be used.

The situation for heat transfer is slightly different. For the flow to be considered steady, the Stanton number must be constant, which implies that the heat transfer must decrease in proportion to the product of the mass flow rate with the recovery enthalpy. If the test flow conditions are computed on the assumption that an isentropic expansion follows shock reflection in the stagnation region, then it can be shown that, for constant Stanton number, heat transfer must have the following relationship with stagnation pressure P_0

$$q \sim P_0^{\frac{(3\gamma-1)}{2\gamma}} \qquad \ldots(16)$$

where γ is an effective ratio of specific heats for the nozzle expansion. For a γ of 1·4, heat transfer dependents on stagnation pressure to the power of 1·14. For the purposes of determining the duration of the steady flow period, this power of 1·14 was ignored for numerical expediency, and the heat transfer rates were normalised by stagnation pressure directly. For a decay in stagnation pressure of 30% this would lead to an error of 5% in Stanton number, and does not substantially affect the conclusions drawn from the data. Reasonably steady normalised traces were obtained in the laminar flow regions even with this simplification. Figure 10 compares the measured heat transfer rates at distance of 50 mm from leading edge with calculated values using Eckert's(24) reference temperature method under different test conditions. The conditions at the beginning of the test period were selected for the calculation. The measured heat transfer rate was taken at the moment when the pressure ratio first reached the steady state. The relative errors are seen to be within ±20%. Figure 11 shows a

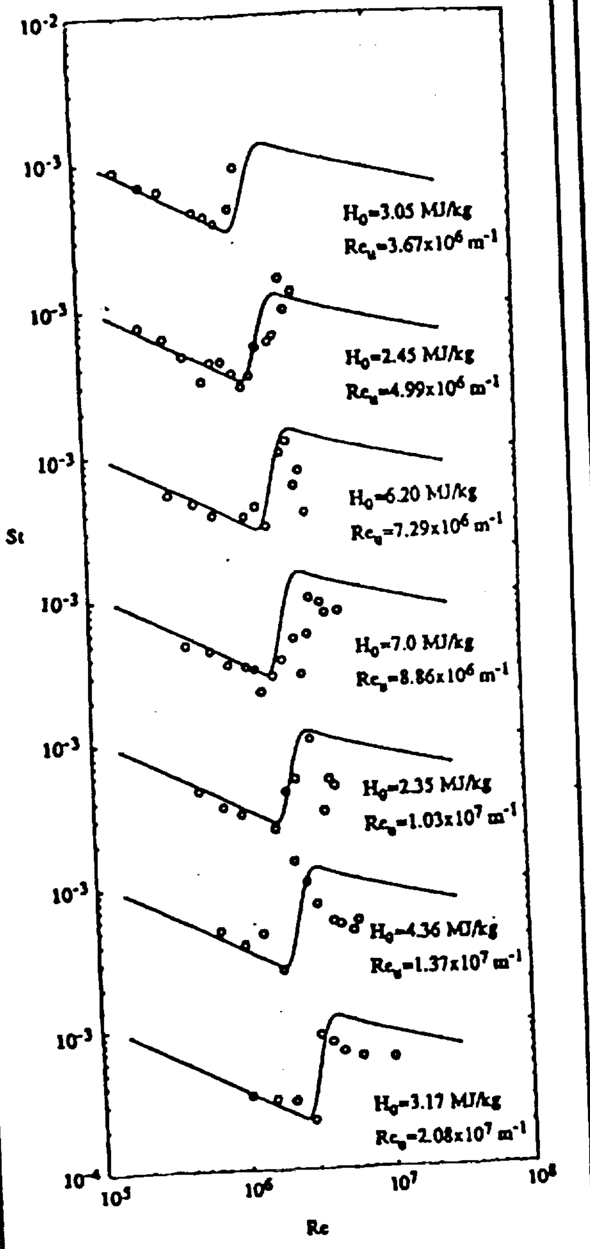

Figure 11. Heat transfer distribution along the plate at different test conditions.

group of measured heat transfer rate distributions in terms of Stanton number along the plate. The predicted turbulent heat transfer rates were obtained from Stollery and Coleman's(25) treatment of Eckert's empirical correlation. The virtual origin for the turbulent boundary layer was set at the onset of transition.

Transitional flow in boundary layers is characterised by unsteady phenomena, and cannot be described completely by either laminar or turbulent steady flow processes. However, a quasi-steady empirical approach may be used for engineering purposes to give estimates of averaged flow properties from standard laminar and turbulent flow correlations. It is based on the assumption that transitional flow may be described by alternating periods of laminar and turbulent boundary layers. An intermittency factor γ is used to indicate the balance between the two periods. Once the value of γ in the transition zone is known, an aerodynamic quantity, say Ω, can usually be approximated from its laminar and turbulent values by,

$$\Omega = (1-\gamma)\Omega_L + \gamma\Omega_T \qquad \ldots(17)$$

where Ω_L and Ω_T denote respectively the values of Ω for fully laminar and fully turbulent flows. Dhawan and Narasimha(26) used an equation of the form Equation (17) to predict skin friction coefficient in transitional boundary layers. From Reynolds analogy, a similar equation can be used for heat transfer analysis,

$$St = (1-\gamma)St_L + \gamma St_T \qquad \ldots(18)$$

In the case of subsonic and supersonic wind tunnel tests, the distribution of the intermittency factor in the transition zone can be measured with hot-wire velocimeter, or pitot probe laced close to the surface of the model. In hypersonic shock tunnel test, use of hot-wire and pitot probe in the remarkably thin boundary layer seems to be impossible. However, there is considerable evidence to suggest that transitional characteristics in hypersonic boundary layers are similar to that in subsonic boundary layers(27). Hence, theoretical or empirical correlations obtained for incompressible boundary layers were used for the calculation of γ. Abu-Ghannam and Shaw's(28) proposal of a correlation for intermittency factor in subsonic boundary layer transition reads

$$\gamma = 1 - \exp\left(-5\eta^3\right) \qquad \ldots(19)$$

The variable η is defined as

$$\eta = \frac{(Re - Re_t)}{(Re_e - Re_t)} \qquad \ldots(20)$$

It is seen from Fig. 11 that within the laminar boundary layer the Stanton number distribution closely followed the theory. After passing through a minimum point, the Stanton number increased rapidly, then fell again. The rise of the Stanton number indicates

Table 1. Flow conditions and transition result.

Diaphragm mm	H_0 MJ/kg	T K	P kPa	M	U m/s	Re_e ×10⁶	Re_t ×10⁶
1	2·45	254	3·25	6·52	2100	4·99	1·28±0·15
1	3·05	330	3·27	6·40	2330	3·67	0·88±0·07
1	4·32	476	3·25	6·14	2680	2·46	0·85±0·05
1	7·0	867	3·28	5·74	3360	1·25	0·65±0·03
2	2·35	240	5·22	6·55	2060	10·3	1·74±0·18
2	2·99	321	5·50	6·42	2310	6·42	1·40±0·12
2	4·35	500	6·40	6·11	2720	4·50	1·28±0·08
2	4·52	508	6·30	6·08	2850	3·80	1·17±0·07
2	6·40	770	5·0	5·81	3150	2·6	1·03±0·08
3	2·88	310	8·70	6·48	2200	9·56	1·63±0·17
3	4·04	470	9·61	6·15	2690	6·00	1·44±0·11
3	4·46	529	7·92	6·09	2840	4·98	1·20±0·09
3	6·03	767	8·54	5·85	3140	3·50	1·09±0·07
3	9·19	1257	9·60	5·47	3810	2·18	0·71±0·07
4	3·17	347	18·3	6·30	2380	20·8	2·81±0·37
4	4·36	496	19·2	6·12	2730	13·7	1·85±0·25
4	6·20	785	21·9	5·81	3220	7·29	1·45±0·13
4	7·40	995	20·0	5·65	3490	5·88	1·40±0·11
4	10·1	1340	23·8	5·46	4050	4·30	1·33±0·08
5	5·75	777	24·0	5·72	3146	11·3	1·75±0·09
5	7·0	1020	26·5	5·51	3444	8·86	1·51±0·07
5	8·87	1274	29·5	5·43	3771	6·84	1·28±0·07
5	16·2	2369	28·5	5·02	4797	3·10	1·08±0·06
5	19·2	2634	25·0	5·02	5141	2·40	0·92±0·05
5*	3·52	379	11·1	6·33	2510	11·3	1·75±0·09

* Argon driver gas

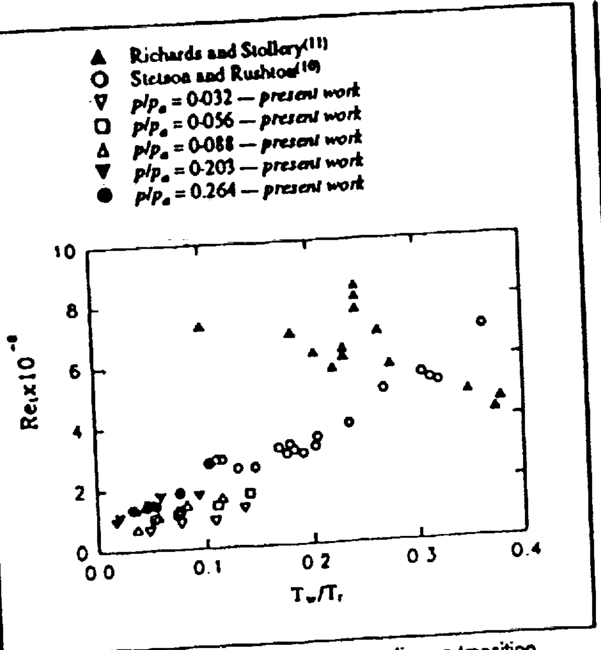

Figure 12. Effect of boundary layer cooling on transition.

the breakdown of laminar flow, resulting in the heat transfer process being assisted by turbulent mixing in an intermittent manner. The increase in Stanton number, or heat transfer rate, continued as the boundary layer flow became more and more turbulent. The establishment of a fully turbulent boundary layer was marked by a consistent decrease in Stanton number after the maximum value, albeit the shape of the experimental Stanton number profile did not follow the curve calculated using turbulent boundary layer theory. The increase of transition Reynolds number with unit Reynolds number is also depicted in Fig. 11. Another feature observed in data analysis is that the position of the transition onset point was not fixed during the test, but fluctu- ated over a wide region. Transition by its nature is unsteady, and the unit Reynolds number was not completely constant throughout the test period, so this result was not unexpected. In the present study, the uncertainty of the onset position was constrained by half of the distance between two consecutive transducers. In the turbulent boundary layer the measured heat transfer rates were smaller than predicted values. This could be attributed to chemical reactions, such as oxygen dissociation, which would reduce the recovery temperature of the boundary layer flow, although

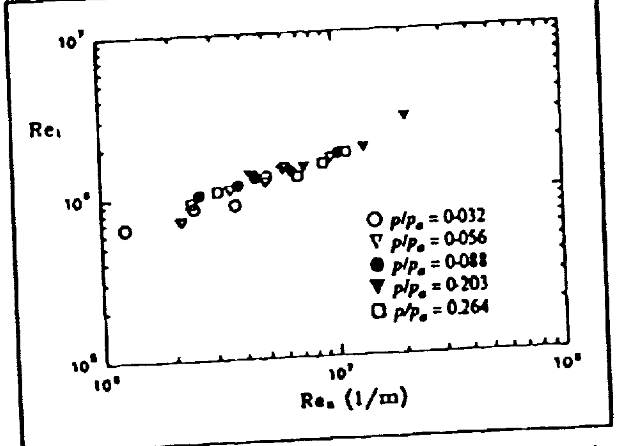

Figure 13. Transition onset Reynolds number as a function of unit Reynolds number.

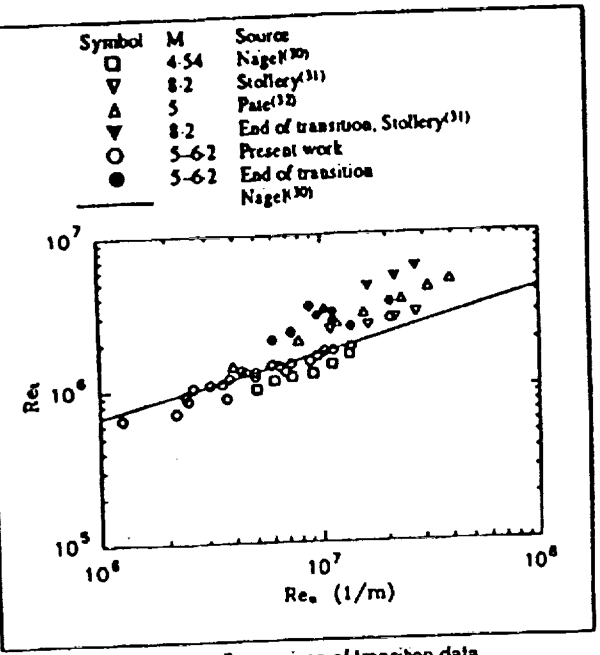

Figure 14. Comparison of transition data.

increase in heat transfer in laminar region due to recombination of dissociated oxygen has been reported for a shap cone model (Germain *et al*(29))

Transition results are listed in Table 1, along with the freestream test conditions and unit Reynolds numbers. Figure 12 displays the relation between transition Reynolds number and wall to recovery temperature ratio T_w/T_r. These data can extend Stetson and Rushton's results in the low range of wall to recovery temper- ature ratios, as well as reveal that the transition Reynolds number is pressure and enthalpy dependent. However, in the plot of Re_t vs Re_e (Fig. 13), the measured points collapsed closely on to a single curve. This implied that, as pointed out by Ross(8), the primary influence of pressure and temperature on transition is through the unit Reynolds number coupling. In both Fig. 12 and Fig. 13, the effect of Mach number was not eliminated, i.e. all the data points were plotted regardless of the Mach numbers involved in test flows. The general trend of Fig. 12 shows that transition Reynolds number decreased with wall cooling, contrary to the observation made by Cary(12) but in agreement with the results by Demetriades(9) and Stetson and Rushton(10). Another important difference between the present investigation and those of previous investigators lies in the method of wall cooling. In this experiment the variation in wall to recovery temperature ratio was achieved by changing the stagnation enthalpy of the flow while the wall temperature was maintained constant, which is the same method employed by Stetson and Rushton(10). The methods used by most other investigators were the opposite. For this reason, Stetson and Rushton's conical data were plotted in Fig 12 for comparison Figure 13 implies that there would be a simple relation between transition Reynolds number and unit Reynolds number, and this relation incorporates the effects of Mach number, pressure and wall cooling.

Following Nagel's(30) discussion, the correlation between Re_t and Re_e can be written as

$$Re_t = aRe_e^{0.4} \qquad \ldots (21)$$

where the constant a is determined through the experiment and was found to be 2687. The Re_t–Re_e relationship was compared with experimental and theoretical results of other investigators in Fig. 14. The transition zone was correlated using Dhawan and Narasimha's(26) proposal, i.e.

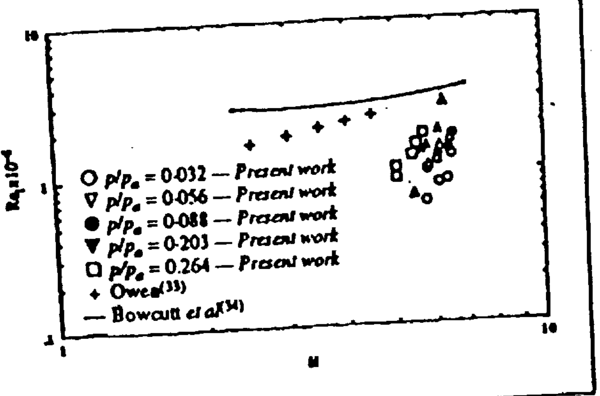

Figure 15. Variation of Re_t against M.

where c = 13·8, and was also determined through the experiment. Equations (21) and (22) are substituted into Equation (19) to calculate the intermittency factor.

$$Re_e - Re_t = cRe_t^{0.8} \qquad \ldots(22)$$

Figure 15 shows transition Reynolds number *vs* Mach number, and it became apparent that the effect of Mach number on transition was influenced by freestream pressure. Also included in this figure are Owen's(33) result and a simple correlation by Bowcutt *et al*(34) It should be pointed out that in the present investigation, all the tests were performed on the same fixed geometry nozzle, and changes in Mach number were due to the changes in chemical composition of test gas when the stagnation enthalpy was varied. Consequently, associated with this Mach number variation was the change in unit Reynolds number. Therefore, Fig. 15 should be regarded as the reflection of the effect of unit Reynolds number on transition when viewed in M–Re_t space.

CONCLUSION

The experimental investigation extended the boundary layer transition measurement to the stagnation temperature of about 9100K for flow over a flat plate. The relation between the onset transition Reynolds number and unit Reynolds number in high enthalpy hypersonic flows was shown to be similar to that in low enthalpy supersonic and hypersonic flows. The result of the present investigation showed that unit Reynolds number was the primary parameter in determining transition in hypervelocity boundary layers. Wall cooling destabilised the laminar boundary layer and caused the reduction of transition Reynolds number, which indicated that the second mode instability may retain its dominance in the transition of hypervelocity boundary layers. The experimental data was consistent with the results from other facilities, although the test flow of T4 shock tunnel contains strong disturbances with a narrow band concentration of disturbance energy. The measured heat transfer rate in laminar boundary layers agreed well with analytical predictions, whereas in turbulent boundary layer, it differed significantly from available turbulence models. Dissociations of diatomic molecules in the air test flow would have effects similar to wall cooling on boundary layer flows, i.e. they both result in the reduction of recovery temperature in the boundary layer. It could be speculated that the effects of the former on hypervelocity boundary layer transition are similar to that of the latter. Further investigations are needed to verify this speculation and to examine the effects of different modelconfigurations on hypervelocity boundary layer transition.

ACKNOWLEDGEMENTS

This work was supported by the Australian Research Council and NASA Langley Research Center under NASA contract NAGW674.

REFERENCES

1. Kendall J.M. Wind tunnel experiments relating to supersonic and hypersonic boundary-layer transition, *AIAA J*, 1975, 13, (3), pp 290-299.
2. Reshotko, E. Boundary-layer stability and transition, *Ann Rev Fluid Mech*, 1976, 8, pp 311-349.
3. Van Driest E.R. Calculations of the stability of the laminar boundary layer in a compressible fluid on a flat plate with heat transfer, *J Aero Sci*, 1952, 19, (13), pp 801-812.
4. Mack, L.M. Boundary Layer Stability Theory, AGARD, Rep no.1709, 1984.
5. Stetson, K.F. and Kimmel, R.L. On hypersonic boundary layer stability AIAA-92-0737, 30th Aerospace Sciences Meeting and Exhibit 6-9 January 1992, Reno, NV.
6. Seddougui, S.O., Bowles R.I. and Smith, F.T. Surface Cooling Effects on Compressible Boundary Layer Instability, NASA Contractor Report 182003, ICASE Report No. 9019, 1990.
7. Deem, R.E. and Murphy, J.S. Flat plate boundary layer transition at hypersonic speeds, AIAA Paper 65128, 1965.
8. Ross, R. Influence of total temperature on transition in supersonic flow, *AIAA J*, 1973, 11, (4), pp 563-565.
9. Demetriades, A. New experiments on hypersonic boundary layer stability including wall temperature effects, In: Proceedings of the 1978 Heat Transfer and Fluid Mechanics Institute, Washington. Emery A.F. and Depew C.A. (eds), Stanford University Press, 26-28 June 1968, pp 39-55.
10. Stetson, K.F. and Rushton G.H. Shock tunnel investigation of boundary-layer transition at M = 5·5, *AIAA J*, 1967, 451, (5), pp 899-906.
11. Richards, B.E. and Stollery, J.L. Further experiment on transition reversal at hypersonic speeds, *AIAA J*, 1966, 4, (12), pp 2224-2226.
12. Cary Jr, A.M. Turbulent boundary layer heat transfer and transition measurements for cold wall conditions at Mach 6, *AIAA J*, 1968, 6, (5), pp 958-959.
13. Stalker, R.J. and Morgan, R.G. The University of Queensland free piston shock tunnel T4, initial operation and preliminary calibration, In: Proceedings of 43rd Australian National Space Engineering Symposium, Adelaide, 1988.
14. Stalker, R.J. and Crane K.C.A. Driver gas contamination in a high-enthalpy reflected shock tunnel, *AIAA J*, 1978, 16, (3), pp 277-279.
15. McIntosh, M.K. Computer program for the numerical calculation of frozen and equilibrium conditions in shock tunnels, Department of Physics, Australian National University, Canberra, Australia, September 1968.
16. Lordi, J.A., Mates, R.E. and Moselle, J.R. Computer program for the numerical solution of nonequilibrium expansions of reacting gas mixtures, NASA CR 472, 1966.
17. Chen, F.J., Malik, M.R. and Beckwith, I.E. Boundary layer transition on a cone and flat plate at Mach 3·5, *AIAA J*, 1989, 27, (6), pp 687-693.
18. Pate, S.R. Effects of wind tunnel disturbances on boundary layer transition with emphasis on radiated noise: a review, 11th Aerodynamic Testing Conference, Colorado Springs, Colorado, 18-20 March 1980.
19. Wells Jr, C.S. Effects of freestream turbulence on boundary layer transition, *AIAA J*, 1967, 5,(1), pp 172-174.
20. Schubauer, G.B. and Skramstad, H.K. Laminar boundary layer oscillations and transition on a flat plate, *J Aero Sci*, 1947, 14, pp 69-76.
21. Boltz, F.W., Kenyon, G.C. and Allen, C.Q. The boundary layer transition characteristics of two bodies of revolution, a flat plate and an unswept wing in a low turbulence wind tunnel, NASA TN D309, 1960.

22. Owen, F.K. and Horstman, C.C. Comparison of wind tunnel transition and free stream disturbance measurements, *AIAA J*, 1975, 13, (3), pp 266-269.
23. Pilipenko, A.A. and Shapovalov G.K. Effect of model vibration on transition from laminar to turbulent boundary layer flow, *Fluid Mechanics-Soviet Research*, 1988, 17, (4), pp 68 -76.
24. Eckert, E.R.G. Engineering relations for skin frictions and heat transfer to surface in high velocity flow, *J Aero Sci*, 1955, 22, pp 585-587.
25. Stollery, J.L. and Coleman, G.T. A correlation between pressure and heat transfer at supersonic and hypersonic speeds, *Aeronaut Q*, 1975, 26, pp 304-315.
26. Dhawan, S. and Narasimha, R. Some properties of boundary layer flow during the transition from laminar to turbulent motion, *J Fluid Mech*, 1958, 3, pp 428-436.
27. Narasimha, R. The laminar-turbulent transition zone in the boundary layer, *Prog Aero Sci*, 22, 1985, pp 29-80.
28. Abu-Ghannam, B.J. and Shaw, R. Natural transition of boundary layers, the effects of turbulence, pressure gradient, and flow history, *J Mech Eng Sci*, 1980, 22, (5), pp 213-228.
29. Germain, P., Cummings, E., and Hornung, H., Transition on a sharp cone at high enthalpy; new measurements in the shock tunnel T5 at Galcit, 31st Aerospace Sciences Meeting and Exhibit, 11-14 January 1993, Reno, NV.
30. Nagel, A.L. Analysis of the unit reynolds number effect in hypersonic flat plate boundary layer transition, In: Proceedings of the 1968 Heat Transfer and Fluid Mechanics Institute, Amery A.F. and Depew C.A. (eds). Stanford University Press, 1968, pp 51-64.
31. Stollery, J.L. Heat transfer at hypersonic speeds — a survey of recent and current experiments in the Imperial College hypersonic gun tunnel, ARC. 29611, December 1967.
32. Pate, S.R. and Schueler, C.J. Radiated aerodynamic noise effects on boundary layer transition, *AIAA J*, 1969, 7, (3), pp 450-457.
33. Owen, F.K. Transition experiments on a flat plate at subsonic and supersonic speeds, *AIAA J*, 1970, 8, (3), pp 518-523.
34. Bowcutt, K.G., Anderson, J.D. and Capriotti, D. Viscous optimized hypersonic waveriders, AIAA Paper 87-0272, 1987.

N95- 25399

19

1995118977 47552

P- 9

The Superorbital Expansion Tube concept, experiment and analysis

A. J. NEELY and R. G. MORGAN
Department of Mechanical Engineering,
The University of Queensland, Brisbane,
Australia

ABSTRACT

In response to the need for ground testing facilities for super orbital re-entry research, a small scale facility has been set up at the University of Queensland to demonstrate the Superorbital Expansion Tube concept. This unique device is a free piston driven, triple diaphragm, impulse shock facility which uses the enthalpy multiplication mechanism of the unsteady expansion process and the addition of a secondary shock driver to further heat the driver gas. The pilot facility has been operated to produce quasi-steady test flows in air with shock velocities in excess of 13 km/s and with a usable test flow duration of the order of 15 μs. An experimental condition produced in the facility with total enthalpy of 108 MJ/kg and a total pressure of 335 MPa is reported. A simple analytical flow model which accounts for non-ideal rupture of the light tertiary diaphragm and the resulting entropy increase in the test gas is discussed. It is shown that equilibrium calculations more accurately model the unsteady expansion process than calculations assuming frozen chemistry. This is because the high enthalpy flows produced in the facility can only be achieved if the chemical energy stored in the test flow during shock heating of the test gas is partially returned to the flow during the process of unsteady expansion. Measurements of heat transfer rates to a flat plate demonstrate the usability of the test flow for aerothermodynamic testing and comparison of these rates with empirical calculations confirms the usable accuracy of the flow model.

NOTATION

a	speed of sound
d	diameter of tube
h	specific enthalpy
l	slug length
l_∞	asymptotic slug length
M_r	reflected Mach number
m_G	mass per unit area of gas
m_{D3}	mass per unit area of tertiary diaphragm
Pr	Prandtl number
q	heat transfer rate
Re	Reynolds number
T	temperature
t	time
u	velocity
W	shock density ratio
X_s	shock tube length
β	Mirels parameter
γ	ratio of specific heats
μ	dynamic viscosity
ρ	density

Subscripts

1…20	gas states
$a,b…z$	variation of gas state within flow region
e	edge of boundary layer
I	interface
r	recovery
R	reflected shock
s	shock
w	wall

1. INTRODUCTION

With the increasing interest in the design of vehicles intended to enter the atmosphere of other planets or return to the Earth's atmosphere from beyond Earth orbit, experimental facilities will be required to allow aerothermodynamic ground testing of flight vehicle concepts and components. The envelope of flight regimes for these vehicles is expanding. Recent parametric studies on missions which involve Mars entry and Earth return(1) foresee aerocapture manoeuvres involving atmospheric approach velocities of up to 14·5 km/s. It has not been possible to produce flows suitable for aerodynamic testing, at such speeds, in any existing ground based facility. Even the most capable testing facilities such as free-piston driven shock tunnels and expansion tubes are limited in the maximum flow enthalpies they can produce. In the case of reflected shock tunnels this limit is due to the high temperatures and pressures which must be contained in the stagnation region before expansion of the flow through the nozzle, and the associated energy losses through radiative cooling. The standard single stage driver expansion tube does not experience this limitation, but its performance is limited by the strength of the shock wave produced by its driver. Flow velocities up to 9·9 km/s have been achieved in a free-piston driven single-stage driver expansion tube(2).

Manuscript received 2 August 1993, revised version received 21 December 1993, accepted 13 January 1994.
Paper No. 1972.

a-2

ORIGINAL PAGE IS
OF POOR QUALITY

9

Non-reflected shock tunnels can produce shock speeds which are fast enough for superorbital studies(3). However, all the energy is added to the test gas across the shock, which produces a dissociated, ionised plasma quite unsuitable for aerodynamic testing.

The Superorbital Expansion Tube is a new hypervelocity facility designed to produce flow conditions in a variety of test gases at velocities exceeding Earth orbital velocity. It operates as a free piston driven, triple diaphragm, impulse windtunnel. It differs from the standard expansion tube layout with the addition of a secondary driver section in which the primary driver gas is used to shock heat a secondary driver gas, boosting the driver performance. A small scale Superorbital Expansion Tube facility is currently in operation at the University of Queensland(4), and is being used to investigate these hypervelocity flow regimes using both air as test gas, reported here, and carbon dioxide test gas.

Test conditions are only useful if the state of the gas in the test flow can be quantified. As well as discussing the operation and performance of the facility, this paper also outlines the equilibrium analysis used to calculate the state of the test flows used in experiments in the small scale Superorbital Expansion Tube. This analysis is also appropriate for flow calculations in a standard expansion tube or any other facility using an unsteady expansion generated from the shock induced rupture of a light diaphragm with a large pressure difference across it.

2. OPERATION OF THE SUPERORBITAL EXPANSION TUBE

The operation of the Superorbital Expansion Tube is described in Morgan and Stalker(5). It uses the phenomenon of enthalpy multiplication of the test flow through an unsteady expansion as used in the standard expansion tube, described originally by Resler and Bloxsom(6). In this process the total enthalpy of the flow is determined by the extent of the final unsteady expansion of the test gas.

The layout of the facility is shown in Fig. 1. The tunnel is driven by a helium filled, free piston driver which is used to shock heat a helium filled secondary driver section (2·111 m in length), separated from it by a heavy diaphragm (1·6 mm mild steel, 52·5 MPa burst pressure). The primary driver, designated TQ, was originally designed for use with a small scale shock tunnel. It is of limited performance as it can only produce driver gas temperatures up to 1800K. The compression tube of the primary driver has an internal diameter of 100 mm and uses a 25 kg free piston. The secondary driver, shock tube and acceleration tube sections are all of constant area (38 mm internal diameter).

The facility can be operated in two driver modes. In the first, or reflected, mode the driver gas is stagnated at the end of the secondary driver section and exhausts into the test gas contained in the shock tube section (of adjustable length, initially 3·15 m), which is separated from the secondary driver by a thin steel secondary diaphragm (0·6 mm, 12·4 MPa burst pressure). In the second or straight-through mode the thin steel secondary diaphragm is replaced with a light cellophane diaphragm (23 mm, 95 kPa burst pressure) which ruptures with the arrival of the shock. The second mode is the preferred mode of operation. Because the primary shock speed is overtailored, the reflection of the shock in the first mode would be expected to contaminate the driver gas and reduce the driver's performance. The experiments described in this work use the preferred straight-through mode of operation.

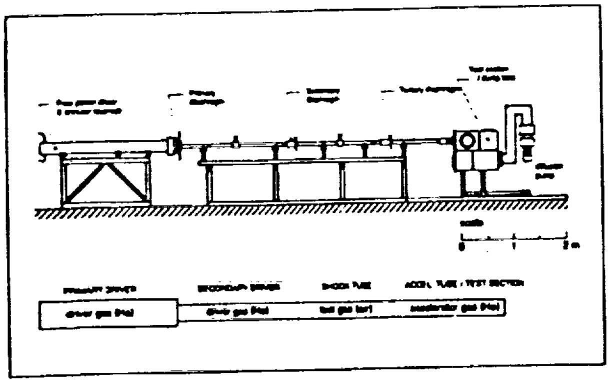

Figure 1. Layout of the small scale Superorbital Expansion Tube facility.

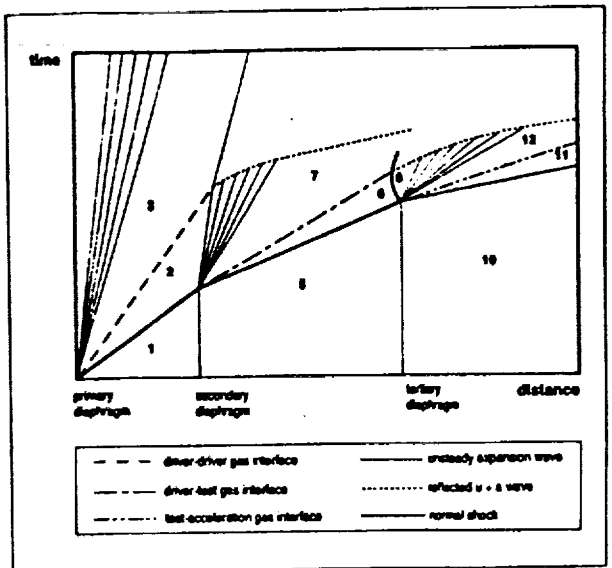

Figure 2. Wave diagram of the flow process in the Superorbital Expansion Tube.

In both modes the resulting shock wave propagates into the shock tube section and accelerates the quiescent test gas. The shock wave traverses the shock tube and ruptures the light tertiary diaphragm (9 mm grocery wrap material, 20 kPa burst pressure) and then accelerates to a higher velocity as it passes into low pressure accelerator gas (helium or air) contained in the acceleration tube (1·289 m in length, adjustable). The test gas following the shock is also further accelerated as it is expanded unsteadily into the acceleration tube. At the exit of the acceleration tube the test gas passes over the instrumented model mounted in the test section. Helium is the preferred accelerator gas as it has a low density and subsequently lower Mach number giving lower pressure and temperature ratios than air for the same shock speed.

It is the addition of the secondary driver section which, under the appropriate operating conditions, is able to boost the performance of the facility beyond that of a standard free piston driven expansion tube as reported by Neely *et al*(2). In an expansion tube, the performance of the facility, that is the flow enthalpy which can be produced, is a function of the strength of the initial incident shock wave produced by the driver. Morgan and Stalker(5) describe the performance enhancing mechanism of the secondary driver with the use of a wave diagram of the flow (Fig. 2).

The primary and secondary driver gases in regions 2 and 3 respectively, which are both helium, have the same pressure and velocity as they are separated only by a gas interface. Thus if the free piston driver is operated so that the primary shock is overtailored then the helium in region two will have the higher speed of sound. The driver gas is therefore able to drive a higher shock speed through the test gas contained in the adjacent shock tube than would be possible for a single driver arrangement where region three drives the test gas shock directly.

Flow Condition		108 MJ/Kg
secondary driver fill pressure	(kPa)	60
shock tube fill pressure	(Pa)	800
acceleration tube fill pressure	(Pa)	10
test gas		air
accelerator gas		He
shock tube length	(m)	1·625
final primary shock speed	(m/s)	6450
final secondary shock speed	(m/s)	7280
final tertiary shock speed	(m/s)	13 000

Table 1
Experimental condition

3. ESTABLISHMENT OF FLOW CONDITIONS USING AIR TEST GAS

A number of test conditions for the small scale Superorbital Expansion Tube have been established by investigating a range of filling pressures in the secondary driver, shock tube and acceleration tube sections. The highest enthalpy experimental condition produced in the facility is set out in Table 1.

For the high shock velocities produced in the shock tube (> 8 km/s) it was observed, during initial testing, that there was severe attenuation of the flow with the shock being slowed by up to 2 km/s when it reached the tertiary diaphragm. The degree of attenuation is a function of the shock velocity. To avoid the resulting decrease in performance due to this viscous flow attenuation, sections of the shock tube were removed to reduce its length (to 1·625 m) so that the secondary shock reaches the tertiary diaphragm before significant attenuation has occurred. Final tertiary shock velocities in excess of 13 km/s were achieved, for the condition described in Table 1, where a period of usable quasi-steady test flow of 15 µs duration was observed (Fig. 5).

Static pressure levels were recorded at a number of stations down the length of the three sections. These measurements were also used to calculate the shock speeds in each section. In the acceleration tube, ionisation detectors were mounted in parallel with the pressure transducers and were used to confirm the shock speeds. A typical record of wall static pressures measured in the acceleration tube is shown in Fig. 3, illustrating the development of a region of steady flow between the tertiary shock wave and the trailing expansion wave. Paull(7) proposed that it is either this expansion wave, or the reflected wave emanating from the interaction of the upstream head of the unsteady expansion with the driver-test gas interface in the shock tube, which terminates the test flow.

A standard PCB piezoelectric pressure transducer, in the configuration described by Neely *et al*(2), was initially used to measure the centreline pitot pressure levels in the test flow. Shielding was required to protect the expensive PCB transducer from fragments of the primary diaphragm which may be carried down the tube by the flow after rupture. This shielding increases the response time of the gauge, due to the filling of the cavity between the transducer and its shield, to the order of 10 µs (compared with 2 µs for unshielded operation as was observed for the flush mounted wall pressure gauges). This configuration is therefore unsuitable for the high enthalpy, short duration flows of this study. The shielded PCB was used for set up runs to determine if a suitable flow was established, in which the bar gauges described below might be used.

The bar gauge has been developed as a relatively cheap device which can therefore be placed directly in the flow without shielding. The bar gauges used were based on a design developed at the Australian National University(8) for use in the T3 free-piston driven shock tunnel. They consist of a thin piezoelectric film sandwiched between a sensing bar of aluminium and a tail of tin–lead alloy (Fig. 4). The device operates by measuring the intensity of the stress wave which propagates down the sensing bar to the piezoelectric film when the gauge is aerodynamically loaded. The material and dimensions of the tail are chosen such that the stress wave which propagates into the tail will not reflect back down its length before the period of test flow is past.

Typical wall static pressure and centreline pitot pressure histories, recorded at the exit of the acceleration tube, are shown in Fig. 5 for the high enthalpy test condition. The static pressure trace shown is from an upstream transducer as the exit transducer trace was found to be more susceptible to noise, as can be seen in Fig. 3. High frequency oscillations visible on the traces are consistent with ringing of the gauges in the mounts and were also seen in calibration tests. This behaviour is not thought to be a flow phenomenon.

Calculations indicate that the passage of the slug of accelerator gas (5 mm in length) should last less than 0·5 µs, and is therefore not resolved by the instrumentation. The traces are therefore indicative of the passage of the test gas. The calculated pressure levels for these test flows are indicated in Fig. 5 and are discussed

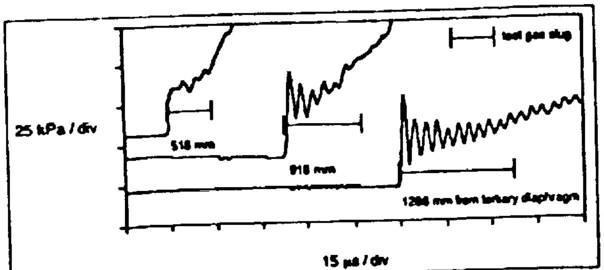

Figure 3. Acceleration tube wall static pressure histories showing calculated time for the passage of test slug (tertiary shock speed = 10·7 km/s).

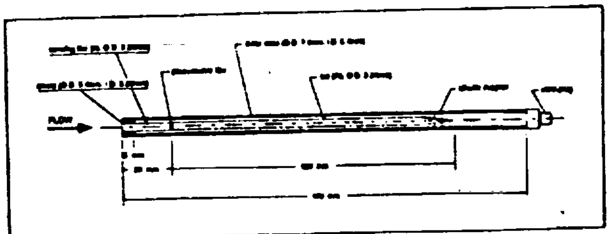

Figure 4. Detail of aluminium/lead bar gauge used to measure centreline pitot pressure.

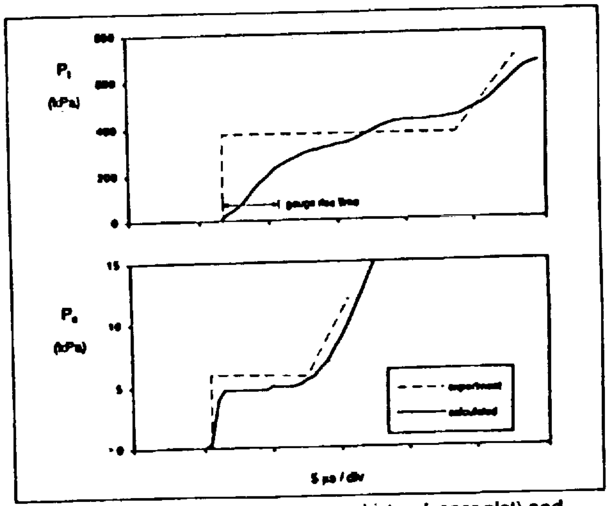

Figure 5. Centreline pitot pressure history (upper plot) and (lower) wall static pressure history for 108 MJ/kg test condition (Note: P_s measured 780 mm upstream of P_t)

in a later section. As can be seen from the pitot pressure trace, problems were experienced with the rise time of the bar gauges used to measure the pitot pressure. Calibration tests with the bar gauge flush mounted in a blanked off tube indicate a gauge rise time of 4 μs. This rise time is increased with the addition of the flow establishment time for a gauge placed in the freestream. While this is not ideal, it is adequate for resolving the region of steady flow which is observed in the static pressure traces. The bar gauges would also be expected to suffer less from temperature effects in the hot flow due to the displacement of the piezoelectric film from the sensing surface. Development of the bar gauges, which are custom made, is continuing in house, and an improved response is anticipated, which should give better definition of the limits of the test flow. It is also possible that the use of scored primary diaphragms will eliminate the problems with debris and allow the use of non shielded PCBs to measure the pitot pressure levels in the flow.

4. ANALYSIS OF TEST GAS FLOW STATES

4.1 Approach

This section covers the analysis of the processes to which the test gas alone is subjected, and leads to an estimate of the flow conditions which are achieved in the expanded core flow. No attempt is made here to model the driver flow although the perfect gas analysis from Morgan and Stalker(5) was used to help in determining the optimum driver conditions. The analysis is one-dimensional, and not fully predictive in nature, in that the experimentally measured values of the secondary and tertiary shock speeds are used. This is seen as being an essential tool for the preliminary evaluation of the experimental results.

In a parallel study(9) an axisymmetric Godunov scheme with laminar viscosity and equilibrium chemistry is being used to simulate the experiments, and is expected to add important detail to defining the extent of the usable flow in space and time.

The approach of other researchers to calculating expansion tube conditions is interesting, and can potentially be usefully applied to the current configuration to improve understanding of the complete flow conditions. Wilson(10) has performed a one-dimensional finite rate chemistry simulation with diaphragm inertia represented by a finite holding time for which the shock tube acts as a reflected shock tunnel. The code was used to simulate the conditions produced in Hypulse, the GASL expansion tube facility(11), and predicted an unexpectedly high level of dissociation in the test gas due to the strength of the reflected shock from the secondary diaphragm. Subsequent analysis by Bakos and Morgan(12) with an improved diaphragm analysis, and a criterion for the onset of chemical freezing, indicated that this level of dissociation was overestimated. As discussed below, chemical freezing of enthalpy has extra significance in the Superorbital Expansion Tube because the enthalpy multiplication effect across an unsteady expansion does not act on frozen chemical enthalpy.

Jacobs(13) performed a perfect gas axisymmetric analysis of the Hypulse facility, with viscous effects, which revealed useful information about the integrity of the contact surface, the extent and uniformity of the test flow disturbances, and departures from one dimensional flow in general. The high static enthalpies involved in the superorbital facility preclude the use of perfect gas analysis, though the usefulness of a two-dimensional code is clearly illustrated in this report.

It is seen that none of the currently available codes is able to fully predict the operation and test conditions of the superorbital flow. The analysis developed here was configured to model the dominant effects influencing the flow (i.e. viscous shock attenuation, diaphragm inertia and the unsteady expansion with near equilibrium chemistry) separately and sequentially in a way which realistically follows a sample of gas through its passage to the test section. Noting the limitations of this approach, good agreement with the experimental results was observed.

4.2 Implementation of the flow model

As stated above, the observed shock speeds in the shock and acceleration tubes are used in conjunction with the known quiescent test gas pressure to calculate the secondary and tertiary shock strengths. Real gas calculations of these conditions are made using an equilibrium analysis. The static pressure and the entropy level behind the shock are determined and these are used to determine the full gas state via an equilibrium scheme. The validity of assuming an equilibrium state is discussed later.

Calculation of the changing state of the flow through the unsteady expansion is implemented in a stepwise manner. The expansion process is divided into a large number of velocity increments (for these calculations, 100) which proceed from the calculated starting velocity of the test gas (state 8, Fig. 2) to the final velocity after expansion (state 12). This final test gas velocity is set equal to the observed tertiary shock speed as it can be shown by calculation that full Mirels(14) development of the accelerator gas slug length occurs due to its low quiescent density. Calculation across each increment is governed by the standard equation for a simple unsteady expansion wave which relates the change in static enthalpy to the change in velocity and the local speed of sound.

$$dh = -a du \qquad \ldots (1)$$

A calculation of the entropy and static enthalpy of the flow is made at the initial state eight. For equilibrium or frozen flow the expansion is isentropic. The gas condition is uniquely defined by the static enthalpy and static entropy and the *Eqstate* code(15) is used to iterate, at the end of each computed step, a solution for pressure, temperature and gas composition. The *Crek* subroutines developed by Pratt and Wormeck(16) are used to calculate the equilibrium composition at each point. These subroutines are valid for 35 ionized and unionized species in air between 300K and 24 000K. The process proceeds until the final velocity is reached, thus supplying the final state of the test gas. In this process it turns out that the determination of the initial gas state after diaphragm rupture, which then undergoes unsteady expansion, is a critical step.

The lightest possible tertiary diaphragm is used to separate the air test gas and the helium accelerator gas. Ideally this diaphragm would rupture instantaneously and, having no mass, would have no further influence on the flow. But as has been reported in previous expansion tube work(17) even the lightest diaphragm does not behave ideally resulting in two principal non-ideal effects. These are reflection of the incident secondary shock wave into the oncoming test gas and momentum loss from the expanded flow due to the energy required to accelerate the diaphragm mass after rupture. This behaviour can be observed on a more detailed wave diagram for the flow in the vicinity of the tertiary diaphragm (Fig. 6).

Operation of the facility has shown that the tertiary diaphragm material does not petal, but is sheared off around its circumference, leaving the now unattached material, whether it be solid or vapour, to travel with the flow. The subsequent motion and behaviour of the diaphragm is unclear. The strength of the reflected shock as it traverses the test gas is described well by a simple inertial model, but the values of tertiary shock speed measured could not be achieved if the diaphragm residue remains as an obstacle to the flow for more than about one tube diameter downstream. Stalker(18) has suggested that fragmentation may allow test gas to leak past the diaphragm. Independent of whatever happens to the diaphragm, the boundary conditions for the test gas across

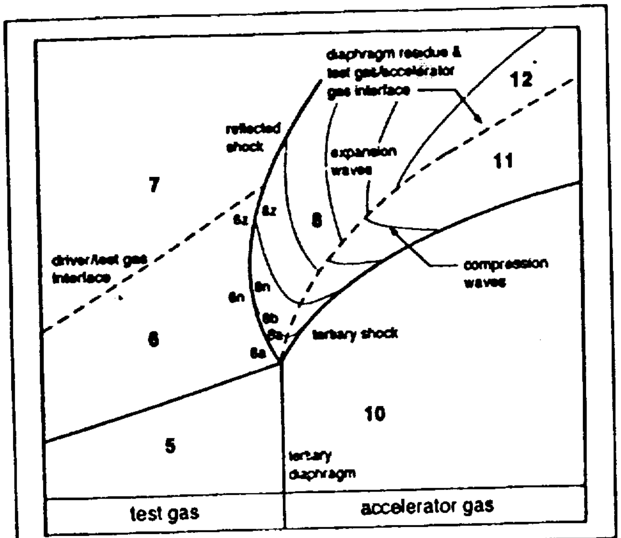

Figure 6. Wave diagram for the flow near the tertiary diaphragm.

the unsteady expansion are determined from the strength of the reflected shock and from the experimentally measured tertiary shock speed. The analysis presented here relates these boundary conditions to give a prediction of the final flow properties.

Petaling of the diaphragm may be the preferred rupture mechanism as it would anchor the material to the diaphragm station, but for such a light material it is hard to achieve. In this instance the diaphragm is impulsively loaded to two orders of magnitude above its static rupture pressure, and circumferential shearing occurs. Attempts to actively rupture the diaphragm in a controlled manner have been made(19) and continuing work on these methods is being carried out in this department.

These non-ideal diaphragm effects must be accounted for and have a significant influence on the calculation of the test gas state. The slug of shock heated test gas which arrives at the tertiary diaphragm (Fig. 6, region 6) is processed by the reflected shock wave (region 8) and there is a resulting entropy rise in the test gas which depends on the strength of the reverse shock. It then passes through the unsteady expansion which develops behind the accelerator gas–test gas interface.

The source of shock heated test gas for the expansion is non uniform. The first part of the test gas slug to arrive (region 6a), is stagnated by the shock which is reflected from the tertiary diaphragm (region 8*a*) and is then expanded from this state. Once the diaphragm ruptures though, this stagnation of the flow no longer occurs as the reflected shock is attenuated by the expansion waves (regions 8*b*...*z*), eventually to a Mach wave, and is no longer strong enough to bring the oncoming test gas to a halt. The test gas may thus be expanded from a range of initial gas states (8*a*...*z*) all of varying entropy.

Calculation of the expansion process and the resulting state of the test gas must be made for this range of starting conditions. It is perhaps easiest to consider the two bounding extremes of the starting flow. The first extreme is the initial part of the test gas slug to enter the expansion (region 8*a*) which will also become the first part of the final test flow. This region of test gas is taken as initially stationary with conditions determined behind a fully reflected shock bringing the test gas to rest. The other extreme is the terminating case (region 8*n*) which is the final part of the test gas slug to make it into region 12 before the end of the acceleration tube. The calculation of this state is less straightforward.

By tracing a particle path through the unsteady expansion, the exit point of the particle may be determined. Paull(7) set out some simple one step analytical relations for the particle path through an unsteady expansion, directly relating the entrance and exit

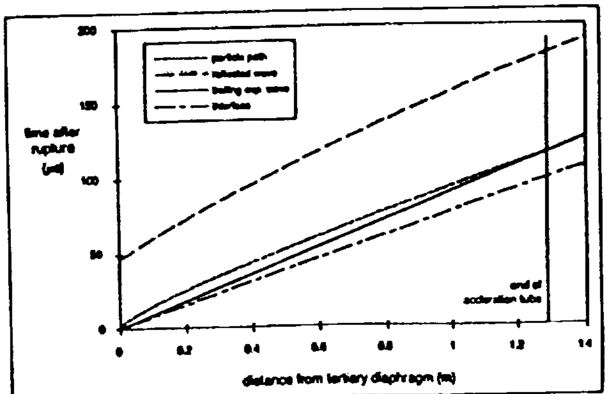

Figure 7. Tracing the terminating particle path and the reflection from the interaction of the secondary interface and the reflected shock, through the expansion for the 108 MJ/kg condition.

trajectories. Unfortunately these relations are for an ideal gas and assume a constant value of the ratio of specific heats. As the variation of γ has significant effect through the unsteady expansion, it is necessary to fully track the particle using the equilibrium scheme described earlier in this section. By adjusting the entrance time into the expansion, different particle paths may be simulated, and the appropriate one chosen.

The disturbance ($u + a$ wave) emanating from the point where the interface, separating the test gas and secondary driver gas, catches up with the attenuated reflected shock must also be tracked as it, rather than the trailing expansion wave, may terminate the test flow (Fig. 7). This occurs in a similar fashion to the process described by Paull(7) whereby the test flow is terminated by the wave emanating from the interaction between the driver–test gas interface and the leading expansion wave.

Calculation of the terminating particle paths, for the flow conditions and facility geometries described here, reveal that only a very small fraction of the shock heated test gas in region 8 reaches the final test flow and that it is the trailing expansion wave which terminates the test flow rather than the reflected wave (Fig. 7). This indicates an expected period of steady flow of 17 μs which is of the order of that observed. This also suggests the tunnel geometry described may not be the optimum configuration for the flow condition. Disregarding any further attenuation of the tertiary shock, calculation of the trajectory of the reflected wave suggests that the optimum length for the acceleration tube at this condition is 5 m. This would significantly increase the slug length of test flow and thus extend the test time to 60 μs. However, operation of the facility with longer acceleration tubes was found to cause severe attenuation of the tertiary shock speed.

To determine the point of interface catchup and the strength of the reflected shock at the beginning of the terminating particle path, it is necessary to model the behaviour of the tertiary diaphragm after rupture. Meyer(20) developed an analytical one-dimensional model for the impact of a shockwave on a movable wall such as a diaphragm, and the subsequent wave behaviour after impact. The model though is only accurate for weak incident shocks. A more appropriate analytical model has been developed for the Superorbital Expansion Tube and is described here for the strong shocks experienced in the flows considered in this study.

The residual influence of the tertiary diaphragm after rupture is represented by the inertia of the diaphragm as it is convected downstream(5) in a similar form to the action of a free piston. The mass of the ruptured diaphragm is accelerated downstream by the pressure difference across the diaphragm, the pressure behind the reflected shock being far greater than the quiescent accelerator gas pressure (initially as much as 700 000 times) and the subsequent shock heated accelerator gas pressure. As this occurs expansion waves propagate upstream from the diaphragm, eventually attenuating the reflected shock to a Mach wave. The

ORIGINAL PAGE IS
OF POOR QUALITY

accelerating diaphragm also sends compression waves downstream into the accelerator gas which quickly converge to form the tertiary shock (Fig. 6).

As the reflected shock and the diaphragm are initially in close proximity (within one tube diameter) and the sound speed behind the reflected shock is very high, it is assumed that the expansion waves emanating from the diaphragm immediately catch up with the reflected shock and that the attenuated shock pressure is immediately realised on the face of the diaphragm. Thus we have specified a region of uniform gas velocity between the reflected shock and the diaphragm remnants. The velocity of the interface, u_I, formed by the diaphragm remnants, is determined by the integration of its acceleration from rupture.

$$u_I = \left(u_I\right)_i + \Delta t \frac{\left(p_8 - p_{11}\right)}{\left(m_{D3} + m_G\right)} \qquad \ldots(2)$$

where m_{D3} is the mass of the diaphragm material per unit area and m_G is the mass of the gas per unit area which is contained between the reverse shock, S_R, and the tertiary shock, S_3.

$$m_G = \rho_8\left(x_1 - x_{S_R}\right) + \rho_{11}\left(x_{S_3} - x_1\right) \qquad \ldots(3)$$

The diaphragm velocity may then be used with the known incoming test gas velocity to determine the strength of the reverse shock at each moment(5).

$$M_R = \left(u_6 - u_{S_R}\right)\frac{\gamma + 1}{4a_6} + \left\{\frac{\left(u_6 - u_{S_R}\right)^2\left(\gamma + 1\right)^2}{16a_6^2} + 1\right\}^{\frac{1}{2}} \qquad \ldots(4)$$

As the reverse shock traverses the test gas it induces an entropy change in the gas which may be determined from the Mach number, M_R, calculated from Equation (4). The period it takes the shock to traverse the slug of test gas is small (< 15 μs) and it can be shown that only a small displacement of the diaphragm will occur in this time indicating that it is permissible to determine the reverse shock strength from the theory presented. It should also be noted that as the initial pressure loadings on the tertiary diaphragm are small (less than 1/25th of the burst pressure) there will be no significant pre-deformation of the diaphragm further suggesting one dimensional behaviour and circumferential failure of the light diaphragm material.

As this simple diaphragm analysis assumes ideal gas behaviour there will be some inaccuracy associated with its use on the high enthalpy conditions considered here. This analysis though, is only used to determine the shock strength at the beginning of the terminating particle path. The use of an adjusted value of the ratio of specific heats, which is set equal to that necessary to match the initial value of M_R calculated from Equation (4), against that required by the iterative equilibrium scheme to fully stagnate the test gas (region 8a), helps to minimise the error. It should be noted that the entropy change across the reflected shock (M_R ~ 3·6) is much less than that across the incident shock (M_R ~ 20), so that errors in this procedure are second order effects.

To calculate the velocity of the gas behind the attenuated reverse shock at the beginning of the terminating particle path (State 8*n*), the velocity immediately upstream of the shock must be determined. Although the shock heated test gas in region 6 is nominally indicated as being a region of uniform flow in Fig. 2 and Fig. 6, it is in fact a region in which there is a velocity gradient induced by viscous effects. Mirels' analysis(14) was used to determine the velocity of various points in the region and this is found to have a significant effect on the final values of pitot pressure calculated for the expanded test flow.

Mirels' theory implies that due to the viscous effects of the boundary layer growing behind the incident shock, the velocity of the gas behind the shock will approach the attenuated velocity of the shock at an asymptotic slug length determined by Equation (5) (with subscripts for the appropriate states of interest).

$$l_m = \frac{d^2}{16\beta^2}\frac{T_5}{T_6}\frac{\left(u_s - u_6\right)}{u_6}\frac{\rho_6}{\mu_5} \qquad \ldots(5)$$

A calculation of the actual slug length of test gas at the end of the shock tube is made by solving Equations (6)(14) and this is compared, for the test flow described in Table 1, to the calculated asymptotic slug length in Table 2.

$$-\frac{1}{2}\frac{X_s}{W.l_m} = \ln\left(1 - \left(\frac{l}{l_m}\right)^{\frac{1}{2}}\right) + \left(\frac{l}{l_m}\right)^{\frac{1}{2}} \qquad \ldots(6)$$

It can be seen from Table 2 that for both conditions the slug of test gas does not reach full development in the shock tube, and thus the velocity of the interface and the adjacent test gas does not reach the attenuated shock velocity. Mirels uses Equation (7) to calculate the flow non uniformity between the shock wave and the contact surface.

$$\frac{\rho_e u_e}{\left(\rho_e u_e\right)_0} = 1 - \left(\frac{l}{l_m}\right)^{\frac{1}{2}} \qquad \ldots(7)$$

If we assume that the flow density remains essentially constant, an estimate of the velocity at a distance behind the shock, which is less than the asymptotic slug length, may be made.

$$u_{6n} = u_{6w} + \left(u_s - u_{6w}\right)\left(\frac{l_n}{l_m}\right)^{\frac{1}{2}} \qquad \ldots(8)$$

This is used to determine the incoming test gas velocity adjacent to the beginning of the terminating particle path (region 8*n*). Jacobs(15) has shown numerically, using an axisymmetric Navier-Stokes code, that the rise in velocity behind the shock is essentially of the form described by Equation (8).

For the initial velocity determined in this manner, the gas velocity and gas state across the reflected shock is calculated (Table 3) and is then expanded through the unsteady expansion.

Once the starting conditions for the expansion process are determined the remnants of the diaphragm are disregarded and it is assumed they have no further effect on the flow state. The effects of the curvature and shifting of the origin of the expansion fan are essentially confined to the immediate vicinity of the tertiary diaphragm and for ease of calculation are also disregarded. The unsteady expansion is assumed to behave as a simple linear fan for the implementation of the equilibrium scheme described earlier in this section.

Test condition			108 MJ/kg
asymptotic slug length	l_m	(m)	0·280
actual slug length	l	(m)	0·073

Table 2
Test gas slug lengths at the end of the shock tube

Flow condition		108 MJ/kg	
Flow state	8	a	n
reflected Mach number		3·66	3·51
pressure	(kPa)	7672	7095
temperature	(K)	16 620	15 431
static enthalpy	(MJ/kg)	58·2	55·6
velocity	(m/s)	0	332
ratio of specific heats		1·38	1·39
gas constant	(J/kgK)	571	570
total pressure*	(MPa)	7672	7140
total enthalpy*	(MJ/kg)	58·2	55·7

* determined by isentropic stagnation

Tabla 3
Calculated flow states behind the reflected shock

Flow condition		108 MJ/kg		
calculation method		equilibrium		frozen
flow state	12	a	b	a
velocity†	(m/s)	13 000	13 000	13 000
pressure	(Pa)	6028	5768	30
temperature	(K)	5976	5918	174
density	$\times 10^{-2}$(kg/m^3)	0·222	0·218	0·030
static enthalpy	(MJ/kg)	23·6	22·8	28·9
Mach number		6·57	6·66	29·0
gas constant	(J/kgK)	454	448	571
ratio of specific heats		1·43	1·43	1·64
pitot pressure	(kPa)	375	368	51
total pressure*	(MPa)	286·8	335·4	—
dissociation fractions N		0·65	0·62	1·00
O		1·00	1·00	1·00

†equal to measured tertiary shock speed
*determined by isentropic stagnation

Table 4
Final test flow states calculated using equilibrium and frozen theory

The two starting conditions set out in Table 3 are used to calculate the limits of the range of test gas flows produced at the end of the unsteady expansion. The calculated gas states of the test flow (region 12) at the end of the acceleration tube, are set out in Table 4.

The resulting calculation of static pressure and pitot pressure levels for each starting condition can also be seen in Figs 5a and 5b, superimposed on those pressures measured in the experimental flow. Examination of the flow states before (Table 3) and after expansion (Table 4) indicate a decrease in the static pressure of the test gas compressed by the reflected shock due to the attenuation of the shock after diaphragm rupture. A slight downward pressure gradient in time remains after expansion to the final flow state. It may be seen from Fig. 5 that although the overall levels of predicted pressures are close to observed values, the experimental static and pitot pressure levels appear to increase slightly through the test flow.

Although the analysis included viscous effects behind the secondary shock, the expansion to the tertiary shock speed was performed using inviscid theory. It is thought that boundary layer growth in the expanded test gas (region 12) may be causing the noted discrepancy. A calculation of the displacement thickness of a laminar air boundary layer at the end of the test gas slug (0·97 mm for the 108 MJ/kg condition) indicates a contraction of the flow core sufficient to produce a net pressure rise in the test flow. The analysis of Akman and Morgan(9) is targeting this specific problem.

It is interesting to compare the final flow states calculated by modelling the expansion as an equilibrium process with calculations made assuming a frozen expansion process. Calculations of the expanded state of the test gas, required to match the observed final velocity, were made for a frozen expansion by fixing the chemical state of the test gas after processing by the reflected shock (state 8). The resulting expanded frozen states are also set out in Table 4.

The high dissociation fractions of the nitrogen component of the air for the frozen cases indicate that large amounts of chemical energy are stored in the flow after shock heating in the shock tube section. It can be seen that the resulting temperatures, static pressures and pitot pressures of the expanded frozen test gas are unrealistically low giving support to the assumption of an approximately equilibrium process occurring through the unsteady expansion. To achieve the high enthalpy flow conditions produced by the Superorbital Expansion Tube in experiments, the flow energy used to dissociate the test gas when it is shock heated in the shock tube must be at least partially restored to the flow through recombination of the test gas through the unsteady expansion. If this energy remained frozen as chemical energy the observed test conditions could not be achieved. It can be seen that allowing the expansion to proceed in an equilibrium manner results in significant recombination of the nitrogen component.

In the Superorbital Expansion Tube, as in all facilities which use the unsteady expansion process, the total enthalpy is not fixed at any point in the flow as it is in shock tunnel facilities. Rather, the Superorbital Expansion Tube relies on the enthalpy multiplication mechanism of the unsteady expansion and thus any increase in energy due to recombination through the unsteady expansion will be multiplied by the expansion to produce the elevated final enthalpies recorded. This is one of the main advantages which expansion tubes have over more conventional shock tube facilities in producing high enthalpy flows.

It should be noted that in reality, the chemical reactions occurring through the unsteady expansion do so in such short distances and times that finite rate chemical kinetics would come in to play. This is especially true for the beginning of the test slug where the test gas traverses the expansion wave near its origin and thus experiences the highest rate of expansion. The equilibrium model described here, though, allows a straightforward calculation giving a useful indication of the final flow states, without having to consider the complexities of finite rate chemical kinetics. It is planned that future development of this model will include some accounting for these chemical kinetics via the approximate scheme described by Bakos and Morgan(12).

5. HEAT TRANSFER RATE MEASUREMENTS TO A FLAT PLATE

As a demonstration of the usability of the superorbital velocity flow produced in the facility for aerothermodynamic testing, experiments in the test flow were conducted to measure heat transfer rates to a flat plate for the 108 MJ/kg condition. The flat plate, 65 mm in length and 25 mm wide, was mounted along the centreline of the acceleration tube exit at zero incidence to the flow (Fig. 8). It was instrumented with six platinum–quartz thin film resistance thermometers, flush mounted along the surface at 8 mm intervals beginning 13·2 mm from the leading edge. Although the duration of the test flow is brief there are sufficient model lengths of test gas in the test slug to establish steady flow over the model and a typical unsmoothed integrated heat transfer rate history illustrating the essentially steady nature of the test flow over the flat plate is shown in Fig. 9.

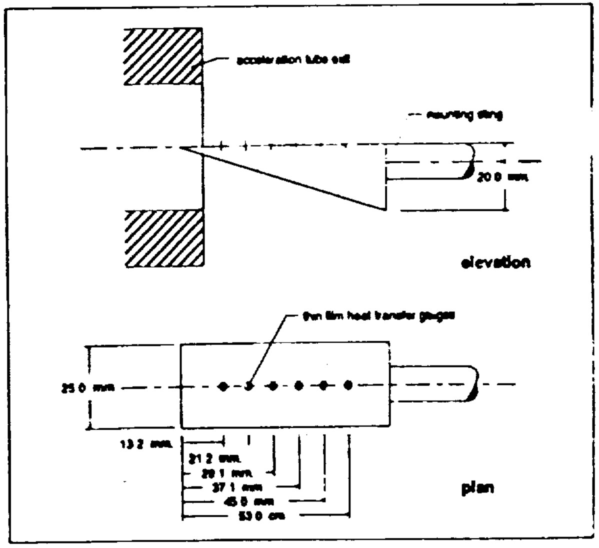

Figure 8. Flat plate geometry for heat transfer rate experiments.

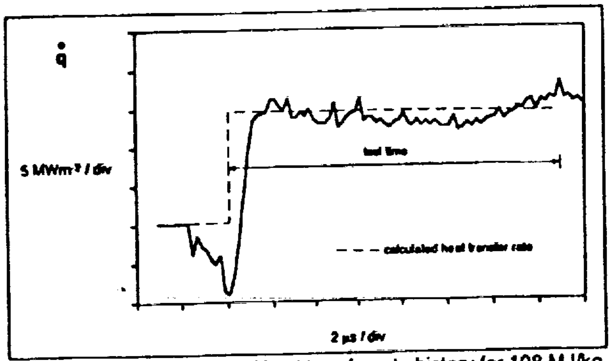

Figure 9. Typical integrated heat transfer rate history for 108 MJ/kg condition, measured 13·2 mm from the leading edge.

As local Reynolds numbers for the flow over the flat plate were below 5 × 10⁶, calculations of the expected heat transfer rates for a laminar boundary layer were made using Eckert's empirical reference enthalpy method(21).

$$\dot{q}_w = 0{\cdot}332\rho^* u_e \Pr^{-\frac{2}{3}} \mathrm{Re}^{*-\frac{1}{2}} (h_r - h_w) \qquad \ldots(9)$$

The starred values are evaluated at a reference enthalpy defined by.

$$h^* = 0{\cdot}5(h_e + h_w) + 0{\cdot}22(h_r + h_e) \qquad \ldots(10)$$

The calculated test flow state, set out in Table 4, was used to calculate conditions at the edge of the boundary layer and at the surface of the flat plate using a pressure distribution determined by the weak interaction principle for a cold wall(22), which is appropriate for the geometry and flow state in question. These in turn were used to calculate the heat transfer rate to the flat plate. The calculated rates are compared in Fig. 10 with the surface temperature histories which were integrated, in the manner of Schultz and Jones(23), to obtain the heat transfer rates.

For laminar boundary layers with similar profiles, the coefficients in Equation (9) are all constant except for the local Reynolds number. In Fig. 10 the Stanton number is normalised by $x^{-0.5}$ which is proportional to $\dot{q}/\mathrm{Re}^{*-0.5}$, and the steady level when plotted against the wetted length is seen to be constant, indicating laminar flow. The level is also seen to be in agreement with Eckert's empirical correlation. This is an interesting result as the correlations are unproven at these flow velocities and would not be expected to account for high enthalpy heat transfer mechanisms such as radiative heating which increase in significance at the elevated temperatures encountered here.

Dips in the surface temperature traces at the arrival of the shock, as can be seen in Fig. 9, were evident on many of the experimental traces. He(24) observed similar dips in his flat plate experiments and postulates that they may be due to a decrease in resistance across the gauge due to conduction through the ionised boundary layer flow. For a uniform test flow the initial resistance change due to this conduction is large with the starting of the surface flow and results in a decrease in the recorded voltage. The surface flow quickly becomes steady and the subsequent voltage increase is due only to the increasing surface temperature. He suggests that a simple first order correction may be made by effectively shifting the origin of the heat transfer rate trace to the base of the dip. This would increase the measured heating rates to a level greater than the laminar calculation predicts.

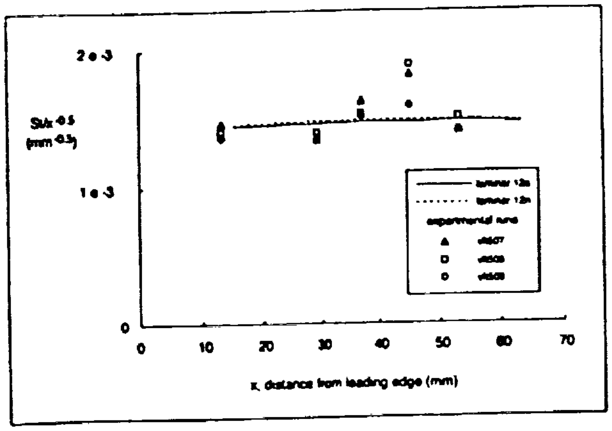

Figure 10. Plot of St normalised by $x^{-0.5}$ versus distance from leading edge for 108 MJ/kg.

The correlation of the empirical calculations and the integrated measurements is good, indicating that the method of determining the final test flow states described above is effective and that a useful core of test gas at superorbital velocity has been created in the facility.

6. CONCLUSIONS

The combination of an added secondary driver section to further shock heat the driver gas and the enthalpy multiplication effect of the unsteady expansion of the test gas allow the unique Superorbital Expansion Tube facility to produce flows at superorbital velocities, without the dissociation problems experienced by conventional shock tubes at these speeds. The small scale facility used to investigate the concept has been operated to produce quasi-steady test flows with shock velocities in excess of 13 km/s and with a duration of usable test flow of approximately 15 ~~ms~~ μs. Such high enthalpy flows are of importance in the design of any vehicle used to operate within a planetary atmosphere at velocities exceeding Earth orbital velocity, such as in proposed missions returning to Earth from Mars. No other existing ground based test facility can produce test flows at these velocities, with gas composition suitable for aerodynamic testing.

Consideration of the effects of boundary layer growth and non ideal diaphragm rupture on the flow have allowed a better understanding of the dominant flow mechanisms and enabled more accurate matching of calculated and observed test flow states. In particular account has been taken of the increase in the entropy of the test gas associated with the shock reflection at the tertiary diaphragm and the resulting non uniformity of the test gas slug in the shock tube.

It has also been shown that much better agreement with experiment is achieved if the unsteady expansion is modelled as an equilibrium process rather than as a frozen chemistry process, as the high enthalpies produced by the facility are not possible unless some of the chemical energy stored in the flow after shock heating of the test gas is returned to the flow during the unsteady expansion process.

Heat transfer rate measurements to a flat plate at zero incidence in the superorbital flow were of the same level as those predicted by Eckert's empirical correlations for laminar flow. These results show that the test flow produced by the facility can be used for meaningful aerothermodynamic research and further confirm that the analytical method of determining the final test flow states is both reasonable and useful.

These initial results have demonstrated the viability of the Superorbital Expansion Tube concept and while further testing on the small scale facility will continue, work is now proceeding on the design of larger scale facilities. It is foreseen that such facilities will be invaluable for the basic aerothermodynamic research required for future interplanetary missions involving atmospheric manoeuvring as well as for the design and testing of vehicles to be used on such missions.

ACKNOWLEDGEMENTS

The authors gratefully acknowledge the financial support of the Australian Research Council for this work.

REFERENCES

1. Lyne, J.E., Tauber, M.E. and Braun, R.D. Parametric study of manned aerocapture Part I: Earth return from Mars, *J Spacecr Rockets*, November-December 1992, 29, (6), pp 808-813.
2. Neely, A.J., Stalker, R.J. and Paull, A. High enthalpy, hypervelocity flows of air and argon in an expansion tube, *Aeronaut J*, June/July 1991, 95, (946), pp 175-186.
3. Sharma, S.P. and Park, C. Operating characteristics of a 60- and 10 cm electric arc-driven shock tube — Part II: The driven section, *J Thermophysics*, July 1990, 4, (3), pp 266-272.
4. Neely, A.J. and Morgan, R.G. Flow measurements and calibration of a superorbital expansion tube , 11th Australasian Fluid Mechanics Conference, Hobart , December 1992.
5. Morgan, R.G. and Stalker, R.J. Double diaphragm driven free piston expansion tube. *Shock waves*: Proceedings of the 18th International Symposium on Shock Waves, Sendai 1991, Springer-Verlag.
6. Resler, E.L. and Bloxsom, D.E. Very high Mach number flows by unsteady flow principles,Cornell University Graduate School of Aeronautical Engineering limited distribution monograph, 1952.
7. Paull, A. Theoretical Analysis of Test Conditions in an Expansion Tube, Department of Mechanical Engineering report, 1989, The University of Queensland.
8. Mudford, N.R., Stalker, R.J. and Shields, I. Hypersonic nozzles, *Aeronaut Q*, May 1980, p 128.
9. Akman, N. and Morgan, R.G. Numerical simulation of viscous flow in a superorbital expansion tube, 19 ISSW, Marseille 1993.
10. Wilson, G.J. Time dependent quasi-one dimensional simulations of high enthalpy pulse facilities, AIAA 4th International Aerospace Planes Conference, 1–4 December 1992, Orlando Florida.
11. Tamagno, J. Hypervelocity real gas capabilities of GASL's expansion tube (Hypulse) facility, AIAA Paper 90-1390, June 1990.
12. Bakos, R.J. and Morgan, R.G. Chemical recombination in an expansion tube with an inertial secondary diaphragm rupture model, submitted to *AIAA J*, May 1993.
13. Jacobs, P. J. Numerical Simulation of Transient Hypervelocity Flow in an Expansion Tube, ICASE interim report 120, NASA contractor report 189601, January 1992.
14. Mirels, H. Test time in low-pressure shock tubes, *Physics Fluids*, 1963, 6, (9).
15. Rizkalla, O. Eqstate: program to calculate the equilibrium or frozen properties of a supersonic gas flow at the static and stagnation points upstream and downstream of a shock wave, General Applied Science Laboratories, New York, 1990.
16. Pratt, D.T. and Wormeck, J.J. Crek: A Computer Program for Calculation of Combustion Reaction Equilibrium and Kinetics in Laminar or Turbulent Flows. Report WSU-ME-TEL-76-1, 1976, Washington State University.
17. Shinn, J.L. and Miller, C.G. Experimental perfect-gas study of expansion-tube flow characteristics. NASA Technical Paper 1317, 1978.
18. Stalker, R.J. private communication, 1993.
19. Jones, J.J. Some performance characteristics of the LRC 3 3/4-inch pilot expansion tube using an unheated hydrogen driver, Fourth Hypervelocity Techniques Symposium, Tullahoma, Tennessee, November 1965.
20. Meyer, R.F. The impact of a shock wave on a movable wall, *J Fluid Mech*, 1957, 3, (3), pp 309-323.
21. Eckert, E.R.G. Engineering relations for friction and heat transfer to surfaces in high velocity flow, *J Aeronaut Sci*, August 1955, pp 585-587.
22. Anderson, J.D. *Hypersonic and High Temperature Gas Dynamics*, McGraw-Hill, New York, 1989.
23. Schultz, D.L. and Jones, T.V. Heat Transfer measurements in short duration hypersonic facilities, AGARDograph No. 165, February 1973.
24. He, Y. PhD thesis, Department of Mechanical Engineering, The University of Queensland, 1992.

Presented at 19th International Symposium on Shock Waves, [illegible]

N95-25400

5-35

45353

1995118980

p. 6

Balances for the Measurement of Multiple Components of Force in Flows of a Millisecond Duration

D.J. Mee[1], W.J. Daniel[2], S.L. Tuttle[3] and J.M. Simmons[4]
Department of Mechanical Engineering, The University of Queensland, AUSTRALIA

Abstract. This paper reports a new balance for the measurement of three components of force - lift, drag and pitching moment - in impulsively starting flows which have a duration of about one millisecond. The basics of the design of the balance are presented and results of tests on a 15° semi-angle cone set at incidence in the T4 shock tunnel are compared with predictions. These results indicate that the prototype balance performs well for a 1.9 kg, 220 mm long model. Also presented are results from initial bench tests of another application of the deconvolution force balance to the measurement of thrust produced by a 2D scramjet nozzle.

Key words: Force measurement, shock tunnel, instrumentation

1. Introduction

The measurement of forces on vehicles flying at hypervelocity conditions has been restricted by the short durations for which current experimental facilities can sustain a representative flow. Progress has been made recently in designing balances for use in flows of duration as short as a few milliseconds (Jessen and Gronig 1993; Naumann et al. 1993; Carbonaro 1993). A new technique for measuring a single force component, the deconvolution drag balance, has been developed recently at The University of Queensland (Sanderson and Simmons 1991). This technique involves interpreting transient signals from strain gauges on a long sting connected to the test model to determine the time-history of the drag loading. The deconvolution drag balance has been applied to quite large and complex shapes in flows of duration as short as 1 ms (Porter et al. 1993).

In this paper the deconvolution force balance is extended to the simultaneous measurement of lift, drag and pitching moment. The basic design of this balance is considered and the installation of a prototype balance for measurements with a 15° semi-angle cone is discussed. Results for this model at small angles of incidence in a Mach 5 flow of nitrogen are then presented. A further application of the deconvolution balance to thrust measurement on a two-dimensional scramjet nozzle is also discussed.

2. The three-component balance design

The three-component deconvolution force balance consists of a single, 2 m long sting attached to the test model by four short bars (Fig. 1). Each of the short bars is instrumented for measurement of axial strain at its mid-point. A strain gauge bridge is

---

[1] Queen Elizabeth II Research Fellow

[2] Lecturer

[3] Postgraduate Student

[4] Dean of Engineering

also attached to the sting 200 mm from the model/sting junction. Combinations of the strain signals from the four bars are used to produce two output signals - one responding primarily to a lift input signal and the other responding primarily to a pitching moment input signal. The strain measurement in the sting responds primarily to a drag input. Inevitably there is some coupling amongst these output signals.

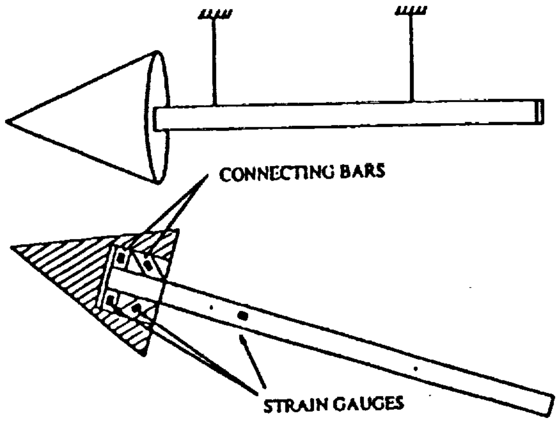

Fig. 1 Schematic of the three-component balance arrangement.

The time histories of the three outputs related to lift, drag and moment, $y_L(t)$, $y_D(t)$ and $y_M(t)$, can be related to the time-histories of the lift force, drag force and pitching moment on the model, $u_L(t)$, $u_D(t)$ and $u_M(t)$ via nine impulse response functions. This coupled convolution problem can be written in matrix notation as in Mee et al. (1992)

$$\begin{pmatrix} y_L \\ y_D \\ y_M \end{pmatrix} = \begin{pmatrix} G_{LL} & G_{LD} & G_{LM} \\ G_{DL} & G_{DD} & G_{DM} \\ G_{ML} & G_{MD} & G_{MM} \end{pmatrix} \begin{pmatrix} u_L \\ u_D \\ u_M \end{pmatrix} \qquad 1$$

where the y vectors are formed from the discretized output signals and the u vectors are formed form the applied load time histories. The square G matrices are formed from the impulse response functions, G_{ij} being the impulse response for the y_i output to a u_j input. If there is no coupling amongst the outputs then the off-diagonal submatrices in the impulse response matrix will be null. Further details on the design of the force balance are given in Mee et al. (1992).

The nine impulse response matrices were found from a series of bench tests in which a weight was attached to the model by a fine wire. The wire was cut, thus producing a step change in the load applied to the model. The output signals resulting from such a load change were recorded and processed to produce the impulse responses. The linearity of the system enables the responses to flow-type loading distributions to be determined by superposition of the results of several tests for single loads applied at various locations on the model.

In experiments in the shock tunnel, each of the y_i outputs was measured and time domain, coupled deconvolution techniques were used to determine the time histories of the lift and drag forces and pitching moment on the model. The experimentally determined impulse response functions were used for this deconvolution.

3. Tests of a prototype balance

The prototype balance was installed in a 220 mm long, 15° semi-angle, aluminium cone as indicated in Fig. 2. The cone mass was 1.94 kg. The device was first tested outside the tunnel by cutting wires attaching weights to the model. Results for a single lift load applied to the cone were compared with the results for a distributed loading which gave the same net lift force and centre of pressure. These tests indicated that the balance was not very sensitive to the distribution of load on the model.

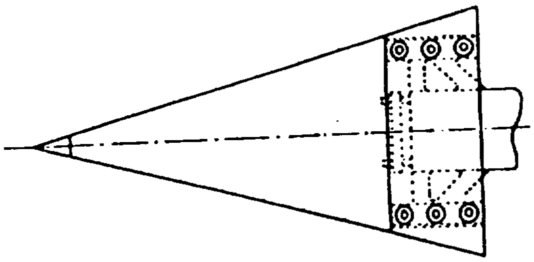

Fig. 2 Details of the connection of the balance to the sting.

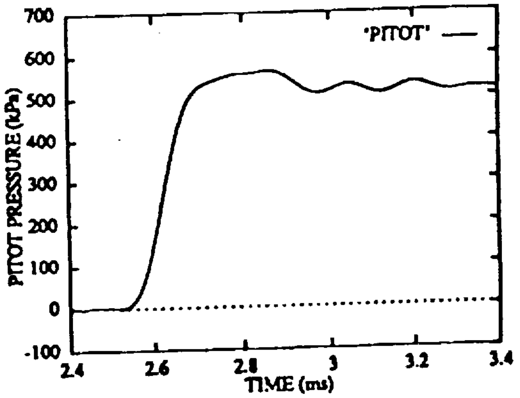

Fig. 3 Typical Pitot pressure trace for present tests.

Experiments were performed in the T4 free-piston shock tunnel (Stalker and Morgan 1988) to test the performance of the balance. The sting was supported by fine wires (Fig. 1), thus allowing it to move freely in the plane of the lift force, and was shielded from the flow so that the only aerodynamic forces were on the surface of the cone. For these tests the cone was set at three angles of attack - 0.0°, 2.5° and 5.0°.

For the tests nitrogen, at the conditions given in Table 1, was used. A typical, filtered trace of Pitot pressure during a shot of the tunnel is given in Fig. 3. Note that the zero on this and subsequent time scales is arbitrary. The Pitot trace shows a small initial overshoot which is attributed to the nozzle starting process. The mean level settles to a steady value about 500 μs after the flow starts.

It takes about 800 μs for plane stress waves initiated by the arrival of the test gas to traverse the 2 m long steel sting, reflect from the free end and return to the strain measurement locations. During this time the flow has traversed approximately 15 model lengths. The deconvolution of the measured signals continues beyond this point but the accuracies of the impulse responses at these larger times deteriorates.

Examples of the raw voltage signals obtained from the five strain gauge bridges are shown in Fig. 4. These data are from the test at 2.5°. Results are shown for the strains measured in the two inclined and the two transverse bars joining the model to the sting and for the strain measured in the sting itself. The signal-to-noise ratio is found to be adequate using semiconductor strain gauges. The relatively large oscillations in the signals in the transverse bars are associated with the dynamics of the model/sting configuration.

Table 1 Nominal test conditions - test gas is nitrogen.

Supply Enthalpy MJ/kg	Supply Pressure MPa	Static Temperature K	Static Pressure kPa	Static Density kg/m³	Flow Speed m/s	Mach Number
10.7	34.2	1370	11.4	0.0281	4270	5.8

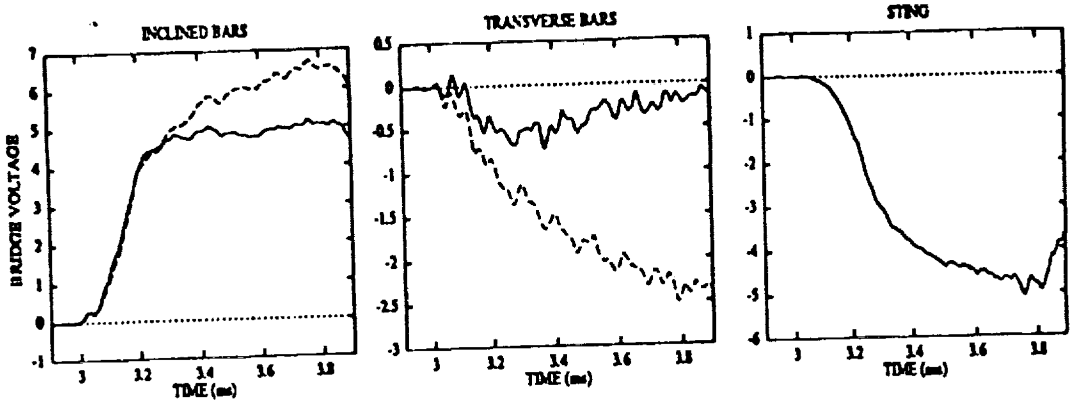

Fig. 4 Raw strain signals from the five bridges for test at 2.5° incidence.

Deconvolved signals are shown in Fig. 5 for the three incidences of the present tests. The deconvolution process leads to amplification of noise on signals and the results shown have been passed through an 8-pole Butterworth filter with a cut-off frequency of 6 kHz. The drag signals show an initial overshoot during the nozzle starting time, however the lift signals, which have a slower response, do not show this overshoot. Both lift and drag show reasonably steady values during the test time of 500 - 800 µs after flow start. The moment signal for the model is defined to be zero when the lift force acts through a point one-third of the cone axial length from the base of the cone - the theoretical line of action of the lift force for an inviscid conical flow. The results indicate that the centre of pressure during the test time is about 5 mm (2% of the cone height) further downstream of this point.

The measured results have been compared with the computed data of Jones (1969). There is a small difference in the ratio of specific heats (1.4 in Jones 1969 and 1.32 in the experiments) but a comparison of the results, shown in Table 2, gives an indication of the performance of the balance. There are some uncertainties in the conditions of the flow in the test section which, for example, will lead to an uncertainty in theoretical drag of ± 12% (Mee 1993). The absolute values for lift and drag are about 10% lower in the experiments but the ratios of lift to drag agree well. At this stage the accuracy of the balance has not been quantified.

5. Thrust measurement on a 2D scramjet nozzle

The deconvolution force balance is also being used to measure thrust produced by a symmetrically divergent nozzle with 11° ramp walls. The area ratio is approximately

5.5. Attached to the nozzle are two long stings in which the measurement of tensile strain will be used to find the nozzle's net axial thrust. The system is shown in Fig. 6.

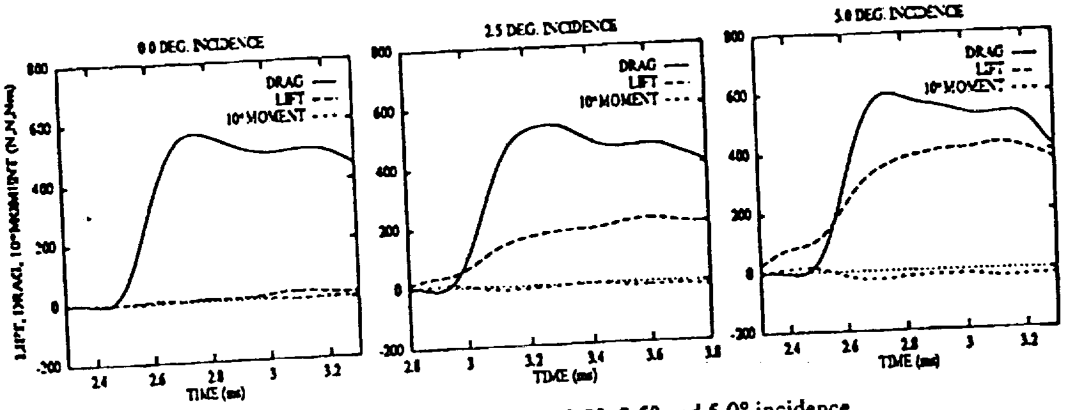

Fig. 5 Deconvolved lift, drag and moment signals for 0.0°, 2.5° and 5.0° incidence.

Table 2 Comparison of experimental results with computations of Jones (1969)

Test No.	Incidence (deg.)	Experiment Drag, D (N)	Experiment Lift, L (N)	Experiment L/D	Computation Drag, D (N)	Computation Lift, L (N)	Computation L/D
3745	0.0	510	20	0.04	550	0	0.00
3752	2.5	460	210	0.46	530	220	0.42
3748	5.0	520	420	0.81	590	470	0.80

The stings are twisted through 90° near to the nozzle to provide rigidity and bending stiffness. Finite element modelling has shown this to be acceptable. There are strain gauges before and after the twist on each sting. The static pressure along the ramp walls and the Pitot pressure across the nozzle's exit plane will be measured in the experiments. Any difference between the thrust indicated by the pressures and that determined with the deconvolution balance will be due to skin friction.

The strains from a finite element simulation for a tunnel-type loading have been deconvolved successfully using an impulse response based on another finite element computation. The model has been manufactured and instrumented and bench testing shows encouraging agreement with the computations (Fig. 7). Differences between the step responses after arrival of reflected waves are attributed to different end conditions for the experiment and the computation. Based on these results and previous experience with deconvolution balances it is expected that the present balance will perform satisfactorily in tests in T4.

6. Conclusions

The results of tests using a three-component deconvolution force balance have indicated that the balance performs satisfactorily in a shock tunnel flow of a millisecond duration. The balance performed well on a model that was not restrictively small or light - the model was 220 mm long and had a mass of 1.9 kg. Further testing is required to quantify the accuracy of the balance.

Acknowledgement

The authors are grateful for the support received from the Australian Research Council under grant AE9032029 and the Queen Elizabeth II Fellowship Scheme (for DJ Mee).

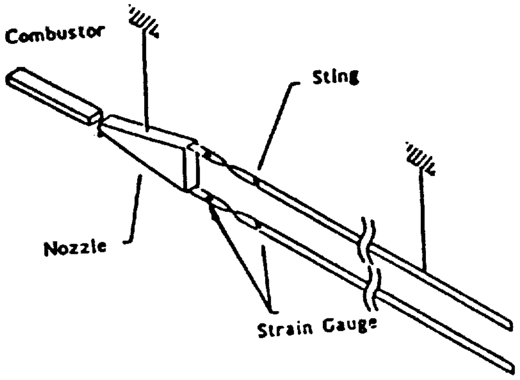

Fig. 6 Schematic of the thrust balance.

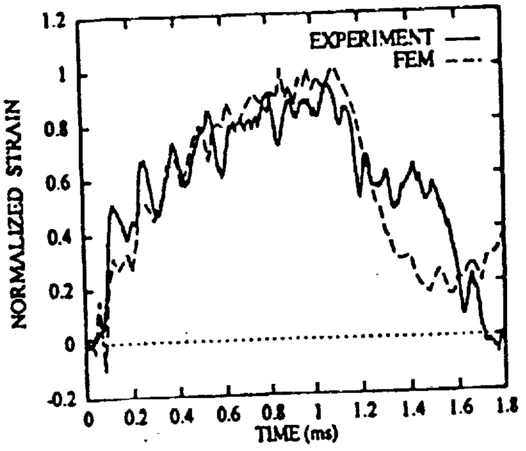

Fig. 7 Experimental and computed step responses for a point load on the nozzle.

References

Carbonaro M (1993) Aerodynamic force measurements in the VKI longshot hypersonic facility. In: Boutier A (ed) New trends in instrumentation for hypersonic research. Kluwer, Dordrecht, pp 317-325

Jessen C, Gronig H (1993) A six component balance for short duration hypersonic facilities. In: Boutier A (ed.) New trends in instrumentation for hypersonic research. Kluwer, Dordrecht, pp 295-305

Jones DJ (1969) Tables of inviscid supersonic flow about circular cones at incidence, $\gamma = 1.4$. AGARDograph 137

Mee DJ (1993) Uncertainty analysis of conditions in the test section of the T4 shock tunnel. Research Report 4/93, Dept. Mech. Eng., The University of Queensland

Mee DJ, Daniel WJ, Simmons JM (1992) Three-component aerodynamic force measurements in hypervelocity impulse facilities. Proc. 11th Australasian Fluid Mechanics Conference, Hobart, 14-18 Dec. 1992, pp 55-58

Naumann KW, Ende H, Mathieu G (1993) Millisecond aerodynamic force measurement technique for high-enthalpy test facilities. In: Boutier A (ed.) New trends in instrumentation for hypersoni [illegible] pp. 307-316

Porter LM, Mee DJ, Paull A (1993) [illegible] cones and a scramjet vehicle in hypervelocity flow [illegible]

Sanderson SR, Simmons JM (1991) [illegible] city impulse facilities. AIAA J. 29(12):2185-2191

Stalker RJ, Morgan RG (1988) Free piston shock tunnel T4 - initial operation and preliminary calibration. NASA CR-181721

REPORT DOCUMENTATION PAGE

Form Approved
OMB No. 0704-0188

1. AGENCY USE ONLY *(Leave blank)*

2. REPORT DATE
January 1995

3. REPORT TYPE AND DATES COVERED
Contractor Report, CY 1993

4. TITLE AND SUBTITLE
Shock Tunnel Studies of Scramjet Phenomena 1993
Supplement 10

5. FUNDING NUMBERS
G NAGW-674
WU 505-70-62-04

6. AUTHOR(S)
R.J. Stalker, R. J. Bakos, R. G. Morgan, L. Porter, D. Mee, A. Paull, S. Tuttle, J. M. Simmons, M. Wendt, K. Skinner, Y. He, A. Neely, and W. Daniel

7. PERFORMING ORGANIZATION NAME(S) AND ADDRESS(ES)
University of Queensland
Department of Mechanical Engineering
St. Lucia, Queensland
AUSTRALIA

8. PERFORMING ORGANIZATION REPORT NUMBER

9. SPONSORING / MONITORING AGENCY NAME(S) AND ADDRESS(ES)
National Aeronautics and Space Administration
Langley Research Center
Hampton, VA 23681-0001

10. SPONSORING / MONITORING AGENCY REPORT NUMBER
NASA CR-195038

11. SUPPLEMENTARY NOTES
Langley Technical Monitor: R. Clayton Rogers
Interim Report 0 Supplement 10, NAGW-674

12a. DISTRIBUTION / AVAILABILITY STATEMENT

Unclassified - Unlimited

Subject Category 34

12b. DISTRIBUTION CODE

13. ABSTRACT *(Maximum 200 words)*

Reports by the staff of the University of Queensland on various research studies related to the advancement of scramjet technology and hypervelocity pulse test facilities are presented. These reports document the tests conducted in the reflected shock tunnel T4 and supporting research facilities that have been used to study the injection, mixing, and combustion of hydrogen fuel in generic scramjets at flow conditions typical of hypersonic flight. In addition, topics include the development of instrumentation and measurement technology, such as combustor wall shear and stream composition in pulse facilities, and numerical studies and analyses of the scramjet combustor process and the test facility operation. This research activity is Supplement 10 under NASA Grant NAGW-674.

14. SUBJECT TERMS
Scramjets, pulse facilities, hypersonic, hypervelocity, shock waves, combustion, shock tubes

15. NUMBER OF PAGES
113

16. PRICE CODE
A06

17. SECURITY CLASSIFICATION OF REPORT	**18. SECURITY CLASSIFICATION OF THIS PAGE**	**19. SECURITY CLASSIFICATION OF ABSTRACT**	**20. LIMITATION OF ABSTRACT**
Unclassified	Unclassified	Unclassified	